RADAR DETECTION AND IDENTIFICATION OF HUMAN SIGNATURES USING MOVING PLATFORMS

A Thesis
Presented to
The Academic Faculty

by

Sevgi Zübeyde Gürbüz

In Partial Fulfillment
of the Requirements for the Degree
Doctor of Philosophy
in the
School of Electrical and Computer Engineering

Georgia Institute of Technology
December 2009

RADAR DETECTION AND IDENTIFICATION OF HUMAN SIGNATURES USING MOVING PLATFORMS

Approved by:

Dr. Douglas B. Williams, Advisor
Professor, School of ECE
Georgia Institute of Technology

Dr. William L. Melvin, Advisor
Georgia Tech Research Institute
Georgia Institute of Technology

Dr. James H. McClellan
Professor, School of ECE
Georgia Institute of Technology

Dr. Aaron D. Lanterman
Associate Professor, School of ECE
Georgia Institute of Technology

Dr. Ayanna M. Howard
Associate Professor, School of ECE
Georgia Institute of Technology

Dr. Brani Vidakovic
Professor, Biomedical Engineering
Georgia Institute of Technology

Date Approved: August 12, 2009

To my most beloved teacher,
soul mate, and guardian angel:
my mother

ACKNOWLEDGEMENTS

This thesis is significant not only because it represents a major milestone and achievement in my life, but because it embodies the aspirations and dreams of my mother, who unexpectedly and suddenly passed away from an aggressive brain cancer that doctors failed to diagnose, on February 10, 2007, before she could witness my graduation. My mother was a bright and capable woman, who overcame all odds to study Mechanical Engineering at a time when there were almost no women in engineering. The youngest of six sisters, her family's value of education and sacrifices made to send her to school no doubt played an important role in her success. But it was her undying lust for knowledge, stamina, hard work, and attention to detail that enabled her to graduate ranked first in the 1968 graduating class of Istanbul Technical University's Mechanical Engineering Department. Awarded a NATO Science Scholarship, she pursued her graduate studies at MIT, Stanford and U.C. Berkeley.

But, as happens in life, while still a Master's student, she met my father, got married, and several years later, before she could complete her PhD, gave birth to me. The rest is a story I am sure many women in engineering can relate to – she juggled a job at Lawrence Livermore Labs, her graduate studies, and taking care of me and my father before finally realizing she was not superwoman. She made the ultimate choice of sacrificing what she truly loved – science and engineering – to take care of me, what she loved even more. Over a decade later, while in her 40's, my mom went back to MIT to again pursue her PhD from where she had left off, only to be thwarted again by a divorce and struggles of being a single mom, now laden not with a baby, but with a rambunctious child in need of much attention and discipline (worse than a baby!). Again, she chose me over her studies, dedicating the remainder of her life to teaching me mathematics, science, and engineering. Indeed, just before she passed away, she had

but one question for me: “Are you happy?” It was all that mattered to her in the end, because that was what she had sacrificed her whole life for.

Thus, in every real or spiritual sense, this doctorate is as much hers as it is mine. She taught me how to be a good person, a good engineer, and through her example is still teaching me how to be a good mother. I will forever be grateful and blessed for this.

There are also a number of people I wish to thank for their help and support during my graduate studies at Georgia Tech. First, I would like to thank my advisors, Dr. William L. Melvin and Professor Doug Williams. I experienced perhaps three of the biggest events one can have in life – marriage, child-birth, and loss – during the course of my PhD studies. Their understanding and support through these events was as critical as their guidance and education on technical matters for the successful completion of this thesis. I am also indebted to Dr. Ryan Hersey and Dr. Greg Showman for answering many of my questions about radar signal processing and always making the time for me, regardless of the bundles of work they had on their plates. I would also like to thank Ms. Melanie Scoville for coordinating the many meetings and conferences I attended, and having the answer to any administrative problem you can think of. I am grateful to Professor David Hertling and Ms. Marilou Mycko of ECE Graduate Affairs Office for their advice and assistance throughout my graduate studies, especially while I was still on active duty with the US Air Force, trying to knock off coursework requirements and pass the preliminary exam.

Thanks also to the faculty at the Center for Signal and Image Processing (CSIP) of Georgia Tech, and especially Professor Jim McClellan, Professor Aaron Lanterman, and Professor Mark Richards, for their contributions to my education in detection, estimation, and radar signal processing, and motivating my decision to study at Georgia Tech. On a personal level, I would like to thank the students and friends at CSIP for making life at the lab enjoyable.

I would like to thank my best friends Sibel, Ayten, Özlem, and Selma for being there for me through thick and thin. I would also like to thank my “house pals” Özlem and Gülten for being the absolutely coolest gals in Atlanta. You may have come as mere guests, but you conquered my heart and left as sisters. I would also like to thank in general our close family friends for making life in Atlanta good, even when my code wasn’t working.

During the course of my graduate studies, I was also blessed with the aid of many friends who supported me by looking after my son during the day while I was at school: Semra, Fatma, Havva, Nuray, and Dilek.

A special thanks goes out to all the members of my family for their love and support over the years. Thanks to my aunts for always being there for us. Also thanks for my mother-in-law and father-in-law for taking care of my son during the critical times before my graduation. It is a blessing to know that no matter what you are there to support us. I also would like to thank my sister-in-law for being more “sister” than “in-law” – as an only child myself, I appreciate her warmness.

I would like to thank my husband for 1) being my husband; and 2) being a great husband (mashallah). I could write a book listing the one million and one ways he’s been a blessing, but let it just suffice to say that it is a special man who thinks that wiping off poop from his baby’s behind is an “honor.” ☺ Finally, I am grateful for my son, whose unconditional love has brought out the sunshine during even my darkest days.

TABLE OF CONTENTS

LIST OF TABLES

Page

LIST OF FIGURES

SUMMARY

Radar offers unique advantages over other sensors for the detection of humans, such as remote operation during virtually all weather and lighting conditions. However, humans are difficult targets to detect because they have a small radar cross section (RCS) and move with a low velocity. Thus, humans often fall below the minimum detectable velocity (MDV) of Ground Moving Target Indication (GMTI) radars and are easily masked by ground clutter. Most current radar-based human detection systems employ some type of linear-phase matched filtering as part of the detector, such as Doppler processing or the Adaptive Matched Filter (AMF) test. Multi-channel systems also employ space-time adaptive processing (STAP) to suppress clutter and maximize output signal-to-interference-plus-noise ratio (SINR). However, the phase history of human targets is highly nonlinear, and the resulting phase mismatch causes significant SINR losses in the detector itself, degrading the human detection performance.

In fact, the nonlinearity of the human phase history is not arbitrary, but caused by the complexity of human motion. The periodic motion of each body part, especially that of the arms and legs, makes the human target return distinct and unique, distinguishable from that of even other animals, such as dogs. Thus, while many characteristics, such as the speed, trajectory, and size of a potential human target, are unknown, the uniqueness of human gait can be used to specify the structure of the expected target return. This knowledge can then be used to derive a matched filter more closely matched to the sought target's return.

In this thesis, two algorithms exploiting human modeling and gait analysis are proposed: a parameter estimation-based optimized non-linear phase (ONLP) detector, and a dictionary search-based enhanced optimized non-linear phase (EnONLP) detector.

First, the design of the ONLP detector for single-channel radar systems is considered. As the strongest component of the human return comes from the torso reflection, a sinusoidal model is employed to approximate the expected human return. Maximum likelihood estimates (MLEs) of unknown geometry and model parameters are obtained to maximize the likelihood ratio and resulting matched filter output. Comparisons of the Cramer-Rao bounds (CRB) with the variance of the parameter estimates show that at about 5 dB the MLEs meet the CRB, and that there is about 5 dB of modeling error due from the ONLP approximation. Performance of linear phase FFT-based matched filters is compared to that of the proposed ONLP detector, as well as to the ideal "clairvoyant" detector using Receiver Operating Characteristic (ROC) curves. Results show that the proposed ONLP detector consistently outperforms conventional linear-phase filters. Improved output SNR is achieved, thereby significantly increasing the probability of detection attained.

The impact of clutter is addressed by extending the parameter-estimation based ONLP detector to multi-channel systems, which enable the application of clutter mitigation techniques, and ONLP performance *in clutter* is considered. Although relative to the Gaussian noise only case performance was degraded, the ONLP algorithm continued to outperform linear-phase matched filters in highly cluttered environments as well.

Second, a dictionary-search based enhanced ONLP (EnONLP) detector is proposed that searches over a dictionary, or database, of potential human responses generated for each possible combination of parameters values in the human model. Now, the complete human model is exploited, not just the torso response. An orthogonal matching pursuit (OMP) algorithm is used to search the dictionary for the optimal linear combination of dictionary entries that represent the clutter cancelled data. The EnONLP detector thus offers a framework not only for extracting additional

information on the features of a single detected human target, but can also be used to detect and extract features of multiple targets. ROC curves comparing the performance of conventional STAP, ONLP, and EnONLP *in clutter* show that the best performance is achieved by the EnONLP algorithm, while both proposed algorithms outperform STAP.

CHAPTER 1

INTRODUCTION

Human detection and identification has many key military and security applications. Depending on the context, however, detection may involve a variety of sensors and identification may take on slightly different meanings. For example, airport surveillance aiming to locate a particular suspect would most likely employ video cameras. Here, "identification" literally implies putting names to the faces on the video tape and matching them to the face of the suspect. On the other hand, an airborne platform being used to track the movement of guerilla forces in the mountains would use radar to sense human motion, and "identification" would involve discriminating among types of targets, such as human versus vehicle. In this thesis, the term "human detection" refers to the detection of a target of a human nature, while "identification" encompasses any additional information about the target signal, including classification as human, and gender and gait analysis, which can be used to further specify the target.

Visual [1] [2] [3], acoustic [4] [5], vibration/seismic [6] [7] [8], infrared [9] [10], and electromagnetic sensors [11] [12] [13] have all been used in human detection systems. Indeed, many systems apply system fusion techniques to take advantage of the strengths of several sensors in a complementary fashion. For example, Linzmeier [10] used radar to detect potential targets in conjunction with infrared sensors for determining which targets are human. Milch [14] employed video as well as radar. The radar was used to detect probable targets and generate a preliminary hypothesis – based on RCS and speed – as to which are most likely human. Then, visual data from video was used to verify the hypothesis. Indeed, many sensor fusion systems employing radar use other sensors to determine whether a target is human or not, since radar is perceived as being inadequate to make such a determination.

While the augmentation of radar with other sensors may be useful in certain applications, this prevents the utilization of the main benefits for using radar: namely, the ability to operate far away from potential targets, to see through walls and other obstacles, such as foliage, and to perform imaging and detection during nighttime. Visual, acoustic, infrared, and seismic sensors all require being placed in proximity to the target. Also, augmentation with video means that the system can only fully function during daytime, without any obstacles impeding the line-of-sight. However, for many military and security applications, a close, direct view of the target may not be possible because of operational conditions and high risk to personnel safety. Furthermore, nighttime operation is generally a requirement. For these reasons, this thesis focuses on radar as the sole available sensor.

The problem of human detection with radar may be broken down into two key tasks: first, detecting the presence of a target, and, second, deciding whether or not the target detected is human. Most of the research in this area has focused on the latter task, while the former has been addressed more generally as slow-moving target detection.

Radar-based human detection systems have almost always used some kind of spectral processing to discriminate human targets from other reflectors. For example, Yarovoy [11] used ultra-wide band (UWB) radar to locate humans trapped in buildings by sensing respiratory motions. The radar returns from breathing and non-breathing targets were separated by analyzing the spectral variations of the radar return. The spectral response of breathing targets, such as humans, have peaks and contain frequencies corresponding to the frequency of respiration and its harmonics, whereas those of non-breathing targets are roughly flat.

Falconer [12] employed a similar technique, this time detecting, locating, and identifying building occupants with a pulsed-Doppler microwave radar placed outside the

building. The power spectral density (PSD) of a variety of objects was measured, and differences in the shaping of the PSD were used to try to differentiate between targets and guess at the activity level (resting versus moving) of human targets. For example, a low power waveform whose kurtosis greatly exceeded 3.0 was classified as an inactive person. However, only large movements were discernable.

Sabatini [15] applied wavelet analysis to the time-varying range profile measured by sonar to find human targets. Using the observation that the range profile of "confounding" targets, such as swaying plants or hand-shaken curtains, contain much higher frequency oscillations than those of a walking or dancing person, a Haar-based wavelet transform was used to remove high-frequency components and reconstruct the signal. The error between the reconstructed signal and the original signal was computed and a threshold applied to discriminate between targets: human targets would have a low error, whereas the confounding targets would have a higher error. However, this technique could be easily fooled by any other slow-moving target of predominantly low-frequency content.

Indeed, only over the last decade or so have radar-based techniques exploiting the very nature of human motion begun to be explored, perhaps influenced by research on *gait analysis* – the extraction of features from the motion of a human. In fact, the periodic, bipedal nature of human walking is so unique that one day human gait may become a biometric parameter that could be used for identification, just like fingerprints or hand geometry [16] [17]. Human gait offers the advantage of recognition at a distance, when other biometrics may not be perceivable, and is difficult to disguise. Although most work in this area has focused on gait analysis of video, there has been some work on the utilization of seismic sensors, and, most recently, radar.

In 1997, Weir [18][19] developed an ultrasound ranging device (sonar) that generated a velocity profile for the human target. This "gait velocitygram," as termed by

the authors, contained distinct features that were used in calculating gait parameters, such as walking speed, cadence, step length, step time, and time to steady-state walking. Visual differences in the velocitygram for a walking human and for a person limping were noticed, but no classification scheme was developed beyond simple observation.

Frequency-based concepts were refined with the concept of the "radar gait signature" – a spectral analysis of the gait signature that has been shown to be characteristic of humans [13][16][19-25]. Although Geisheimer [20] initially used chirplet transforms to characterize gait signature, spectrograms have been proposed as a simpler way of extracting biomechanical information from the radar return. In 2002, Geisheimer [19] experimentally verified that the overall spectrogram from a human target matched the sum of spectrograms constructed from the returns of individual body parts. The theoretical basis for this result was developed by Van Dorp [13], who divided the human body into 12 parts and computed the time-varying range for each part using a walking model developed by Thalmann [26]. Van Dorp showed that human model-based simulated gait signatures matched the spectrograms derived from measured data – an important result that will serve as the basis for the human model utilized in this thesis.

This foundation has led to much work that exploits the unique features of the human spectrogram. For example, Greneker [27] exploited the changes in stride and velocity caused by the weight of a load around the waist to propose a spectrogram-based suicide bomber detection system. Otero [22] used the spectrogram to compute features such as the stride and appendage/torso ratio. Plotting the velocity and appendage/torso ratio for pedestrians passing by, Otero observed that male and female targets were roughly grouped in different regions on the grid, suggesting that such features may be used for gender discrimination. A similar concept was pursued by Van

Dorp as well, who developed a strategy for estimating the key parameters of the Thalmann model from more detailed analysis of a human spectrogram [28]. Recent work by Bilik [29] utilizes the Thalmann model for target classification.

Spectrogram and gait analysis techniques, however, all aim at characterizing targets already detected through Doppler or Fourier-based processing; they do not address the first task of detecting the presence of a target. In this regard, human target detection presents unique challenges as humans are slow-moving targets with low radar cross section (RCS) in comparison to vehicles or other objects, making human returns fall below the minimum detectable velocity (MDV) of conventional ground moving target indication (GMTI) radars, easily obscured by ground clutter, and poorly integrated over noise. Increased temporal aperture is required to boost SNR, and therein lies a key challenge: as the aperture increases, the increasingly nonlinear target phase history leads to significant integration loss when using a Fourier (Vandermonde) basis. Thus, although lowering the MDV of SAR GMTI radars is an active area of research [30-34] and detection in clutter is a critical radar attribute, we first concern ourselves in this work with improving noise-limited human target detection performance as a pre-requisite to the more challenging case of clutter-limited detection.

Most algorithms do not take into consideration information we know a priori that is specific to human targets: namely, the uniqueness of human gait. Although gross human motion may be viewed as that of a point target with time-varying position and velocity, in fact, the complex motion of our body, especially that of the arms and legs, generate side-bands about the center frequency of the target's body Doppler frequency [24], known as micro-Doppler. The phase history for human targets reflects these frequency variations and, thus, is non-linear [35][36].

The Fourier transform, used in the Doppler processing of many conventional SAR imaging systems, can also be viewed as essentially a filter matched to linear-phase

inputs. Thus, Doppler processing of a signal of non-linear phase, such as that of human targets, results in a significant loss in output signal-to-interference-plus-noise (SINR) ratio caused by the inherent phase mismatch. This SINR loss in turn degrades the detection probability of human targets.

The main goal and key contribution of this thesis is the application of physical, kinematic models of human motion to enhance human detection and identification capabilities in even high clutter environments. Thalmann's kinematic model for human walking is used as a basis for deriving a parameterized, analytic expression of the true human target phase and for generating the synthetic human radar data used in our computer simulations. Two algorithms exploiting human modeling and gait analysis are proposed: a parameter estimation-based optimized non-linear phase (ONLP) detector, and a dictionary search-based enhanced optimized non-linear phase (EnONLP) detector. Both of these detectors are essentially "tuned" to human motion, such that the mismatch between the modeled target return and true target phase is minimized, thus maximizing the output SINR and probability of detection.

Since the strongest component of the human target return is the reflection from the torso, the ONLP algorithm approximates the torso return with a sinusoid. The unknown geometry and model parameters are then estimated using maximum likelihood estimation. Cramer-Rao bounds of parameter estimates are used to illustrate the impact of modeling error on performance. Detection performance of FFT-based matched filters is compared to that of the proposed ONLP detector, as well as to the ideal "clairvoyant" detector, representing the best performance attainable with complete knowledge of target parameters.

The ONLP detector is extended to multichannel systems so that space-time adaptive processing techniques may be applied to cancel or mitigate the effects of

clutter and further enhance detection performance. Results showing the performance of the ONLP detector in clutter are presented.

Next, an Enhanced ONLP (EnONLP) detector is proposed that employs a dictionary to store possible target returns generating from the human model for each combination of parameter values. Rather than matched filtering based on just the torso response, as in ONLP, the EnONLP detector compares the data snapshot to a parametric model of the expected target response that incorporates reflections from all body parts. An orthogonal matching pursuit algorithm is used to search the dictionary of expected target returns for the linear combination of target responses that best match the measured data. Thus, unlike ONLP, the EnONLP algorithm also has the capability of detecting the presence of multiple human targets. Performance of the EnONLP algorithm is compared to that of the parameter estimation based ONLP and conventional, fully-adaptive STAP. Finally, application of the EnONLP framework to target characterization is illustrated.

CHAPTER 2

BACKGROUND

Radar, short for “radio detection and ranging,” is an electromagnetic system used to detect and locate objects of interest (targets). Radar operates by transmitting a waveform and analyzing the echo signal returned from the reflection off the target. The echo signal differs from the transmitted waveform in basically three ways: amplitude, frequency, and time delay. Attenuation of the signal is caused by space loss (the normal loss of power of the signal over range), the reflection of only part of the transmitted energy back to the receiver, and atmospheric effects. A frequency shift occurs due to the Doppler effect caused by the relative velocity between transmitter and target. Finally, the echo is delayed because of the time it takes for the signal to travel to the target and back. Radar uses the frequency shift and time delay of the echo signal to estimate the radial velocity and distance of the target, respectively.

Continuous-wave (CW) radar, the simplest type of radar, operates by transmitting a sine wave. An example of CW radar is the hand-held device used by police to measure the speed of passing cars. Nearly all airborne platforms use “pulsed Doppler” radar, which transmits a chirp waveform for the *pulse duration* τ followed by no transmission until the end of the *pulse repetition interval* (PRI), as shown in Fig. 2.1.

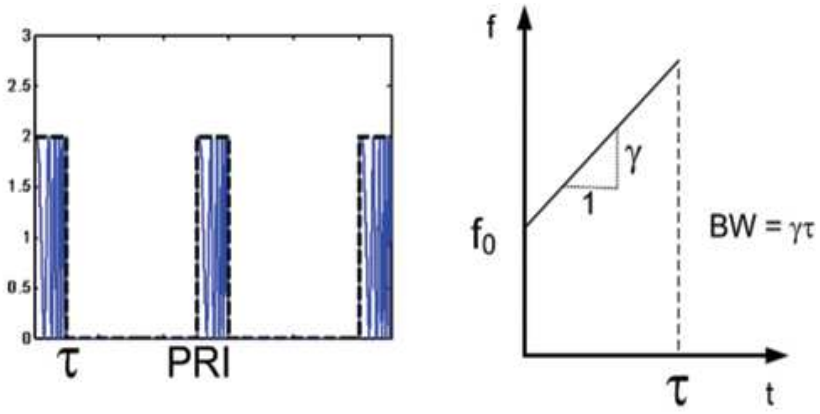

Figure 2.1: Chirp signal frequency variation with time.

2.1 Principles of Synthetic Aperture Radar

As an airplane flies along, the location of the signal transmitted by the radar slightly changes in location by the amount *vt*, where *v* is the speed of the aircraft and *t* is the time interval. The sequence of transmission locations is said to form a synthetic aperture, since the transmission or aperture points are not fixed like the transmitters of a conventional phased array antenna. Synthetic aperture radar (SAR) is advantageous relative to conventional radar because of a much higher cross-range resolution, making SAR more suitable for imaging.

For conventional radar and SAR, the cross range resolution is given by [37]

$$\Delta CR_{conv} = \frac{R\lambda}{D_{az}} \tag{2.1}$$

$$\Delta CR_{sar} = \frac{R\lambda}{2D_{az}}, \tag{2.2}$$

where R is the distance to the target, λ is the wavelength of the transmitted signal, and D_{az} is the width of the antenna in the azimuth direction. For a synthetic aperture, D_{az} is not just the size of the physical antenna, but the distance traveled by the aircraft during data collection, vT_a, where T_a is the aperture time, or duration of data collection. However, T_a cannot be made arbitrarily large but is limited by the physical antenna beamwidth (Fig. 2.2). A scatterer only contributes to the SAR data while being illuminated by the radar. Thus, the maximum SAR aperture size is given by

$$D_{SAR,\max} = R\theta_{az} = Rk\frac{\lambda}{D_{az}}, \tag{2.3}$$

where θ_{az} is the beamwidth and k is a scale factor that depends on the antenna design.

The minimum cross-range resolution for SAR can thus be found as

$$\Delta CR_{\min} = \frac{D_{az}}{2}. \tag{2.4}$$

The significance of this result is that the lower bound on stripmap SAR resolution is *independent of range*, which is especially desirable for imaging applications.

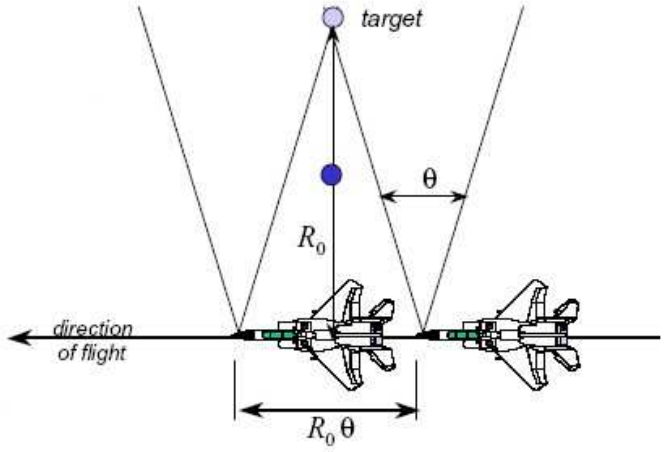

Figure 2.2: Illustration of maximum synthetic aperture length [37].

2.1.1 Space-Time Target Signature

Because of the motion of the aircraft, the distance between the target and transmitter varies with time. This range variation generates a hyperbolic curve (Fig. 2.3) that is characteristic of all SAR systems.

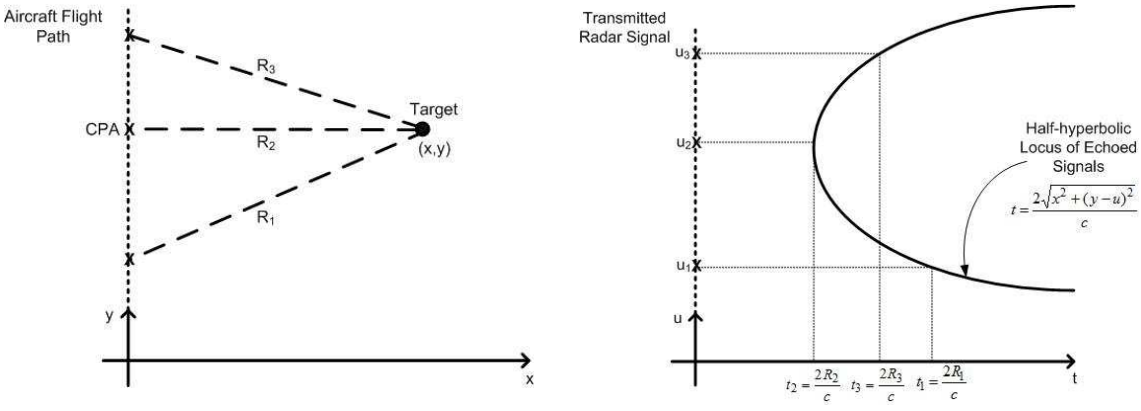

(a) (b)

Figure 2.3: Graphical representation of range variation. (a) Aperture-target geometry. (b) Formation of hyperbolic SAR signature [38].

Mathematically, this hyperbolic signature can be calculated by considering the time delay at each aperture point, $t_n = \frac{2R_n}{c}$, where R_n is the distance between the target and the n^{th} aperture location and c is the speed of light. Substituting for the range variation,

$$t_n = \frac{2}{c}\sqrt{x^2 + (y - u_n)^2} \tag{2.5}$$

$$\frac{c^2}{4}t_n^2 - (u_n - y)^2 = x^2 \tag{2.6}$$

yields the equation for a hyperbola for a target located at (x,y), where u_n is the aircraft position.

Depending on the geometry of the flight path relative to the target location, differing portions of the hyperbola may be seen in the space-time map of the system, thereby causing *range migration*. Range migration refers to the fact that the target energy is not confined to just one range bin, but is in fact spread across range. Range migration can be divided into two components: a linear component, known as *range walk*, and a quadratic component, known as *range curvature* (Fig. 2.4). Range walk is graphically represented by a line between the starting and ending points of the synthetic aperture and represents the range difference between the initial and final ranges.

Range curvature is a measure of the deviation of the hyperbolic signature from the line connecting the endpoints:

$$\Delta R_{\max} = \frac{(vNT)^2}{8R_{\min}} \tag{2.7}$$

where v is the velocity of the aircraft, N is the total number of pulses transmitted, T is the PRI, and R_{min} is the minimum distance between aperture and target during the course of data collection. As will be seen later in Section 2.2 on SAR signal processing, these effects can be "corrected" during signal processing so that the final output in the range-Doppler map peaks at a single point, and the energy returned from the scatterer is maximally collected.

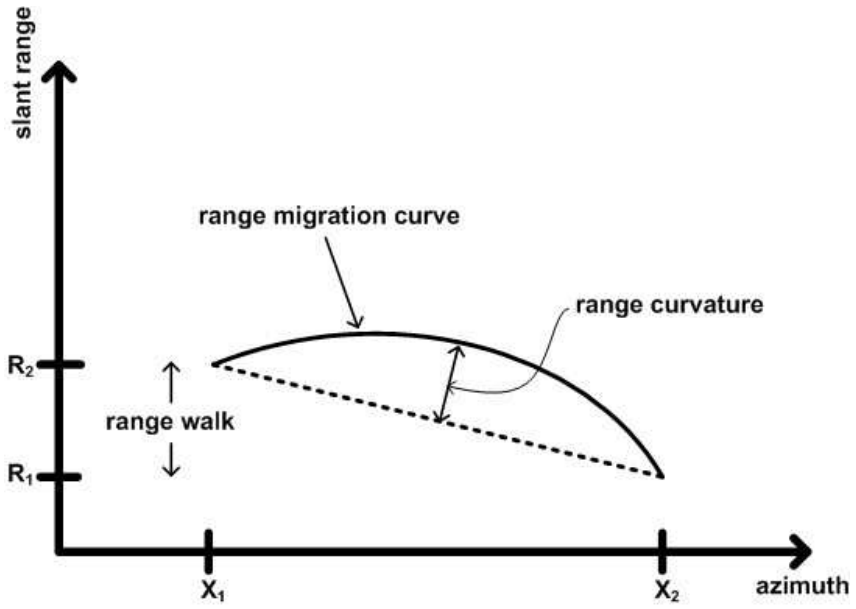

Figure 2.4: Range migration due to hyperbolic target signature [39].

2.1.2 Slow-Time Phase History

The echo signal, delayed in time and shifted in frequency relative to the transmitted signal, can be expressed mathematically as

$$s_r(n,t) = A_o rect\left(\frac{\hat{t} - t_d}{\tau}\right) e^{j\left[2\pi f_c (t - t_d) + \pi\gamma(\hat{t} - t_d)^2\right]}, \tag{2.8}$$

where the *rect()* function is defined as $rect(u) = 1$ for $|u| \le \frac{1}{2}$ and $rect(u) = 0$ for $|u| \ge \frac{1}{2}$; the overall time interval, t, is defined in terms of the pulse number, n, and time referenced from the beginning of each PRI, $\hat{t}$, as $t = \hat{t} + (n-1)PRI$; t_d is the time delay between transmission and receipt of the signal, and f_c is the transmitted chirp signal's initial frequency, τ is the pulse duration, γ is the chirp rate, and A_o is an attenuation scale factor given by the range equation:

$$A_o = \frac{G\lambda\sqrt{P_t\sigma_T\sigma_n}}{(4\pi)^{1.5}R_i^2\sqrt{L_s}\sqrt{L_a}\sqrt{T_{sys}}}. \tag{2.9}$$

Here, R_i is the target range, G is the antenna gain, L_a is the atmospheric loss, P_t is the transmitted signal power, λ is the wavelength, L_s is the system loss, T_{sys} is the system temperature, σ_n is the noise standard deviation, and σ_T is the target's radar cross-section (RCS).

Substituting Eq. (2.5) for t_d, the signal phase may be written as

$$\begin{aligned}\theta &= \angle A_o + \pi\gamma t_d^2 + \pi\gamma\hat{t}^2 - 2\pi\left(f_c + \gamma\hat{t}\right)t_d \\ &= \frac{2\pi\gamma}{c^2}\left(x^2 + (y-u_n)^2\right) - \frac{4\pi}{c}\left(f_c + \gamma\hat{t}\right)\sqrt{x^2 + (y-u_n)^2}.\end{aligned} \tag{2.10}$$

Notice that this expression is not quadratic; however, using the approximation $\sqrt{1+x^2} \approx 1 + x/2$ for x << 1, the phase can be shown to be approximately quadratic in n, the slow-time index. Substituting the position of the aircraft $u_n = vnT$, we obtain

$$\sqrt{x^2 + (y-vnT)^2} = x\sqrt{1 + \left(\frac{y-vnT}{x}\right)^2} \approx x\left[1 + \frac{(y-vnT)^2}{2x^2}\right] \tag{2.11}$$

for $\left(\frac{y-vnT}{x}\right)^2 << 1$. This approximation is valid for most airborne data collection geometries. Thus,

$$\theta \approx \angle A_o + \frac{2\pi}{c}\left(\frac{2\gamma}{c} - \frac{f_c + \gamma\hat{t}}{x}\right)(y-vnT)^2 + \frac{4\pi\gamma}{c^2}x^2 + \pi\gamma\hat{t}^2 - \frac{4\pi}{c}\left(f_c + \gamma\hat{t}\right)x. \tag{2.12}$$

The effect of this quadratic phase is to smear the target response in the Doppler dimension. In contrast, the Fourier transform of a signal with linear phase is an impulse located at a frequency equal to the linear scaling of the time-domain signal. Thus, prior to Doppler processing, most processing techniques remove any non-linear phase terms from the slow-time phase history, and thereby better match to the target response to maximize SNR.

2.1.3 Doppler Shift

The expected Doppler shift can be derived from computing the phase of two successive pulses:

$$\theta_1 = 2\pi f_c\left(t - t_{d1}\right) + \pi\gamma\left(\hat{t} - t_{d1}\right)^2 \tag{2.13}$$

$$\theta_2 = 2\pi f_c\left(t - t_{d2}\right) + \pi\gamma\left(\hat{t} - t_{d2}\right)^2 \tag{2.14}$$

Thus,
$$\Delta\theta = 2\pi\left(f_c + \gamma\hat{t}\right)\left(t_{d1} - t_{d2}\right) + \pi\gamma\left(t_{d2}^2 - t_{d1}^2\right) \tag{2.15}$$

Each pulse is transmitted with an interval equal to the PRI, *T*, during which the target travels a distance of R_2-R_1=vT. Ignoring the second-order terms of time, we find

$$\Delta\theta \approx 2\pi\left(f_c + \gamma\hat{t}\right)\left(-\frac{2vT}{c}\right). \tag{2.16}$$

Doppler shift is defined as the phase change per PRI: $\Delta f = \Delta\theta / T$. For $\gamma\hat{t} << f_c$, we find in radians

$$\Delta f = -\frac{4\pi v f_c}{c}. \tag{2.17}$$

2.2 SAR Signal Processing Techniques

Signal processing of SAR data can be divided into five different stages: 1) range processing, 2) range walk correction, 3) Doppler drift correction, 4) quadratic phase error correction, and 5) Doppler processing. After initially presenting these stages in detail for single-channel SAR systems, the techniques will be extended to the multi-channel SAR case, the ultimate goal being to approximate the backprojection solution.

2.2.1 Range Processing

The optimal range processing method is matched filtering, also known as pulse compression, since the matched filter output of a chirp signal approximately resembles a sinc function for high time-bandwidth products ($\gamma\tau$ > 100). However, the implementation

of pulse compression can be impractical in some radar systems because of their high bandwidth. High-quality A/D converters at such rates are difficult to obtain; thus, most systems instead use a technique known as *stretch processing*, also known as *dechirp* or *deramp* processing. In particular, stretch processing is effective for applications in which very high range resolution is required, but only over a relatively small range window.

A typical stretch processor will begin by modulating the signal down to baseband and multiplying it with a replica of the transmitted chirp, referenced to the center of the range window. Mathematically,

$$s_{out}(n,t) = s_r(n,t)e^{-j2\pi f_c t}e^{-j\pi\gamma(\hat{t}-t_o)^2}, \tag{2.18}$$

where $s_r(n,t)$ is the received radar signal and t_o is the round-trip delay between the aperture and the middle of the range window. Grouping constant terms into a single scaling factor, ξ, the output can be simplified to the form

$$s_{out}(n,t) = \xi e^{-j2\pi\gamma\Delta t(\hat{t}-t_o)}e^{j\pi\gamma(\Delta t)^2}, \tag{2.19}$$

where $\Delta t = t_d - t_o$. The phase term that is quadratic in Δt is a complex constant that is called the *residual video phase*. The remaining term is a constant-frequency complex exponential proportional to the range of the target relative to the reference range. As illustrated in Fig. 2.5, taking the FFT of this signal will yield lines of constant frequency for each target return that can then be converted into range:

$$R = R_o + \frac{c}{2\gamma}F_d, \tag{2.20}$$

where F_d is the frequency found by the FFT.

Both pulse compression and stretch processing techniques give a range resolution of $\Delta R = c\tau/2$. Correct range processing is also dependent upon ensuring that there is no *range aliasing* or *eclipsing loss*. In other words, targets should be closer than $R_{\max} = cT/2$ and further than $R_{\min} = c\tau/2$.

The result of range processing a raw data matrix from data collected by the Canadian RADARSAT satellite is shown in Fig. 2.6.

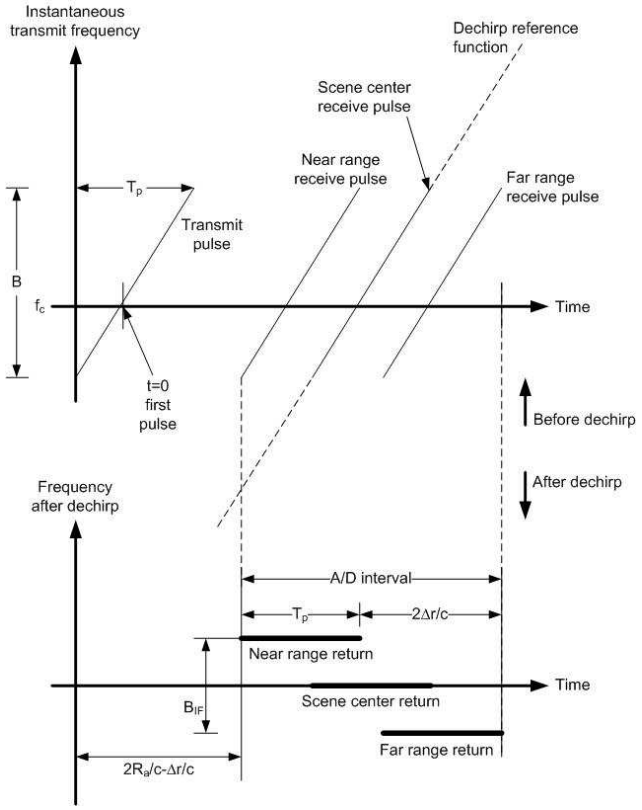

Figure 2.5: Illustration of stretch processing concept [39].

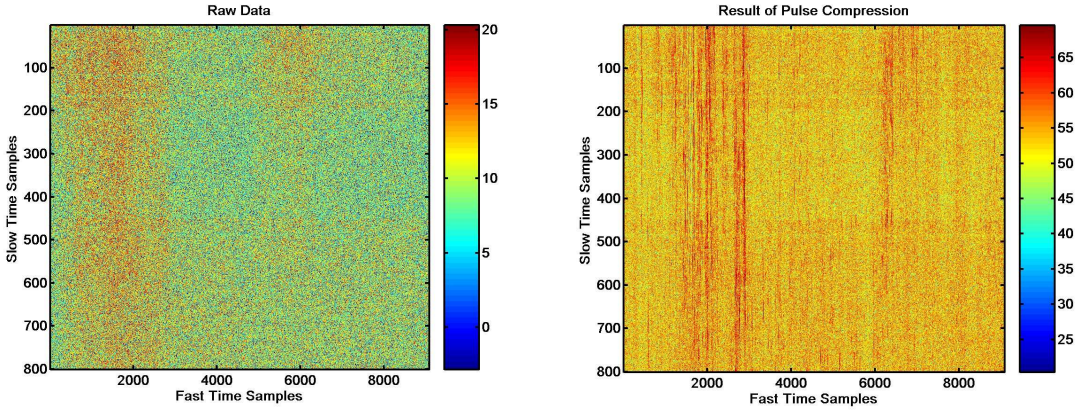

(a) (b)

Figure 2.6: Range processing results. (a) Graphical representation of unprocessed data matrix. (b) Data matrix after range processing.

2.2.2 Range Walk Correction

From a distance, the range processed data may seem to have no significant range migration errors; however, a closer look reveals that range walk is present, with negligible range curvature (Fig. 2.7a). Removal of the linear slope in the data is known as *range walk correction* and is accomplished by multiplying the data with a linear phase shift:

$$s_{rwc} = F_t^{-1}\left[F_t\left(s_{out}(n_s,t)\right)e^{j\omega k(n_s)}\right] \tag{2.21}$$

where F_t is the Fourier transform operator, k is a scaling-factor, n_s is a particular slow-time value being processed, and ω is frequency. The result of range walk correction applied to the RADARSAT data is shown in Fig. 2.7b.

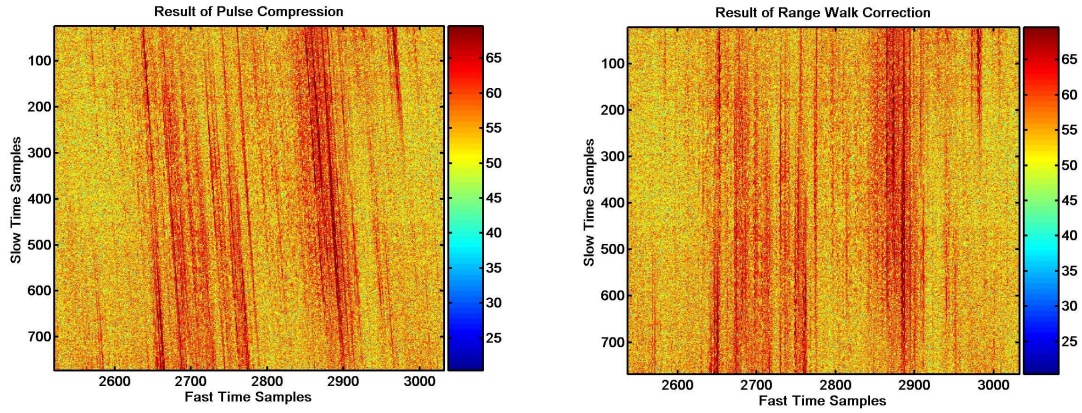

(a) (b)

Figure 2.7: Range walk correction results. (a) Close up of pulse compressed data exhibiting range walk. (b) Data matrix after range walk correction.

2.2.3 Doppler Drift Correction

Doppler drift is defined as the change in the frequency of a signal caused by the relative radial acceleration between the sender and the receiver and should not be confused with the Doppler shift that is due to relative radial velocity changes. In data collected by satellites such as the RADARSAT data, Doppler drift is caused by the

motion of the earth and causes a skewing or smearing of the target Doppler (Fig. 2.8a). Applying a linear phase shift, however, can correct the skewing:

$$s_{ddc} = F_t^{-1}\left[F_t\left(s_{out}(n_s,t)\right)e^{j\omega k(t_s)}\right] \tag{2.22}$$

where k is a scaling factor, t_s is a particular fast-time value being processed, and ω is frequency. The result of Doppler drift correction applied to the RADARSAT data is shown in Fig. 2.8b.

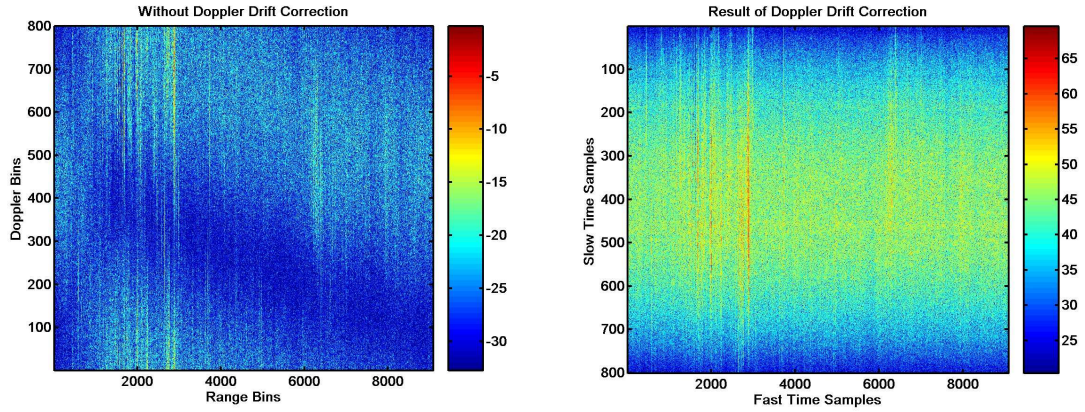

(a) (b)

Figure 2.8: Doppler drift correction results. (a) Before. (b) After.

2.2.4 Quadratic Phase Error Correction

Many techniques exist for removing the quadratic component of the phase. Perhaps the most straightforward method is to simply subtract out a quadratic factor of the form e^{jkx^2} and iterate over k to see which value minimizes the quadratic error. Other techniques include autofocus methods [39] such as the map drift (MD) algorithm, phase difference autofocus (PDA), and phase gradient autofocus (PGA).

MD directly estimates the quadratic phase coefficient and then, using this estimate, applies a correction to the signal phase history. The quadratic coefficient is estimated by first dividing the image into two half-apertures (left and right). The

quadratic coefficient in both half-apertures is identical, whereas the linear components have opposite signs. When the Fourier transform of both halves is taken, the linear components will shift the result in opposite directions. A measure of this relative shift can be obtained by cross-correlating the two half-apertures and looking at the location of the peak of this cross-correlation. Because the quadratic phase error is proportional to the shift, the peak location, in fact, can be used to estimate the quadratic coefficient, which is then easily subtracted from the phase history. Iterating this procedure yields more accurate results; typically two to six iterations are sufficient.

Unfortunately, the MD algorithm is quite computationally intensive. Thus, as an alternative, the PDA algorithm was proposed. PDA proceeds virtually the same as MD, except that rather than iterating, the correlation functions obtained from each range bin are averaged. Thus, in one step PDA can achieve the same quality of result as several iterations of MD.

PGA is a technique that can be applied not just on quadratic phase errors but also on higher-order phase errors as well. First, the range bins with the greatest target energy are selected from a range compressed image. A circular shift is applied to line up the peaks, after which the data is windowed so as to reduce noise that could corrupt the estimate. Using the derivative property of the Fourier transform, an estimate of the phase error can be obtained, and the signal phase history accordingly corrected.

2.2.5 Doppler Processing

The effects of quadratic phase error correction can be visibly seen in the image once Doppler processing – in other words, the discrete Fourier transform of each range bin across slow time – is performed (Fig. 2.9). Those familiar with Atlanta may be able to recognize the five slanted lines in the center of the image as being the runways of the Atlanta Hartsfield-Jackson Airport.

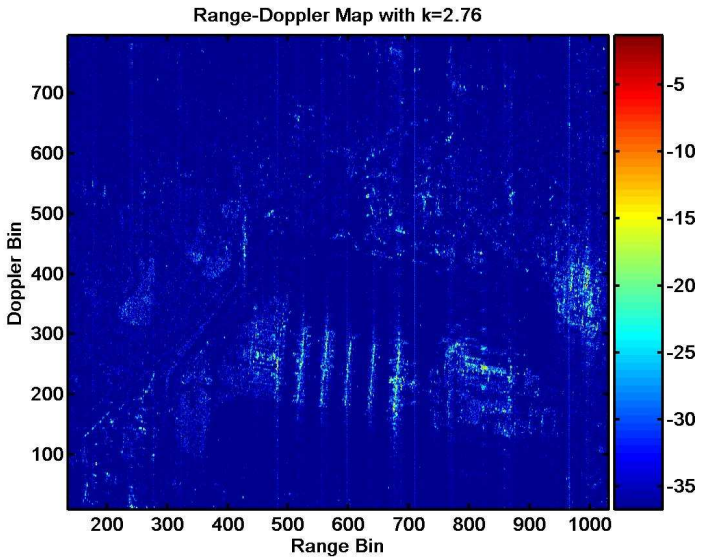

Figure 2.9: Image after all processing stages have been performed.

2.2.6 Multi-channel Processing

The discussion up to this point has focused on techniques as applied to a single-channel antenna; however, most airborne platforms employ radar comprised of multi-channel antenna arrays. Whereas before the data was comprised of a fast-time/slow-time 2-dimensional matrix; now another dimension, namely the number of antenna elements or channels, has been added. Thus, the input data of a multi-channel radar system may be organized as a data cube (Fig. 2.10) with independent axes of fast-time, slow-time, and channel number. Note that F_s is the sampling frequency, θ is the angle of arrival relative to the array normal, c is the speed of light, and d is the distance between adjacent array elements.

Consider an electromagnetic wave of the form $Ae^{j\Omega t}$ striking a uniform linear array, as illustrated in Fig. 2.11. Then, the time delay in the arrival of the waveform between adjacent array elements may be computed as

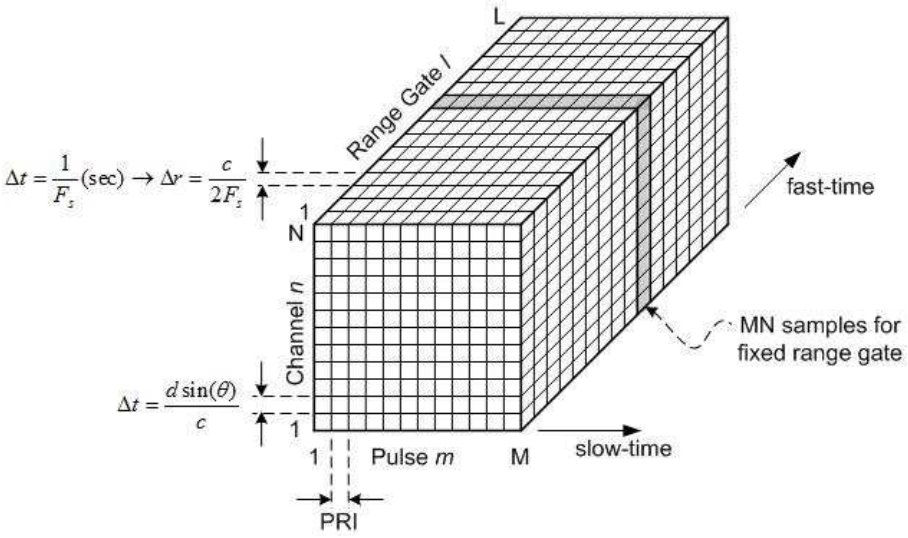

Figure 2.10: Radar data cube for a single coherent processing interval.

$$\Delta t = \frac{d\sin(\theta)}{c}, \tag{2.23}$$

and the signal observed at the n^{th} array element is

$$y_n(t) = Ae^{j[\Omega(t-nd\sin\theta/c)+\phi_0]}, \tag{2.24}$$

where ϕ_0 accounts for the phase offset at the first array element.

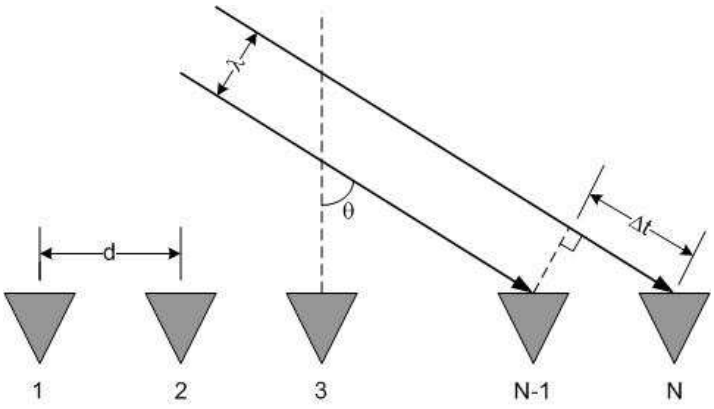

Figure 2.11: Waveform striking a uniform linear array.

The spatial snapshot of the array is defined as a vector comprised of samples of the N elements taken at the same time. Factoring out the constant terms into the modified amplitude factor, $\tilde{A}$,

$$y_n(t_s) = Ae^{j[\Omega(t_s - nd\sin\theta/c)+\phi_0]} = \tilde{A}e^{-j\Omega nd\sin\theta/c}. \quad (2.25)$$

Thus, the spatial snapshot ***y*** is

$$\mathbf{y} = \begin{bmatrix} y[0] & y[1] & \cdots & y[N-1] \end{bmatrix}^T = \tilde{A}\mathbf{a_s}(\theta), \quad (2.26)$$

where

$$\mathbf{a_s}(\theta) \equiv \begin{bmatrix} 1 & e^{-j\vartheta_s} & \cdots & e^{-j(N-1)\vartheta_s} \end{bmatrix} \quad (2.27)$$

is the spatial steering vector and $\vartheta_s \equiv \Omega nd\sin\theta/c = 2\pi d\sin\theta/\lambda$ is the spatial frequency in radians.

Similarly, the temporal steering vector is given by considering the pulse-to-pulse change in Doppler, f_D, as follows

$$\mathbf{b}_t(\varpi_t) \equiv \begin{bmatrix} 1 & e^{-j\varpi_t} & \cdots & e^{-j(M-1)\varpi_t} \end{bmatrix}, \quad (2.28)$$

where ϖ_t is the normalized Doppler frequency defined in terms of the pulse repetition frequency (PRF) as $\frac{f_D}{PRF} = f_D PRI$.

Thus, the MN x 1 space-time steering vector may be computed as

$$\mathbf{v}(\vartheta_s, \varpi_t) = \mathbf{a_s}(\vartheta_s) \otimes \mathbf{b}_t(\varpi_t). \quad (2.29)$$

The space-time steering vector ***v*** is simply a model of the response of the target at a spatial frequency υ_s and a normalized Doppler ϖ_t. The true target data is contained within the space-time snapshot of the data, a two-dimensional slice of the data cube *y(l,m,n)* taken at range bin l_0. Usually, prior to processing the snapshot is converted to an MNx1 column vector by stacking the columns as [37] [71]

$$\boldsymbol{\chi} = \begin{bmatrix} y[l_0,0,0] \\ y[l_0,0,1] \\ \vdots \\ y[l_0,0,N-1] \\ y[l_0,1,0] \\ y[l_0,1,1] \\ \vdots \\ y[l_0,1,N-1] \\ \vdots \\ y[l_0,M-1,0] \\ y[l_0,M-1,1] \\ \vdots \\ y[l_0,M-1,N-1] \end{bmatrix}. \tag{2.30}$$

Most multi-channel processors seek to apply a set of weights, ***h***, to the data snapshot, $\boldsymbol{\chi}$, such that a scalar output, *z*, is produced for use in a detector.

$$z = \mathbf{h}^H \boldsymbol{\chi}. \tag{2.31}$$

The linear filter ***h*** may be designed in a variety of ways to accomplish differing objectives. For example, steering the array to maximize the response at a given angle of arrival, or reducing the antenna side lobes. In this work, we select ***h*** such that the output is maximized while any sources of interference, such as clutter, are minimized.

2.2.7 Clutter Cancellation

The optimum space-time filter is defined as the filter that maximizes the output signal-to-interference ratio (SIR). A complex input signal ***x*** may be written in terms of signal ***s*** and interference $\boldsymbol{x}_n$ as $\boldsymbol{x} = \boldsymbol{s} + \boldsymbol{x}_n$. After filtering with ***h***, the signal and interference components are $\boldsymbol{h}^H\boldsymbol{s}$ and $\boldsymbol{h}^H\boldsymbol{x}_n$, respectively. Thus, the SIR is

$$SIR = \frac{E[\mathbf{h}^H \mathbf{s}\mathbf{s}^H \mathbf{h}]}{E[\mathbf{h}^H \mathbf{x}_\mathbf{n}\mathbf{x}_\mathbf{n}^\mathbf{H}\mathbf{h}]} = \frac{\mathbf{h}^H \mathbf{s}\mathbf{s}^H \mathbf{h}}{\mathbf{h}^H \mathbf{R}_I \mathbf{h}}, \tag{2.32}$$

where $\boldsymbol{R_I}$ is defined as the interference covariance matrix, $\mathbf{R_I} \equiv E[\mathbf{x_n x_n^H}]$.

Maximizing the SIR yields the optimum space-time filter, given by [40-46] as

$$\mathbf{h} = k\mathbf{R}_I^{-1}\mathbf{s}\,, \tag{2.33}$$

where *k* is a constant scalar.

Proof:

Following the discussion given in Richards [37], we begin by applying Schwartz's Inequality to simplify the expression for SIR. Schwartz's Inequality states that if $\boldsymbol{\alpha} = k\boldsymbol{\beta}$ for a constant scalar *k*, then

$$\left|\boldsymbol{\alpha}^H\boldsymbol{\beta}\right|^2 \le \left\|\boldsymbol{\alpha}\right\|^2\left\|\boldsymbol{\beta}\right\|^2. \tag{2.34}$$

If we define $\boldsymbol{\alpha}^H\boldsymbol{\beta} = \mathbf{h}^H\mathbf{s}$, then $\left|\boldsymbol{\alpha}^H\boldsymbol{\beta}\right|^2 = \mathbf{h}^H\mathbf{s}\mathbf{s}^H\mathbf{h}$, which is the numerator of the expression for the SIR. To form one of the factors in Schwartz's Inequality such that it matches the denominator, we must factor $\boldsymbol{R_I}$ as the product of two matrices, namely, its square root. This in turn imposes the requirement that the interference covariance matrix be positive definite. Then, we may express $\boldsymbol{R_I}$ as $\boldsymbol{R_I} = \boldsymbol{A}^H\boldsymbol{A}$. The denominator may then be written as $\mathbf{h}^H\mathbf{R_I}\mathbf{h} = \mathbf{h}^H\mathbf{A}^H\mathbf{A}\mathbf{h} = (\mathbf{A}\mathbf{h})^H\mathbf{A}\mathbf{h} = \left\|\mathbf{A}\mathbf{h}\right\|^2$. Thus, we define $\boldsymbol{\alpha} = \mathbf{A}\mathbf{h}$, from which it follows that $\boldsymbol{\beta} = (\mathbf{A}^H)^{-1}\mathbf{s}$ to be consistent with our previous definition of the numerator.

Schwartz's Inequality then gives

$$\mathbf{h}^H\mathbf{s}\mathbf{s}^H\mathbf{h} \le \left(\mathbf{h}^H\mathbf{R_I}\mathbf{h}\right)\left(\mathbf{s}^H\mathbf{R_I}^{-1}\mathbf{s}\right). \tag{2.35}$$

Rearranging to solve for SIR, we find

$$SIR \le \mathbf{s}^H\mathbf{R_I}^{-1}\mathbf{s}\,. \tag{2.36}$$

Equality occurs if and only if $\boldsymbol{\alpha} = k\boldsymbol{\beta}$ or $\mathbf{A}\mathbf{h}_{\mathbf{opt}} = k(\mathbf{A}^H)^{-1}\mathbf{s}$. Solving for the optimum weight vector, we find

$$\mathbf{h}_{\mathbf{opt}} = k\mathbf{A}^{-1}(\mathbf{A}^H)^{-1}\mathbf{s} = k(\mathbf{A}\mathbf{A}^H)^{-1}\mathbf{s} = k\mathbf{R_I}^{-1}\mathbf{s}\,, \tag{2.37}$$

Q.E.D.

Typically, an estimate of the true interference covariance matrix is computed by averaging over *P* range bins:

$$\hat{\mathbf{R}}_{\mathbf{I}} = \frac{1}{P}\sum_{p=1}^{P}\mathbf{x}_{\mathbf{p}}\mathbf{x}_{\mathbf{p}}^{-1}\,. \tag{2.38}$$

While the filter derived in (2.33) is an optimal filter, its computational complexity prevents it from being realizable for realistic numbers of array elements and pulse numbers. This limitation has led to the development of a plethora of STAP based techniques, which employ a variety of rank-reduction and subspace techniques to manage the computational workload (see [46] for more detail). For the purposes of this thesis, however, we will be directly utilizing the optimal solution.

The clutter suppression properties of (2.33) are illustrated in Fig. 12 below.

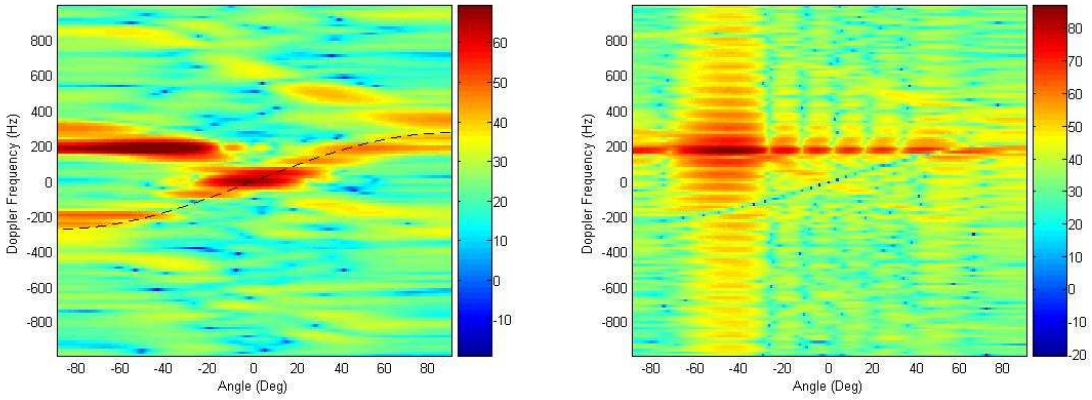

(a) (b)

Figure 2.12: Angle-Doppler maps showing a single human target in clutter. (a) Before clutter cancellation. (b) After clutter cancellation.

2.3 Signal Detection Theory

As noted in the beginning of this chapter, one of the primary functions carried out by a radar signal processor is that of *detection*, i.e. deciding whether or not a target is present. One of two hypotheses can be assumed true:

H_0: The radar measurement is the result of interference only.

H_1: The radar measurement is the combined result of interference and target echoes.

Mathematically, these hypotheses may be expressed as

$$\begin{aligned} H_0 &: \mathbf{x} = \mathbf{x_n} \\ H_1 &: \mathbf{x} = \mathbf{s} + \mathbf{x_n} \end{aligned} \tag{2.39}$$

where $\boldsymbol{x}$ represents the measured radar data, $\boldsymbol{s}$ represents the expected target response as described in (2.8), and $\boldsymbol{x_n}$ represents the interference.

If H_0 best matches the data, the detector declares that a target was not present at the range, angle and Doppler coordinates of the measurement. If H_1 best matches the data, the detector indicates that a target is present. The "best match" is determined by comparing statistical descriptions of each hypothesis. The primary approaches to simple hypothesis testing are the *classical* approach based on the Neyman-Pearson theorem and the *Bayesian* approach based on minimization of the Bayes risk [47]. Most radars employ a Neyman-Pearson approach to signal detection, a detailed discussion of which can be found in books by Richards [37], Kay [47], Johnson and Dudgeon [48], Helstrom [49], and Morris and Harkness [50].

The Neyman-Pearson criterion is designed to maximize the probability of detection (P_D) – the probability that a target is declared (i.e. H_1 is chosen) when a target is present – under the condition that the probability of false alarm (P_{FA}) – the probability that a target is declared when a target is not present – does not exceed a set constant. Typically this constant is determined from which rate of false alarms can be tolerated, which is in turn dependent upon the consequences of acting upon a false alarm. For example, while a false alarm in surveillance radar may result in the tracking of a nonexistent target, the same radar when mounted on a weapons platform may result in the firing of a missile and have critical consequences.

Mathematically, the Neyman-Pearson criterion may be stated as

$$\text{Choose } \Re_1 \text{ such that } \mathrm{P_D} \text{ is maximized for } \mathrm{P_{FA}} \le \alpha\,, \tag{2.40}$$

where $\mathcal{R}_1$ is the set of all observations of $\boldsymbol{x}$ for which H_1 will be chosen and α is the maximum allowable false alarm probability. Applying the method of Lagrange multipliers, this optimization problem is solved as follows:

$$\nabla_\lambda F = 0\,, \text{ for } F \equiv P_D + \lambda\left(P_{FA} - \alpha\right) \tag{2.41}$$

Substituting

$$P_D = \int_{\Re_1} p_{\mathbf{x}}\left(\mathbf{x} \mid H_1\right) d\mathbf{x} \tag{2.42}$$

$$P_{FA} = \int_{\Re_1} p_{\mathbf{x}}\left(\mathbf{x} \mid H_0\right) d\mathbf{x}\,, \tag{2.43}$$

where $p_x(\boldsymbol{x}|H_0)$ is the probability density function (PDF) of $\boldsymbol{x}$ given that a target was not present, and $p_x(\boldsymbol{x}|H_1)$ is the PDF of $\boldsymbol{x}$ given that a target was present, into (2.41)

$$F = -\lambda\alpha + \int_{\Re_1} \left\{ p_{\mathbf{x}}\left(\mathbf{x} \mid H_1\right) + \lambda p_{\mathbf{x}}\left(\mathbf{x} \mid H_0\right) \right\} d\mathbf{x} \tag{2.44}$$

As λ could be positive or negative, F is only maximized when the integral is maximized, i.e., when $p_{\mathbf{x}}\left(\mathbf{x} \mid H_1\right) + \lambda p_{\mathbf{x}}\left(\mathbf{x} \mid H_0\right) > 0$.

Thus, our decision rule, known as the likelihood ratio test (LRT) is

$$\frac{p_{\mathbf{x}}\left(\mathbf{x} \mid H_1\right)}{p_{\mathbf{x}}\left(\mathbf{x} \mid H_0\right)} \underset{H_0}{\overset{H_1}{\gtrless}} -\lambda \tag{2.45}$$

Application of the LRT in radar detection will be illustrated using the case of detection in Gaussian noise, discussed next.

2.3.1 Detection in Gaussian Noise

Consider the case when the interference signal, $\boldsymbol{x_n}$, is comprised only of complex Gaussian distributed noise with covariance matrix $\boldsymbol{R_x}$ and the received radar signal, $\boldsymbol{s}$, is completely known. Then the joint PDF of N complex Gaussian samples is

$$p_{\mathbf{x}}(\mathbf{x}) = \frac{1}{\det(\pi R_{\mathbf{x}})} e^{\left\{-(\mathbf{x}-\boldsymbol{\mu}_{\mathbf{x}})^H \mathbf{R}_{\mathbf{x}}^{-1}(\mathbf{x}-\boldsymbol{\mu}_{\mathbf{x}})\right\}} \tag{2.46}$$

Under hypothesis H_0, $\boldsymbol{\mu_x} = \mathbf{0}$; under hypothesis H_1, $\boldsymbol{\mu_x}$ is the N x 1 vector mean of the signal $\boldsymbol{x} = \boldsymbol{s} + \boldsymbol{x_n}$, i.e. $\boldsymbol{\mu_x} = \boldsymbol{s}$. The likelihood ratio may then be expressed as

$$\frac{e^{\left\{-(\mathbf{x}-\mathbf{s})^H \mathbf{R}_{\mathbf{x}}^{-1}(\mathbf{x}-\mathbf{s})\right\}}}{e^{\left\{-\mathbf{x}^H \mathbf{R}_{\mathbf{x}}^{-1}\mathbf{x}\right\}}} > -\lambda \equiv \eta \,. \tag{2.47}$$

Taking the logarithm of both sides,

$$-(\mathbf{x}-\mathbf{s})^H \mathbf{R}_{\mathbf{x}}^{-1}(\mathbf{x}-\mathbf{s}) + \mathbf{x}^H \mathbf{R}_{\mathbf{x}}^{-1}\mathbf{x} > \ln(\eta), \tag{2.48}$$

which simplifies to

$$T(\mathbf{x}) = \mathrm{Re}\left\{\mathbf{s}^H \mathbf{R}_{\mathbf{x}}^{-1}\mathbf{x}\right\} > \ln(\eta) - \mathbf{s}^H \mathbf{R}_{\mathbf{x}}^{-1}\mathbf{s} \equiv \eta' \,. \tag{2.49}$$

The threshold η' is found by setting the probability of false alarm to the maximum tolerable rate and then solving for the threshold from the definition $P_{FA} \equiv \Pr\{T(\mathbf{x}) > \eta' \mid H_0\}$. The PDF for the test statistic $\boldsymbol{T(x)}$ may be determined by first observing that, since the sum of Gaussian variables is Gaussian, $\boldsymbol{T(x)}$ must also be Gaussian distributed. Thus, specifying the PDF only requires computing the expectation and variance of $\boldsymbol{T(x)}$ under each hypothesis:

$$E[T(\mathbf{x}); H_0] = E\left[\mathrm{Re}\{\mathbf{s}^H \mathbf{R}_{\mathbf{x}}^{-1}\mathbf{x}_{\mathbf{n}}\}\right] = \mathrm{Re}\left\{E[\mathbf{s}^H \mathbf{R}_{\mathbf{x}}^{-1}\mathbf{x}_{\mathbf{n}}]\right\} \tag{2.50}$$

Defining $\mathbf{y} \equiv \mathbf{s}^H \mathbf{R}_{\mathbf{x}}^{-1}$,

$$E[T(\mathbf{x}); H_0] = \mathrm{Re}\left\{E\left[\sum_{n=0}^{N-1} y[n]x_n[n]\right]\right\} = \mathrm{Re}\left\{\sum_{n=0}^{N-1} y[n]E[x_n[n]]\right\} = 0 \tag{2.51}$$

Similarly,

$$E[T(\mathbf{x});H_1] = E\left[\mathrm{Re}\{\mathbf{s}^H\mathbf{R}_\mathbf{x}^{-1}(\mathbf{s}+\mathbf{x_n})\}\right] = \mathrm{Re}\left\{\mathbf{s}^H\mathbf{R}_\mathbf{x}^{-1}\mathbf{s}\right\} \tag{2.52}$$

since $E[\mathbf{s}^H\mathbf{R}_\mathbf{x}^{-1}\mathbf{x_n}] = 0$ and $\mathbf{s}^H\mathbf{R}_\mathbf{x}^{-1}\mathbf{s}$ is a constant;

$$\begin{aligned}\mathrm{var}[T(\mathbf{x});H_0] &= E\left[\left(\mathrm{Re}\{\mathbf{s}^H\mathbf{R}_\mathbf{x}^{-1}\mathbf{x_n}\}\right)^2\right] - \left(E\left[\mathrm{Re}\{\mathbf{s}^H\mathbf{R}_\mathbf{x}^{-1}\mathbf{x_n}\}\right]\right)^2 \\ &= \mathrm{Re}\left\{E[\mathbf{s}^H\mathbf{R}_\mathbf{x}^{-1}\mathbf{x_n}\mathbf{x_n^H}\mathbf{R}_\mathbf{x}^{-1}\mathbf{s}]\right\} \\ &= \mathrm{Re}\left\{\mathbf{s}^H\mathbf{R}_\mathbf{x}^{-1}E[\mathbf{x_n}\mathbf{x_n^H}]\mathbf{R}_\mathbf{x}^{-1}\mathbf{s}\right\} \\ &= \mathrm{Re}\left\{\mathbf{s}^H\mathbf{R}_\mathbf{x}^{-1}\mathbf{s}\right\}\end{aligned} \tag{2.53}$$

and

$$\begin{aligned}\mathrm{var}[T(\mathbf{x});H_1] &= E\left[\left(\mathrm{Re}\{\mathbf{s}^H\mathbf{R}_\mathbf{x}^{-1}(\mathbf{s}+\mathbf{x_n})\}\right)^2\right] - \left(E\left[\mathrm{Re}\{\mathbf{s}^H\mathbf{R}_\mathbf{x}^{-1}(\mathbf{s}+\mathbf{x_n})\}\right]\right)^2 \\ &= \mathrm{Re}\left\{E\left[\left(\mathbf{s^H}\mathbf{R}_\mathbf{x}^{-1}\mathbf{s}+\mathbf{s}^H\mathbf{R}_\mathbf{x}^{-1}\mathbf{x_n}\right)^2\right]\right\} - \left(\mathrm{Re}\left\{\mathbf{s^H}\mathbf{R}_\mathbf{x}^{-1}\mathbf{s}\right\}\right)^2 \\ &= \mathrm{Re}\left\{E\left[\left(\mathbf{s}^H\mathbf{R}_\mathbf{x}^{-1}\mathbf{x_n}\right)^2\right]\right\} + 2\,\mathrm{Re}\left\{\mathbf{s^H}\mathbf{R}_\mathbf{x}^{-1}\mathbf{s}\right\}\mathrm{Re}\left\{E[\mathbf{s}^H\mathbf{R}_\mathbf{x}^{-1}\mathbf{x_n}]\right\} \\ &= \mathrm{Re}\left\{\mathbf{s}^H\mathbf{R}_\mathbf{x}^{-1}\mathbf{s}\right\}\end{aligned} \tag{2.54}$$

Substituting these statistics into the expression for PFA, the threshold may be found as follows:

$$P_{FA} \equiv \int_{\eta'}^{\infty} \frac{1}{\sqrt{2\pi}\sigma_T} e^{-\frac{1}{2\sigma_T^2}(t-\mu_T)^2}\,dt \tag{2.55}$$

where $\sigma_T \equiv \sqrt{\mathrm{var}[T(\mathbf{x});H_0]}$ and $\mu_T \equiv E\left[\mathrm{var}[T(\mathbf{x});H_0]\right]$.

There is no closed form solution for this integral, however, it may be evaluated by using tables of a related integral, the *complementary cumulative distribution function*, or *Q-function*, which is defined as

$$Q(\gamma) \equiv \int_{\gamma}^{\infty} \frac{1}{\sqrt{2\pi}} e^{-\frac{1}{2}t^2}\,dt\,. \tag{2.56}$$

Rewriting (2.55) in terms of the Q-function,

$$P_{FA} = Q\left(\frac{\eta' - \mu_T}{\sigma_T}\right), \tag{2.57}$$

from which the threshold may be determined to be

$$\eta' = \mu_T + \sigma_T Q^{-1}(P_{FA}) = \sqrt{\mathrm{Re}\{s^H R_x^{-1} s\}} \cdot Q^{-1}(P_{FA}). \tag{2.58}$$

2.3.2 Detection of Signals with Unknown Parameters

In typical radar systems, the assumptions made in Section 2.3.1 are generally not valid; namely, neither the expected target return nor the interference is exactly known. In the most general case, nothing about the signal may be known at all, and it may be desired to detect simply the presence of any disturbance (other than noise) in the data. Fortunately, in radar, we know that our received signal will be a time-delayed and frequency-shifted version of our transmitted waveform. For example, Eq. (2.8) is an accurate expression for a point target. Although most real-world objects are not point targets, usually (2.8) is still used for detector design as a reasonable approximation to the true target waveform. Even so, many of the parameters in (2.8) are not known, leading to uncertainty in the signal amplitude, time delay, and frequency.

There are two major approaches to such composite hypothesis testing problems. The first, known as the Bayesian approach, considers the unknown parameters as realizations of random variables and assigns to each unknown parameter a prior PDF. Under each hypothesis, these parameters may or may not be the same. We define the unknown parameter vector as ξ_0 under H_0 and ξ_1 under H_1. Forming the likelihood ratio test, the optimal detector then decides H_1 if

$$\frac{p(\mathbf{x}; H_1)}{p(\mathbf{x}; H_0)} = \frac{\int p_{\mathbf{x}}(\mathbf{x} \mid \boldsymbol{\xi_1}; H_1) p(\boldsymbol{\xi_1}) d\boldsymbol{\xi_1}}{\int p_{\mathbf{x}}(\mathbf{x} \mid \boldsymbol{\xi_0}; H_0) p(\boldsymbol{\xi_0}) d\boldsymbol{\xi_0}} > \eta'. \tag{2.59}$$

Although this formulation seems simple enough, there are several issues which make its implementation difficult. First, the required integrations are multidimensional with dimension equal to the number of unknown parameters. In radar, there can easily be

three or more unknown parameters, leading to quite complex and computationally intensive integrals. Second, the choice of prior PDFs can be difficult. If there is prior knowledge about the distribution of an unknown parameter, this can be used in selecting the PDF used in modeling. Oftentimes, there is little knowledge and a non-informative PDF such as the uniform PDF, or more commonly, the Gaussian PDF must be used.

The second major approach to detecting a signal with unknown parameters is the generalized likelihood ratio test (GLRT), which first estimates the unknown parameters and then forms the likelihood ratio test. Typically, maximum likelihood estimates (MLE) are used, so that the GLRT may be mathematically expressed as

$$\frac{p_{\mathbf{x}}\left(\mathbf{x} \mid \hat{\boldsymbol{\xi}}_{\mathbf{1}}; H_1\right)}{p_{\mathbf{x}}\left(\mathbf{x} \mid \hat{\boldsymbol{\xi}}_{\mathbf{0}}; H_0\right)} > \eta' . \tag{2.60}$$

Analytically speaking, the GLRT is not an optimal solution; however, for practical problems it has been seen to work well and is the basis for many radar detector designs, as illustrated in [51].

2.3.3 Performance Measures

The performance of radar detectors is typically given using *receiver operating characteristic* (ROC) curves, such as the probability of detection versus the probability of false alarm or *signal-to-noise ratio* (SNR). For the detector described in Section 2.3.1, its ROC curve may be calculated as follows:

$$P_D = \Pr\{T(\mathbf{x}) > \eta' \mid H_1\} = Q\left\{\frac{\eta' - E[T(\mathbf{x}); H_1]}{\mathrm{var}[T(\mathbf{x}); H_1]}\right\}. \tag{2.61}$$

Substituting (2.52), (2.54), and (2.58), we obtain the expression for P_D vs. P_{FA} as

$$P_D = Q\left\{Q^{-1}(P_{FA}) - \sqrt{\mathrm{Re}\{\mathbf{s}^H \mathbf{R}_{\mathbf{x}}^{-1} \mathbf{s}\}}\right\}. \tag{2.62}$$

Note that the detector of Section 2.3.1 is in fact a *matched filter*, i.e. a filter designed to maximize the SNR at its output. When the measured radar data exactly matches the expected target return, the maximum output SNR may be found as follows:

$$SNR \equiv \frac{E[\mathbf{w}^H \mathbf{s}\mathbf{s}^H \mathbf{w}]}{E[\mathbf{w}^H \mathbf{x_n}\mathbf{x_n}^H \mathbf{w}]} \tag{2.63}$$

If we assume that the noise has a covariance matrix of $\sigma_n^2 \mathbf{I}$ and set $\boldsymbol{w} = \boldsymbol{s}$,

$$SNR_0\big|_{\mathbf{w}=\mathbf{s}} = \frac{1}{\sigma_n^2}\mathbf{s}^H\mathbf{s}\,. \tag{2.64}$$

Thus, the ROC curve may also be rewritten in terms of maximum output SNR:

$$P_D = Q\left\{Q^{-1}(P_{FA}) - \sqrt{SNR_0\,|_{\mathbf{w}=\mathbf{s}}}\right\}. \tag{2.65}$$

As an example, let us set $\sigma_n^2 = 1$ for simplicity and plot the resulting ROC curves (Fig. 2.13). An important point to notice is that improving the output SNR also improves the detection performance. The output SNR may be increased by making one or more of many possible radar system changes, such as greater transmitter power, a larger antenna gain, smaller range coverage, or minimizing detector SNR loss. In the above example, we've assumed that the received data exactly matches the expected target return. In fact, as mentioned previously, the expected target return is not exactly known.

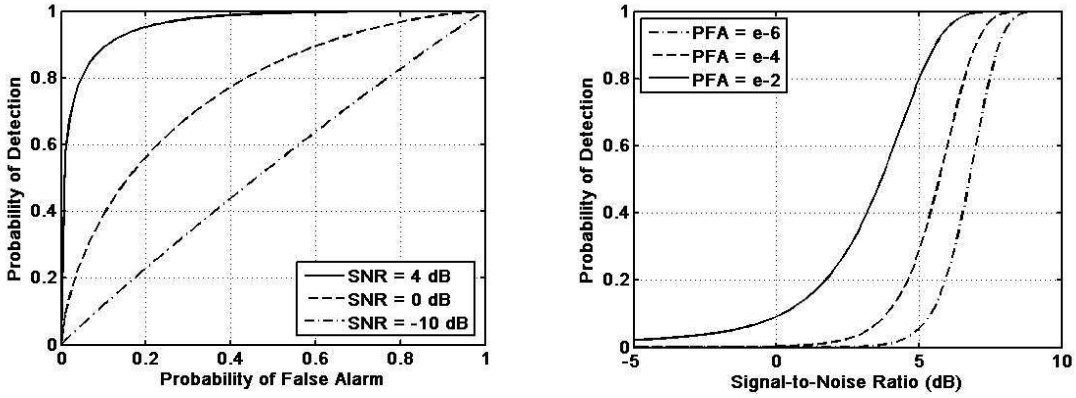

(a) (b)

Figure 2.13: Example ROC curves. (a) P_D vs. P_{FA}, (b) P_D. vs. SNR.

Differences between the modeled waveform and true return and errors in parameter estimates will result in a discrepancy between the data and filter weights, resulting in a sub-optimal matched filter response and a loss (relative to ideal) in output SNR.

Minimizing detector SNR loss is a key aspect of detector design that will be discussed in greater detail in this thesis, especially in regards to detector design tailor to human targets.

2.4 Parameter Estimation Theory

Another important goal of radar, other than detection, is to determine the location and velocity of detected targets. The location, or range (*R*), is calculated from time delay (t_d) as $R = \frac{ct_d}{2}$, while the target velocity can be found from Doppler shift (Δf) as $v = \frac{c|\Delta f|}{4\pi f_c}$. Although after pulse compression and Doppler processing the time delay and Doppler shift may seem to be known, in fact, they are only known to within the limits of the range or Doppler bin in which the true peak lies. Even determination of this bin is made uncertain by noise and interference. Thus, the time delay and Doppler shift are in fact unknown parameters that must be estimated from the data.

Usually, the estimator is designed to be both unbiased and to have minimum variance. An estimator is said to be unbiased if on average the estimator yields the true value of the unknown parameter. Mathematically, an estimator is unbiased if $E\left(\hat{\xi}\right) = \xi$ for $a < \xi < b$, where *(a, b)* denotes the range of possible values of ξ.

One approach for calculating a minimum variance estimator is to minimize the mean-square error (MSE), defined as $mse\left(\hat{\xi}\right) = E\left[\left(\hat{\xi} - \xi\right)^2\right]$. The MSE of an unbiased estimator is just the variance, thus minimizing the MSE is then equivalent to minimizing the variance and leads to a *minimum variance unbiased* (MVU) estimator. In practice, however, MMSE estimators are oftentimes not realizable. Although there are other techniques for computing MVU estimators [49][52], in general the MVU estimator does not always exist.

In such cases, an estimator based on the maximum likelihood principle may be derived. The maximum likelihood estimate (MLE) for a scalar parameter ξ is defined to be the value of ξ that maximizes $p(\boldsymbol{x};\xi)$ for $\boldsymbol{x}$ fixed; in other words, the value that maximizes the likelihood function. Maximum likelihood estimation is perhaps the most popular approach for obtaining practical estimators and is a "turn-the-crank," straightforward procedure that can be applied to even the most complicated estimation problems. Furthermore, the performance of an MLE approaches the optimum for large amounts of data.

2.5 Factors Affecting Radar Performance

There are several factors that affect radar performance, some of which are design parameters and some of which are external affects:

1. Transmitter power
2. Target radar cross section
3. Receiver sensitivity and noise factor
4. Frequency of operation
5. Atmospheric conditions
6. Pulse repetition frequency
7. Pulse duration
8. Interference
9. Electronic countermeasures

The transmitter power directly affects the amplitude of the received radar return, as modeled by the radar range equation. Even with the most concentrated radar beam, only a fraction of the transmitted energy strikes the target. Furthermore, depending on the target RCS, only a fraction of this incident energy is reflected back to the radar. For example, a vehicle has a higher RCS than a human, which is actually somewhat of an absorber, and, thus, has a higher amplitude return signal, leading to easier detection. If

the transmitter power is limited and cannot be increased, the radar range must be decreased to detect the weaker targets.

Receiver noise is another factor inhibiting the detection of weak signals. If the input SNR of the receiver is too low or the electronic noise caused by the receiver's own hardware is too strong, then weak target returns could be masked and go undetected. Radar pulses are typically of very short duration and thus high bandwidth; however, typically the higher the bandwidth, the greater the receiver noise.

The frequency of operation is also a key factor in radar performance, as atmospheric absorption and the RCS of most targets varies with frequency. For example, the atmosphere more easily absorbs higher frequency signals, resulting in increased atmospheric losses and decreased received signal energy.

The pulse repetition interval (PRI) and pulse duration directly impact the range over which targets may be detected. The maximum range is determined by the PRI, as the transmitted signal must travel to the farthest point and return back to the radar before the next pulse transmitted. Similarly, the pulse duration limits the minimum range. Most radars do not simultaneously transmit and receive, so that the earliest a return can be measured is immediately after the pulse has been transmitted. Anything arriving sooner will not be detected, so the minimum range is given by the round-trip distance traveled over the pulse duration.

Finally, interference has the potential to mask target returns. The signal transmitted by the radar reflects not just off the target of interest, but off everything in the environment, including buildings, trees, and cars. Such environmental interference is termed *clutter* and can be significantly different in terms of strength and nature depending on the terrain. For example, targets that are easily detectable in the desert may be masked by trees and other foliage in the woods. But clutter is not the only potential source of interference. In hostile environments, the use of jammers – devices specifically designed to prevent target detection – by adversaries may inhibit detection of critical targets. Much research has been done to negate the effects of jammers and mitigate or cancel clutter.

CHAPTER 3

RADAR SIGNAL MODELING

In general, the target echo is a time-delayed, frequency-shifted version of the transmitted chirp signal. Thus, the baseband return for a point target may be expressed as

$$s_r(n,t) = a_t rect\left(\frac{\hat{t} - t_d}{\tau}\right) e^{j[-2\pi f_c t_d + \pi\gamma(\hat{t} - t_d)^2]}, \tag{3.1}$$

where the time t is defined as $t = T(n-1) + \hat{t}$ in terms of the pulse repetition interval (PRI), T, the pulse number n, and the time relative to the start of each PRI $\hat{t}$; a_t is the amplitude as given by the radar range equation; τ is the pulse width; c is the speed of light; γ is the chirp slope; f_c is the transmitted center frequency; and t_d is the round trip time delay between antenna and target, defined in terms of the target range, R, as $t_d = 2R/c$.

However, the signal measured by the radar is not comprised just of the target return, but of other sources of interference, such as receiver noise, or reflections from objects in the environment (clutter). The received signal may be represented as the sum of the signals from all of these sources:

$$\mathbf{x} = \mathbf{s_r} + \mathbf{x_c} + \mathbf{x_n}, \tag{3. 2}$$

where $\boldsymbol{s_r}$ is the human target return, $\boldsymbol{x_c}$ is the clutter signal and $\boldsymbol{x_n}$ is noise. Noise is typically modeled as having a Gaussian distribution. Modeling of the human and clutter signals is considered next.

3.1 HUMAN MODEL

Humans are complicated targets because of the intricate motion of body parts moving along different trajectories at different speeds. Human kinematic modeling is made even more difficult as there are a plethora of differing human motions, which all

have drastically different kinematics, such as running [53][54], walking, jumping, swimming, crawling, or playing golf [55]. Even within the same class of motion, such as walking for instance, simply carrying a load [56-58] or walking in a circular [59], as opposed to linear, trajectory can change the kinematics. In this work, we refine our scope by specifically considering walking, the most basic human motion.

Over the years much research has been done to analyze and mathematically model human walking [26][60-63]. The model developed by Boulic, Thalmann and Thalmann [26] (henceforth referred to as the "Thalmann model") is used here to determine target range profiles since this model was one of the first complete walking models, is relatively easy to implement, and has been shown to be applicable in radar by Van Dorp [13] who compared measured and modeled human spectrograms.

The work of Geisheimer [20][21] and Van Dorp [13] showed that a human target could be divided into parts and the total response obtained by simply summing the responses of each part – i.e., the principle of superposition could be applied to human modeling. Thus, the radar return from a human target may be mathematically modeled as

$$s_h(n,t) = \sum_{i=1}^{K} a_{t,i}\, rect\left(\frac{\hat{t} - t_{d,i}}{\tau}\right) e^{j[-2\pi f_c t_{d,i} + \pi\gamma(\hat{t} - t_{d,i})^2]}, \tag{3.3}$$

where K is the number of point targets comprising the overall human target. In this work, the human body is divided into twelve basic body parts: the head, upper arms, lower arms, torso, thighs, lower legs and feet. As indicated in Fig. 3.1, each point target is taken to lie at the center of the corresponding body part.

The amplitude $a_{t,i}$, defined from the range equation as

$$a_{t,i} = \frac{G\lambda\sqrt{P_t\sigma_i}\sigma_n}{(4\pi)^{1.5} R_i^2 \sqrt{L_s}\sqrt{L_a}\sqrt{T_{sys}}}, \tag{3.4}$$

includes several factors that vary with target range R_i, and geometry. For instance, the antenna gain G varies according to angle of incidence, and the atmospheric losses L_a vary with range. For simplicity, we assume that these parameters are constant, along

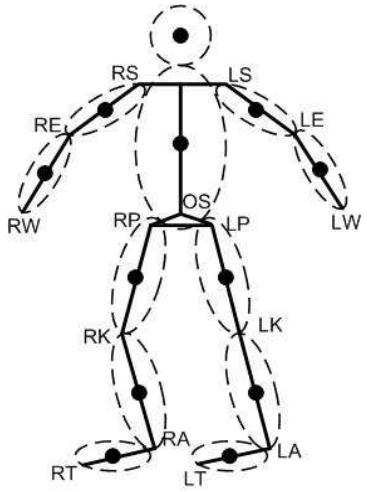

Figure 3.1: 12-point human model [35].

with the transmitted signal power P_t, the wavelength λ, the system loss L_s, the system temperature T_{sys}, and the noise standard deviation σ_n. Modeling the radar cross section (RCS) σ_i, however, is not a trivial task and is worthy of more detailed consideration.

3.1.1 Human Radar Cross-Section Modeling

When the electromagnetic wave from a radar strikes an object, radar waves are reflected in all directions. How much energy goes in each direction depends on a variety of factors, such as the shape of the object, the material composing the object, the type, frequency and polarization of the radar, and the angle of incidence. The RCS can be physically interpreted as the antenna gain times the target's effective cross section and is mathematically given by the expression [64]

$$RCS = \lim_{R\to\infty} 4\pi R^2 \left|\frac{E_r}{E_i}\right|^2, \tag{3.5}$$

where E_i is the incident field strength at the target and E_r is the field strength of the scattered field at range R.

Human RCS is difficult to ascertain as a person's posture, relative orientation, wave incidence angle, and distance to the radar are constantly changing in the course of

walking (or any other type of motion). Moreover, human sizes can significantly vary, from that of a small child to that of a tall man. Even the type of material a person is wearing can affect the reflectivity properties and observed RCS.

There have been few studies of human RCS. In 2005, Yamada, Tanaka and Nishikawa [65] performed a study quantitatively examining the properties of human RCS in the band of 76 GHz. They found that human RCS varied with orientation. As one would intuitively expect, reflections from the front and back were higher than those from the side. While the average reflection intensity was found to be -8.1 dBsm, the distribution of the variance over orientation had a spread of more than 20 dB. Furthermore, the type of clothes worn also had a significant impact on reflectivity (Fig. 3.2). Even whether a shirt was wrinkled or not affected the RCS measurements: wrinkled shirts exhibited higher reflections that greatly varied with orientation. Overall, measurements showed that reflections from human targets were about 15-20 dB less than those from the rear end of a vehicle. Thus, humans in general have a low RCS, and generate much weaker target returns, making them more difficult to detect.

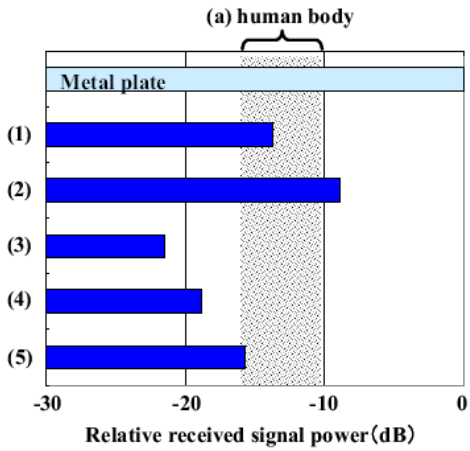

Figure 3.2: Measurement result for reflectivity of clothes: (1) 100% cotton undershirt, (2) 50% polyester, 50% cotton T-shirt, (3) wool sweater, (4) 100% nylon windbreaker, and (5) 45% cotton, 55% polyester work jacket [65].

In 2007, researchers from the Sensors and Electronics Directorate of the Army Research Laboratory applied computational electromagnetic models of the human body to conduct numerical computer simulations of the human body radar signature,

analyzing the human RCS in different configurations as functions of aspect angle, frequency and polarization [66]. A number of important conclusions were made based on these simulations and the ones most relevant to this work are:

- The RCS of the body as seen from the front varies between -10 and 0 dBsm;
- The kneeling position produces more RCS variations with azimuth angle than that of a person standing, as there are a larger number of scattering centers in the former case.
- There is a strong return from the back, as the body torso is more or less flat from that angle, creating a larger RCS as compared to the more curved surfaces characteristic to other parts of the body.
- Angular RCS variation becomes more rapid as the transmitted radar frequency increases.
- The average RCS remains in a tight range of -4 to 0 dBsm for almost all frequencies and all body positions, possibly because the main contribution to the radar return is from the torso.
- Body shape does not have a major influence on average RCS, although there is thought to be a dependence on overall body size.
- Elevation angle can result in increased RCS, especially in the case of V-V polarization, as the body increasingly forms a “corner” resulting in higher reflections.

Additionally, some statistical studies [66] were conducted using these computer models to derive the probability distribution of the RCS for a single human measured from the ground plane, i.e. zero elevation angle. In particular, for low frequencies the RCS was found to follow a Swerling Case 3 distribution,

$$p(\sigma) = \frac{4\sigma}{\sigma_a} e^{-\frac{2\sigma}{\sigma_a}}, \tag{3.6}$$

where σ is the human RCS and σ_a is the average human RCS. While for high frequencies, the distribution more resembled a Swerling Case 1 distribution:

$$p(\sigma) = \frac{1}{\sigma_a} e^{-\frac{\sigma}{\sigma_a}}. \tag{3.7}$$

The transition between these two cases occurred between 1 and 2 GHz, although body position affected the exact transition frequency. For example, the transition for a kneeling man occurred at a lower frequency than that of a standing man, who continued to exhibit Swerling Case 3 properties at 1.8 GHz.

Despite these initial results, which just begin to give us an understanding of the RCS characteristics of humans, much research remains to be done to completely define and model human RCS. Further work is particularly needed for the cases of airborne applications, where elevation angle has a great impact; and varying target motions, since position influences the RCS distribution.

Most researchers to date have simply used a variety of probabilistic or engineering approximations to RCS. Geisheimer [20] approximated the RCS of each body part by weighting each according to a percentage of overall surface area. Naturally, the reflectivity of each body part may change depending on density, size, shape, and incidence angle. For instance, the reflectivity of the head may be significant when compared to that of the torso, despite the difference in size. Therefore, in this work we choose to apply the RCS model used by Van Dorp [13], which takes into account all of the above mentioned factors with the exception of density.

Each body part is approximated in shape by either a sphere or a cylinder, whose analytical expressions also account for size and incidence angle. For a sphere with radius R_s (m)

$$\sqrt{\sigma_s} = R_s \sqrt{\pi} \left[\left(1 + \frac{\lambda}{j 4\pi R_s} \right) e^{-j\left(\frac{4\pi R_s}{\lambda}\right)} - \frac{\lambda}{j 4\pi R_s} \right]. \tag{3.8}$$

For a cylinder with radius R_c (m), height H_c (m), and broadside incidence angle θ_c (rad)

$$\sqrt{\sigma_c} = -jH_c\sqrt{\cos(\theta_c)\frac{2\pi R_c}{\lambda}}\,\mathrm{sinc}\left(\frac{2\pi H_c}{\lambda}\sin\theta_c\right)e^{j\frac{2\pi}{\lambda}(r+R_c\cos\theta_c)}e^{j\frac{\pi}{4}}, \qquad (3.9)$$

where *r* is the range to the target from the radar. A Swerling 0, or constant non-fluctuating model for the RCS is used as no definitive studies have been done on the RCS of individual body parts and the overall RCS of the human shows small variation over a range of angles [66].

3.1.2 Thalmann Kinematic Walking Model

The Thalmann walking model is based on experimental biomechanical data. The human body is represented as a "stick figure," with lines linking the main joints of the human body. The change of the angles between various links as well as the translation of the origin OS (see Fig. 3.1) is provided over the duration of one cycle (two steps), since, thereafter, the walking motion is assumed to repeat identically.

Periodic Trajectories Situating the Body

The expressions in (3.10) to (3.12) describe the motion of the designated origin, OS, over the duration of one cycle (two steps). The translations are expressed as an offset from the initial position of OS (the height of the spine). Thus, a "vertical translation" describes an up or down motion, a "lateral translation" describes motion to the left or right, perpendicular to the direction of walking, and a "forward/backward translation" describes motion along or in reverse to the direction of walking. Notice that in this model the coefficients in (3.10) to (3.12) remain constant for all humans. The variation of human size is accounted for the variable RV, the relative velocity of the human, defined as the absolute velocity divided by the height of the thighs. The time variable, t_n, is also a normalized parameter, defined as the absolute time divided by the overall duration of one cycle. For illustration, these equations are plotted for RV=1 in Fig. 3.3.

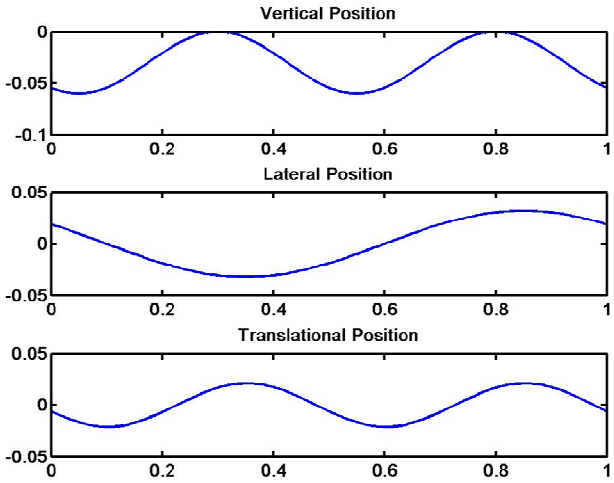

Figure 3.3: Vertical, lateral, and forward/backward translations of OS over one walking cycle for RV=1.

Vertical Translation:

$$\Delta_{v,OS} = 0.015RV\sin(2t_n - 0.35) \tag{3.10}$$

Lateral Translation:

$$\Delta_{t,OS} = \begin{cases} -0.032\sin(2\pi(t_n - 1)), & RV > 0.5 \\ 0.128RV(1-RV)\sin(2\pi(t_n - 1)), & RV < 0.5 \end{cases} \tag{3.11}$$

Forward/Backward Translation:

$$\begin{aligned} &\Delta_{fb,OS} = A\sin(2t_n + 2\phi) \\ &\text{where } A = \begin{cases} -0.021 & RV > 0.5 \\ 0.084RV(1-RV) & RV < 0.5 \end{cases} \\ &\text{and } \quad \phi = 0.625 - \mathrm{Ds_n} \end{aligned} \tag{3.12}$$

Ds_n is defined as the relative duration of support; in other words, the ratio of the time that one foot supports the body in contact with the floor to the total duration of the cycle. Ds_n may be mathematically expressed in terms of the relative velocity using relationships defined in Thalmann's paper [26] as follows:

$$\text{Relative length of cycle, } RLc \equiv 1.346\sqrt{RV} \tag{3.13}$$

$$\text{Duration of cycle, } Dc \equiv \frac{RLc}{RV} \tag{3.14}$$

$$\text{Duration of support, } Ds \equiv 0.752Dc - 0.143 \tag{3.15}$$

$$\text{Relative duration of support, } Ds_n \equiv \frac{Ds}{Dc} \tag{3.16}$$

Thus,

$$Ds_n = 0.752 - 0.10624\sqrt{RV} \tag{3.17}$$

Periodic Trajectories of the Hip, Knee, and Shoulder

Thalmann provides several charts to describe the angular rotation of the hip (angle of the line RP-RK or LP-LK relative to a vertical), knee (angle of the line RK-RA or LK-LA relative to a vertical), and shoulder (angle of line RS-RE or LS-LE relative to a vertical). From these charts, the trajectories of the angular motion over one walking cycle for a range of walking speeds can be derived. Fig. 3.4 illustrates these trajectories calculated for a speed of 2 m/s.

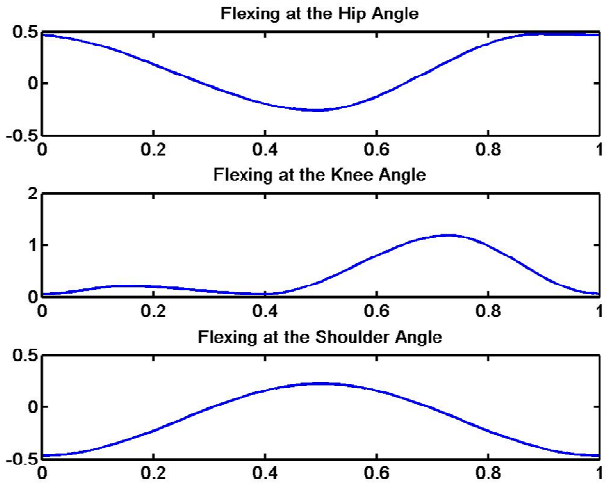

Figure 3.4: Angular rotations of the hip, knee and shoulder over one walking cycle.

Periodic Trajectories of the Elbow, Angle, and Thorax

Trajectories for the angular rotation of the elbow (given by the angle between the line RE-RW or LE-LW and the vertical), elbow (given by the angle between the line RA-RT or LA-LT and the vertical), and thorax (torsion relative to OS) calculated for a walking speed of 2 m/s are given in Fig. 3.5.

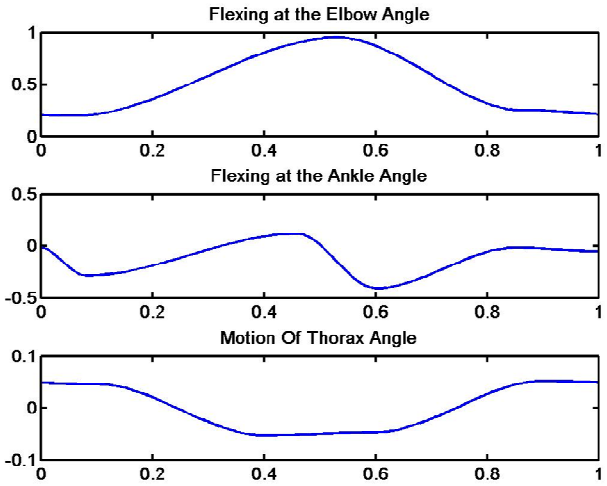

Figure 3.5: Angular rotation of the elbow, ankle, and thorax over one walking cycle.

Dimensions of the human body parts may then be used in conjunction with these time-varying joint angles to compute the time-varying positions relative to OS. A listing of the body part dimensions used in this work may be found in Table 3.1. Because overall human heights vary according to a Gaussian distribution, the distributions of the body part dimensions are also assumed to be Gaussian. The dimensions for any desired human may be found by interpolating as follows:

Define

$$k = \Phi(x) = \frac{1}{2\pi} \int_{-\infty}^{x} e^{-\frac{t^2}{2}} dt . \tag{3.18}$$

Thus, for the 95th percentile, k=0.95. Then, $x = \Phi^{-1}(k)$ and the dimension of any body part is given as

$$d_{bp} = \mu_{bp} + x\sigma_{bp}, \tag{3.19}$$

where μ_{bp} and σ_{bp} are the mean and variance of the distribution of that body part, as calculated from the values of the 95%ile and 5%ile sizes.

Note that all the equations and charts used in Thalmann's model ultimately depend on just two parameters: the walking speed (*V*) and height of thigh (*HT*). As a result, these two features are of especial interest when considering the human detection and identification problem.

Table 3.1: Human Physical Dimensions [67]

(meters)	95% Male	5% Male	95% Female	5% Female
Initial OS	1.180	1.005	1.085	0.930
Height of Thigh	1.000	0.840	0.885	0.740
Torso Height	0.505	0.390	0.460	0.360
Head Height	0.205	0.180	0.190	0.165
Hip Width	0.405	0.310	0.435	0.310
Hip Height	0.295	0.195	0.280	0.185
Thigh Height	0.550	0.440	0.530	0.435
Lower Leg Length	0.490	0.395	0.445	0.355
Foot Length	0.285	0.240	0.255	0.215
Shoulder Length	0.215	0.1825	0.1925	0.1625
Shoulder-Elbow Length	0.395	0.330	0.360	0.300
Elbow-Wrist Length	0.305	0.265	0.270	0.240
Torso Diameter	0.357	0.290	0.340	0.2675
Upper Arm Diameter	0.095	0.080	0.085	0.070
Lower Arm Diameter	0.07125	0.060	0.06375	0.0525
Thigh Diameter	0.185	0.135	0.180	0.125
Leg Diameter	0.1387	0.1013	0.135	0.9375
Foot Diameter	0.110	0.085	0.100	0.080

3.1.3 Pulse Compressed Human Signal Model

The human target return defined in (3.3) is used to generate simulated radar data in MATLAB. The slow-time, fast-time data matrix is then pulse compressed so that the peak occurs at the range bin in which the target is present. The pulse compression output is defined as a matched filter with a time-reversed replica of the transmitted signal, i.e. $h(t) = e^{-j\pi\gamma t^2}$. Thus, for a single body part,

$$\begin{aligned} x(t) &= \int_{-\infty}^{\infty} s_r(u) h(t-u) du \\ &= \int_{t_d}^{t_d+\tau} a_t e^{j\left(-2\pi f_c t_d + \pi\gamma(u-t_d)^2\right)} e^{-j\pi\gamma(t-s)^2} du \end{aligned} \tag{3.20}$$

The peak occurs when $t = t_d$:

$$\begin{aligned} x_{peak} &= x(t_d) \\ &= \int_{t_d}^{t_d+\tau} a_t e^{j\left[-2\pi f_c t_d + \pi\gamma(u-t_d)^2\right]} e^{-j\pi\gamma(t_d-u)^2} du \\ &= \int_{t_d}^{t_d+\tau} a_t e^{-j2\pi f_c t_d} du \\ &= a_t \tau e^{-j2\pi f_c t_d} \end{aligned} \tag{3.21}$$

Summing the pulse compressed output for each body part, and substituting the expression for time delay in terms of range,

$$x_p[n] = \sum_{i=1}^{12} a_{t,i} \tau e^{-j\frac{4\pi f_c}{c} R_i[n]}. \tag{3.22}$$

Eq. (3.22) is the analytical form of the slow-time cross-section that is the starting point for data processing and the input signal to human detection algorithms.

3.1.4 Human Spectrograms

Although spectrograms are not directly used in this work, some observations about human spectrograms will be useful in understanding the proposed detector

design. The spectrogram of a human target may be computed by stacking the fast Fourier transforms (FFT) of short, overlapping time segments taken from the slow-time slice in (3.22). An example of the simulated spectrogram for a human target is shown in Fig. 3.6. Work by Van Dorp [13][28] has shown that simulated spectrograms based on the Thalmann model closely match those measured experimentally, thereby validating the kinematic model.

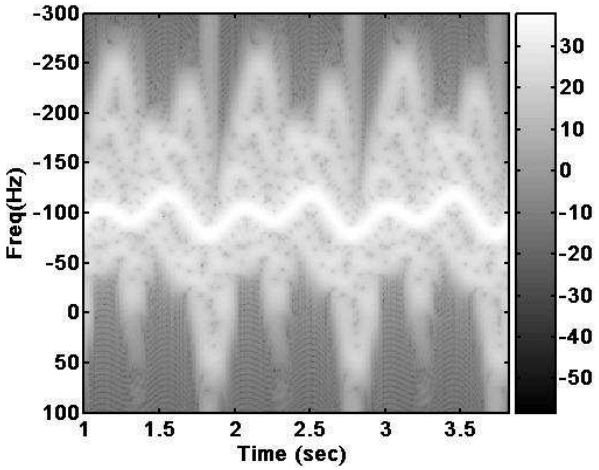

Figure 3.6: Simulated human spectrogram.

The strongest return is received from the torso, with its low-frequency, small-amplitude sinusoidal oscillatory motion. The appendages that travel the farthest during the walking cycle – the feet – appear in the spectrogram with the largest amplitude oscillation. Note that the special nature of the periodicities within the human spectrogram are what makes this response unique and differentiable from the spectrograms of even other animals, as can be seen from the measured spectrograms of a human and dog given by Otero in [22]. Our knowledge of this unique structure of human motion will be exploited in our proposed detector design.

3.2 CLUTTER MODEL

Clutter is defined as any unwanted radar return. For example, when searching for vehicles, the return from buildings, rocks, grass, asphalt, trees – in short, any object other than a vehicle in the scene – is summed to form the clutter return. Thus, the nature of clutter varies depending on the application and the specifications of the radar. The presence or absence of foliage, geography, whether the scene is open terrain or a city environment, whether the radar operates from an airborne platform or under the sea – all these and many more factors affect the characteristics and modeling of clutter.

If we assume that the scene is homogeneous and comprised of a large number of independent scatterers, then according to the Central Limit Theorem, we can model their sum as a Gaussian random variable. Due to the homogeneity assumption, the standard deviation (σ_c) of the Gaussian is constant.

While the Gaussian model is the most basic and generic of probabilistic clutter models, many other distributions have been proposed to approximate other clutter characteristics, such as the tail of the measured clutter density, heterogeneity, specular reflections, or when the grazing angle is small. Examples include, but are not limited to, the noncentral chi-square, Weibull, lognormal, compound-K, compound Gaussian, noncentral gamma (NCG), and noncentral gamma gamma (NCGG) distributions [68-70].

Aside from such probabilistic models, another ubiquitous model is a General Ground Clutter Model that computes the sum of all the clutter returns from a ring of scatterers located at a fixed range, R_c, about the radar (Fig. 3.7). The return from a discrete clutter scatterer has the same form as the target echo; namely, a time-delayed and frequency-shifted version of the transmitted signal. However, the received amplitude will be affected by the clutter RCS, and, since the ground inherently has zero velocity, the relative velocity and hence, relative Doppler of a clutter patch depends only on this patch's location and velocity relative to the radar platform.

Unlike a target, ground clutter returns are distributed in range. However, for the purposes of this work, we are primarily concerned with the clutter contribution within a single range bin, as we've assumed our target motion to be confined to one range bin.

In addition to the returns from the iso-range or clutter ring corresponding to the target location, returns from all ambiguous ranges must also be taken into account. Define N_r to be the number of range ambiguities, and N_c to be the number of clutter patches comprising the clutter ring.

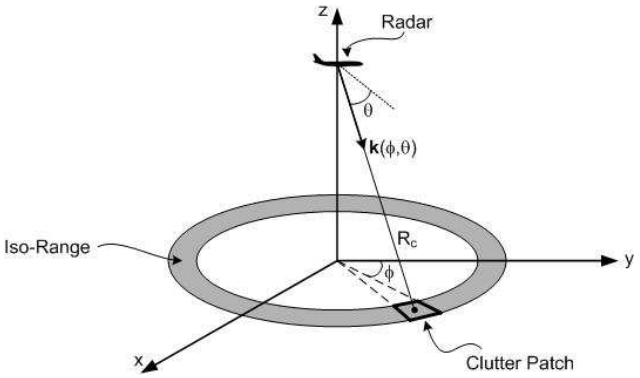

Fig. 3.7: Geometry of ground clutter for a fixed range.

For a sidelooking array, the spatial frequency of the ik^{th} clutter patch is a function of its azimuth angle ϕ_k and elevation angle θ_i as follows.

$$\vartheta_{ik} = \frac{\mathbf{k}(\phi_k, \theta_i) \cdot \mathbf{d}}{\lambda} = \frac{d}{\lambda} \cos\theta_i \sin\phi_k \,, \tag{3.23}$$

Where ***k*** is a unit vector pointing from the platform to the center of the ik^{th} clutter patch; ***d*** is a vector pointing from the first to last array element, i.e. perpendicular to the array normal; d is the array element spacing; and λ is the wavelength.

Similarly, the Doppler frequency of the return from this patch is defined by

$$f_{D,ik} = \frac{2\mathbf{k}(\phi_k, \theta_i) \cdot \mathbf{v_a}}{\lambda} \,, \tag{3.24}$$

where $\boldsymbol{v_a}$ is the velocity vector of the radar platform. If we assume a side-mounted array with no crab, then the velocity vector will be aligned with the array axis and may be expressed as $\boldsymbol{v_a} = v_a \boldsymbol{x}$. Then, the Doppler frequency becomes

$$f_{D,ik} = \frac{2v_a}{\lambda}\cos\theta_i \sin\phi_k . \tag{3.25}$$

Combining (3.23) and (3.25), the normalized Doppler may be expressed in terms of the spatial frequency as

$$\varpi_{ik} = f_{D,ik} PRI = \frac{2v_a}{\lambda} PRI \frac{\vartheta_{ik}\lambda}{d} = \frac{2v_a PRI}{d}\vartheta_{ik} , \tag{3.26}$$

Thus, in angle-Doppler space, the clutter falls along a straight line of slope $2v_a PRI / d$, typically referred to as the clutter ridge, as illustrated in Fig. 3.8.

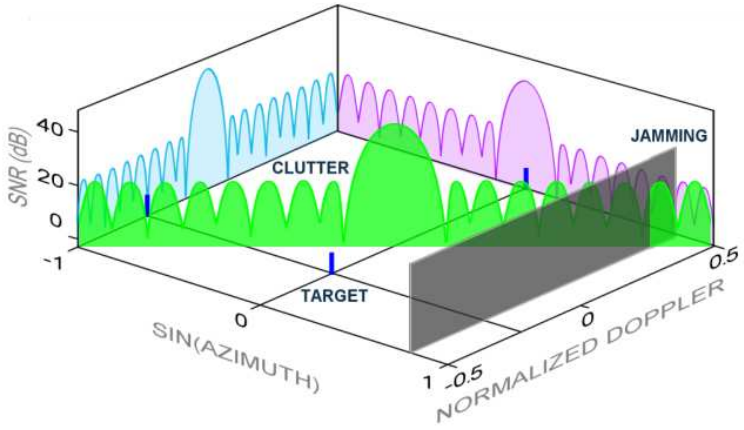

Fig. 3.8: Power spectral density of the interference (clutter and jamming) seen by an airborne radar [71].

Furthermore, the clutter component of the space-time snapshot is

$$\boldsymbol{\chi}_c = \sum_{i=1}^{N_r}\sum_{k=1}^{N_c} \alpha_{ik}\mathbf{v}(\vartheta_{ik}, \varpi_{ik}) , \tag{3.27}$$

where α_{ik} is a random amplitude that may be found by modulating the radar range equation as

$$\alpha_{ik} = \eta \frac{G\lambda\sqrt{P_t\sigma_{ik}}}{(4\pi)^{3/2} R_c^2 \sqrt{L_s L_a}} \sigma_n . \tag{3.28}$$

Here, η is a zero-mean complex Gaussian random variable, G is the antenna gain, P_t is the transmitted power, L_s represents system losses, L_a indicates atmospheric losses, σ_n is the noise standard deviation, and σ_{ik} is the RCS of the ik^{th} clutter patch. The clutter RCS is typically computed using the constant gamma model as

$$\sigma_{ik} = \sigma_0 \Delta A = \gamma \sin\psi_c \Delta A, \tag{3.29}$$

where σ_0 is the area reflectivity of the ground at the ik^{th} patch, γ is a terrain-dependent parameter, ψ_c is the grazing angle and ΔA is the patch area.

Observe that the clutter power is

$$E\left[\left|\alpha_{ik}\right|^2\right] = \left| \frac{G\lambda\sqrt{P_t\sigma_{ik}}}{(4\pi)^{3/2} R_c^2 \sqrt{L_s L_a}} \right|^2 \sigma_n^2 . \tag{3.30}$$

Thus, the clutter-to-noise ratio (CNR) may be found to be

$$CNR = \frac{G^2\lambda^2 P_t \sigma_{ik}}{(4\pi)^3 R_c^4 L_s L_a} . \tag{3.31}$$

CHAPTER 4

PROBLEM ASSESSMENT: THE EFFECTS OF NONLINEAR PHASE

There are several disadvantages to current Fourier-based human detection techniques. First, when multiple human targets are located in the same range bin, as often occurs in practical surveillance scenarios, their spectrograms overlap, making it difficult to perform any kind of feature extraction or target characterization.

Second, the linear nature of Fourier-based detectors is mismatched to the non-linear phase history of real human targets, resulting in an inherent SNR loss in the detector itself. Consider the phase history of a typical human target walking at an incidence angle maximally aligned to the initial antenna-target vector, as shown in Fig. 4.1.

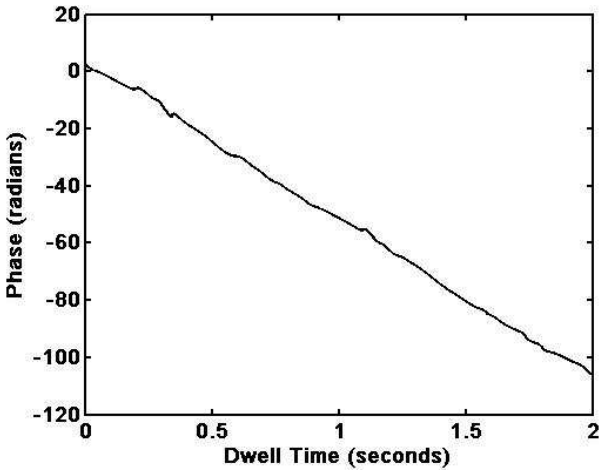

Figure 4.1: Phase history of a typical human target walking along a vector maximally aligned with the initial antenna-target vector.

At first glance, the phase does not appear to be highly non-linear, and the FFT would seem to be a good match. In fact, as shown in Chapter 5, for human targets the phase history is comprised of a linear as well as oscillatory component. Subtracting out the linear component of the phase in Fig.4.1, the oscillatory components are revealed (Fig.4.2).

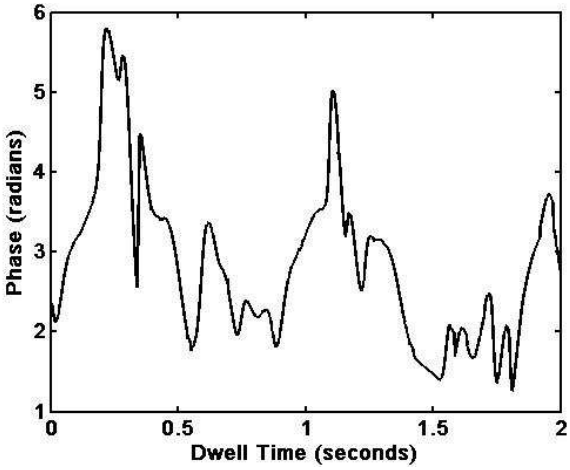

Figure 4.2: Phase history of Fig. 4.1 after linear component is removed.

The SNR loss incurred may be quantitatively analyzed as follows. Define the true target data as

$$\mathbf{s} = \begin{bmatrix} \alpha_0 & \alpha_1 e^{j\theta_1} & \cdots & \alpha_{N-1} e^{j(N-1)\theta_{N-1}} \end{bmatrix}^T, \tag{4.1}$$

where N is the total number of pulses transmitted, and α_i and θ_i are generalized amplitude and phase factors, respectively. Note that in general both the amplitude and phase factors vary with slow-time (*n*).

When ***s*** is filtered with a signal ***w***, the output SNR is

$$SNR = \frac{E[\mathbf{w^H s s^H w}]}{E[\mathbf{w^H x_n x_n^H w}]}, \tag{4.2}$$

where $\boldsymbol{x_n}$ is the noise signal. If we assume that the noise has a covariance matrix of $\sigma_n^2 \mathbf{I}$, then (4.2) may be simplified to

$$SNR = \frac{\left|\mathbf{w^H s}\right|^2}{\sigma_n^2 \left|\mathbf{w^H w}\right|}, \tag{4.3}$$

The maximum output SNR is attained when the received signal ***s*** is matched filtered against itself:

$$SNR_0\big|_{\mathbf{w}=\mathbf{s}} = \frac{1}{\sigma_N^2}\mathbf{s}^{\mathbf{H}}\mathbf{s}\,. \tag{4.4}$$

However, since knowing the target return exactly in advance is impossible, current systems typically match filter with a linear phase filter, which may be expressed as

$$\mathbf{w_{LIN}} = \begin{bmatrix}\beta_1 & \beta_2 e^{j\phi} & \cdots & \beta_{N-1}e^{j(N-1)\phi}\end{bmatrix}^T, \tag{4.5}$$

where β_i and ϕ are generalized amplitude and phase parameters, respectively. Here, the amplitude factor is left in a general form that varies with slow-time, while only the phase has been restricted to be linear. The output SNR for such a linear phase filter is

$$SNR_{LIN}\big|_{\mathbf{w}=\mathbf{w}_{\mathbf{LIN}}} = \frac{\left|\mathbf{w}_{\mathbf{LIN}}^{\mathbf{H}}\mathbf{s}\right|^2}{\sigma_N^2\left|\sum_{n=0}^{N-1}\beta_n^2\right|}. \tag{4.6}$$

Thus, the SNR loss incurred from signal mismatch is

$$SNR\ Loss = \frac{SNR_{LIN}}{SNR_0} = \frac{\left|\mathbf{w}_{\mathbf{LIN}}^{\mathbf{H}}\mathbf{s}\right|^2}{\left|\sum_{n=0}^{N-1}|\beta_n|^2\right|\mathbf{s}^{\mathbf{H}}\mathbf{s}} < 1 \tag{4.7}$$

Note that a SNR loss of 1 corresponds to no loss, a situation only possible when the filter is perfectly matched to the target return.

There are three main factors which impact SNR loss: phase mismatch, amplitude mismatch, and dwell time. Fig. 4.3 illustrates the affect of these factors by applying Fourier processing on the example phase history of Fig. 4.1, which has an amplitude variation of $2.64\text{x}10^{-7}\pm2.5\text{x}10^{-7}$ over a 2 second dwell. The FFT computes a

constant, flat-line approximation to the true amplitude, i.e. $\beta_n=\beta$ for all n. However, the amplitude mismatch – defined as the SNR loss incurred due to amplitude differences, assuming identical phase – is not nearly as significant as the phase mismatch. Over a 2 second dwell, the phase moves through 100 radians, or 5732 degrees, of phase. However, just a 1% error in the slope causes the phase to shift by 2π, an entire cycle. Thus, unlike the amplitude, phase is extremely sensitive to mismatch. Despite the gross linear appearance of the phase history, the underlying nonlinearities that are invisible to the naked eye in fact result in SNR losses of up to 30 dB for a 2 second dwell time!

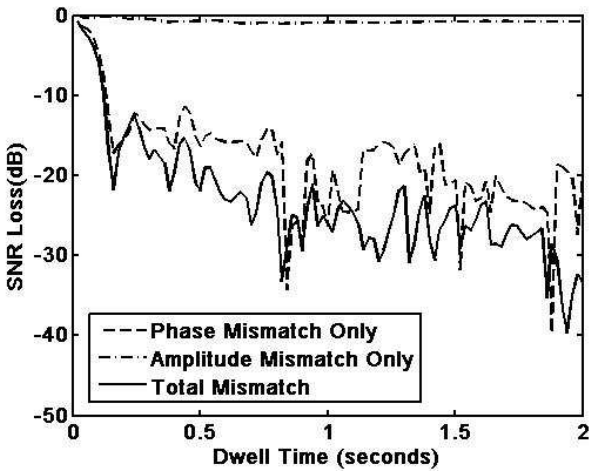

Figure 4.3: SNR Loss variation over dwell time for the target phase history shown in Fig. 4.1.

Collecting data over a longer dwell, so that the integration gain increases, also does not help alleviate the inherent SNR loss in Fourier-based, linear phase detectors. Consider the plot in Fig. 4.4, which shows the trend of the output SNR normalized by the input signal SNR ($|\mathbf{s}|^2/\sigma_n^2$) as dwell time is increased for both the ideal, clairvoyant detector and the FFT. While the output SNR continually increases with dwell for the clairvoyant detector, the FFT exhibits on average a flat trend, so that the output SNR does not significantly increase with dwell time. Indeed, the SNR loss, as shown by the

difference between the two curves in Fig.4.4, simply increases with dwell.

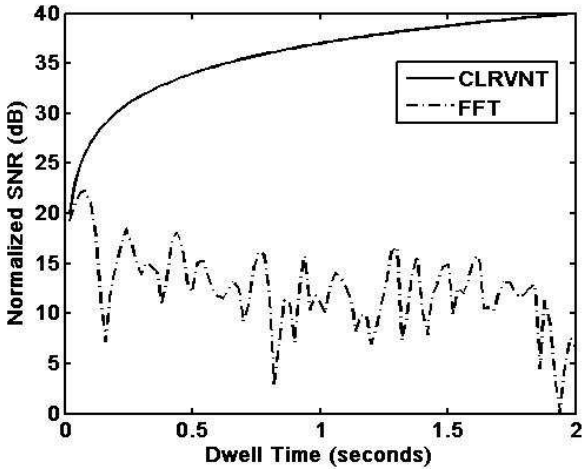

Figure 4.4: Output SNR variation over dwell time normalized by input SNR for the target phase history shown in Fig. 4.1 comparing clairvoyant and FFT-based detectors.

Thus, matched filtering with a more accurate model of the signal phase history has the potential to yield a significant reduction in output SNR losses and, thereby, substantially improve detection performance. For this same example, the model-based optimized nonlinear phase (ONLP) detector proposed for single-channel SAR exhibits an SNR loss of only 7 dB for a 2 second dwell time. The next chapter discusses in detail the design and performance of the proposed ONLP detector.

CHAPTER 5

SINGLE-CHANNEL DETECTOR DESIGN

For each range bin centered at r_b, the detector must make a decision between two hypotheses:

$$\begin{aligned} H_0 &: \quad \mathbf{x} = \mathbf{x_n} \\ H_1 &: \quad \mathbf{x} = \mathbf{s} + \mathbf{x_n}, \end{aligned} \tag{5.1}$$

where $\boldsymbol{x_n}$ is complex Gaussian interference with covariance matrix $\boldsymbol{R_I}$, $\boldsymbol{s}$ is the true target signal, and we've assumed that there is no range migration, i.e., that the entire target return is contained within one range bin. Here, we are modeling the interference as being homogeneous and comprised of a fixed number of independent scatterers. By the central limit theorem, the probability density is assumed to be Gaussian. Because of the assumption of homogeneity, the standard deviation of this Gaussian distribution is constant. However, since the interference covariance matrix cannot be known a priori, an estimate must be used instead. In this work, we assume clairvoyance and the noise-limited case:

$$\hat{\mathbf{R}}_\mathbf{I} = \mathbf{R}_\mathbf{I} = \sigma_n^2 \mathbf{I} \tag{5.2}$$

where σ_n^2 is the interference power and $\hat{\mathbf{R}}_\mathbf{I}$ is an estimate of the true covariance matrix $\boldsymbol{R_I}$. Achieving acceptable performance in the noise limited case is necessary before considering the more general cases for $\boldsymbol{R_I}$, and has practical significance for a number of radar configurations.

A likelihood ratio test is used to determine the detector decision rule. Under H_0, the disturbance is distributed as $CN(0, \hat{\mathbf{R}}_\mathbf{I})$ while under H_1 the distribution of the disturbance is $CN(s, \hat{\mathbf{R}}_\mathbf{I})$, where $\boldsymbol{s}=\boldsymbol{x_p}$ is the target signal vector. Thus the decision rule may be expressed as

$$\text{Decide } \mathrm{H}_1 \text{ if } \frac{p(\mathbf{x}; H_1)}{p(\mathbf{x}; H_0)} > \gamma \rightarrow \mathrm{Re}\left\{\mathbf{s}^\mathbf{H} \hat{\mathbf{R}}_\mathbf{I}^{-1} \mathbf{x}\right\} > \gamma', \tag{5.3}$$

where $\gamma' = \sqrt{\mathrm{Re}\{\mathbf{s}^{\mathbf{H}}\hat{\mathbf{R}}_{\mathbf{I}}^{-\mathbf{1}}\mathbf{s}\}} \cdot Q^{-1}(P_{FA})$ and P_{FA} is the desired probability of false alarm.

Since the target return, **s**, is not known a priori, a realizable detector must use an approximation. Our goal in this work is to develop a better approximation to the target return than that of the linear-phase FFT, so as to minimize SNR loss and achieve better detection performance.

The human-model based expression for the target return in (3.22) is a very good approximation to the true target signal, **s**; however, this model is much too complicated for use as an effective matched filter. The model contains over 24 unknown parameters, and most of the kinematic expressions used to compute the time-varying range of each body part are not presented in closed form but, rather, as graphs, which must be combined with other charts or equations to derive the time-varying position [26]. Thus, we next derive a simpler, non-linear approximation to (3.22) that will serve as the basis for our proposed optimized non-linear phase (ONLP) detector.

5.1 APPROXIMATING THE EXPECTED TARGET RETURN

As shown in Fig. 3.6, the torso response is significantly stronger than the response from the remaining eleven body parts comprising the model, so we will simplify first by neglecting the motion of all body parts except the torso. That is, we will design the detector to match as best as possible the response from the torso only.

Furthermore, since the overall SNR loss is caused primarily by phase mismatch, we will approximate the received signal amplitude, a_t, as a being constant, A, even though there is some variation across slow-time due to slight variations in gain, RCS, and other loss factors. We also approximate the range term in the amplitude factor of (3.22) with r_b, the center of the range bin at which the peak pulse compression output occurred.

For the range term in the phase, however, we cannot make as crude an approximation, because the phase is much more sensitive to errors than the amplitude. A more accurate approximation to range is obtained as follows.

Define $\boldsymbol{r_1}$ as the vector from the antenna to the target's initial position and $\boldsymbol{r_N}$ as the vector from the antenna to the target's final position. For simplicity, assume that the human motion is linear along a constant angle, θ, relative to $\boldsymbol{r_1}$. Then, the vector $\boldsymbol{h}$ between the initial and final target locations represents the human motion (Fig. 5.1).

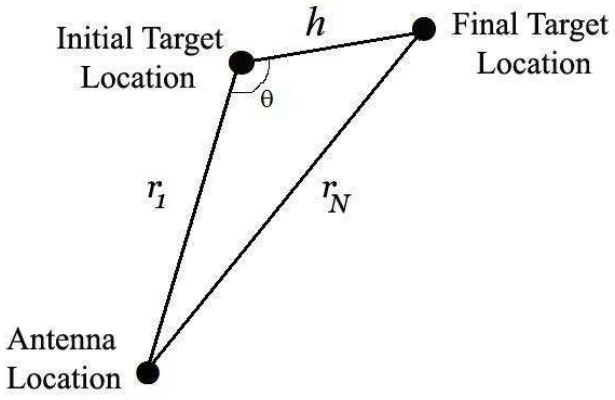

Figure 5.1: Antenna-target geometry.

Using the law of cosines, we may write

$$|\mathbf{r_n}|^2 = |\mathbf{r}_1|^2 + |\mathbf{h}|^2 - 2|\mathbf{r_1}||\mathbf{h}|\cos\theta\,. \tag{5.4}$$

Since in our application we assume $|\mathbf{h}| << |\mathbf{r_1}|$ and $\sqrt{1+x} \approx 1 + x/2$ for small x,

$$|\mathbf{r_n}| \approx |\mathbf{r_1}| - |\mathbf{h}|\cos\theta\,. \tag{5.5}$$

Then, (3.22) may be written as

$$x_p[n] \approx \frac{A}{r_b^2} e^{-j\frac{4\pi f_c}{c}(r - h\cos\theta)}, \tag{5.6}$$

where r = $|\mathbf{r_1}|$ and h = $|\mathbf{h}|$.

The human motion vector $\boldsymbol{h}$ may be more explicitly expressed using the Thalmann kinematic equations as

$$h^2 = OS_V^2 + OS_L^2 + (vTn + OS_{FB})^2, \tag{5.7}$$

where

$$OS_V = 0.015RV\left[-1+\sin\left(4\pi t\% - 0.7\pi\right)\right]$$

$$OS_L = A_L \sin\left(2\pi t\% - 0.2\pi\right)$$

$$A_L = \begin{cases} -0.032 & \text{for } 0.5 < RV < 2.3 \\ -0.128RV^2 + 0.128 & \text{for } RV < 0.5 \end{cases}$$

$$OS_{FB} = A_a \sin\left(4\pi t\% + 2\phi_a\right)$$

$$A_a = \begin{cases} -0.021 & \text{for } 0.5 < RV < 2.3 \\ -0.084RV^2 + 0.084RV & \text{for } RV < 0.5 \end{cases}$$

$$\phi_a = -0.127 + 0.731\sqrt{RV}$$

Here, OS_L, OS_V, and OS_{FB} represent the lateral, vertical and forward/backward motion of the center of the torso relative to coordinate origin of OS (see Fig. 3.1) located at the base of the spine. The Thalmann equations depend on only two variables: 1) *RV*, the ratio of velocity (*v*) to thigh height (*HT*); and, 2) *t%*, a time index taken relative to the beginning of a step. These variables may be expressed as

$$RV = \frac{v}{HT}, \text{ and} \tag{5.8}$$

$$t\% = \frac{nT}{1.346}\sqrt{RV} + t_0, \tag{5.9}$$

where t_0 is a constant indicating the point within the stepping cycle that the first transmitted pulse reflects from the target.

The expression for *h* may be simplified by neglecting second order terms and approximating the square root as

$$h \approx \sqrt{(vTn)^2 + 2vTnOS_{FB}} = vTn\sqrt{1+\frac{2OS_{FB}}{vTn}} \approx vTn + OS_{FB}. \tag{5.10}$$

This equation is consistent with the phase histories plotted previously in Fig. 4.1 and Fig. 4.2. For small radial velocities, *v*, the oscillatory term dominates, whereas for large *v*, the linear term dominates.

Although generally speaking the phase will contain multiple sinusoids as a result of the quadratic components we previously neglected in (5.7), too detailed a model will

render the detector fragile under noise, so just one sinusoid is used as a nonlinear approximation to the true target phase.

Then, the ONLP approximation to the true target phase can be found by substituting (5.10) into (5.6) and grouping coefficients as

$$x_{onlp}[n] = \frac{A}{r_b^2} e^{j\left(Mn + C_1 + C_2 \cos(C_3 n + C_4)\right)} \tag{5.11}$$

with M, the slope proportional to Doppler frequency; C_1, a factor dependent upon range; C_2, the amplitude of torso motion; C_3, torso frequency; C_4, torso phase; and, A, the amplitude as defined in the range equation. These variables are unknown model parameters over which the matched filter response will be optimized.

5.2 ESTIMATING MODEL PARAMETERS

The maximum likelihood estimate (MLE) for any parameter ξ_i in a signal ***x*** with mean *m* in complex Gaussian noise may be represented as [52]

$$\frac{\partial \ln\left(p(\mathbf{x};\boldsymbol{\xi})\right)}{\partial \xi_i} = 2\,\mathrm{Re}\left\{\left(\mathbf{x} - \mu(\boldsymbol{\xi})\right)^H \mathbf{C}_\mathbf{x}^{-1} \frac{\partial \mu(\boldsymbol{\xi})}{\partial \xi_i}\right\} \tag{5.12}$$

For the detection problem described in (5.1), the signal mean under H_1 is simply the expected target return, $\boldsymbol{x_{onlp}}$. Let's first compute the MLE estimate for the unknown amplitude, ξ_i = A.

$$\frac{\partial \mu}{\partial A} = \frac{\partial x_{onlp}}{\partial A} = \frac{1}{r_b^2} e^{j\angle x_{onlp}} \tag{5.13}$$

Thus, we set

$$\frac{\partial \ln\left(p(\mathbf{x};A)\right)}{\partial A} = \frac{2\,\mathrm{Re}\left\{\mathbf{x}^H e^{-j\angle \mathbf{x}_{\mathbf{onlp}}} - \dfrac{AN}{r_b^2}\right\}}{\sigma_n^2 r_b^2} = 0, \tag{5.14}$$

which in turn can be solved to find the MLE:

$$\hat{A} = \frac{r_b^2}{N}\,\mathrm{Re}\left\{\mathbf{x}^H e^{-j\angle \mathbf{x}_{\mathbf{onlp}}}\right\}. \tag{5.15}$$

Although (5.12) may also be used to estimate the phase parameters, the resulting estimate is not numerically robust. Thus, the MLE for the phase parameters are instead found by first explicitly extracting the phase data. The phase of a complex signal may be found by taking the ratio of the imaginary and real parts. However, this operation also transforms the disturbance distribution from complex Gaussian to Cauchy, so that the detection problem may be restated as follows:

$$\begin{aligned} \widetilde{H}_0 &: \quad \widetilde{\mathbf{x}} = \widetilde{\mathbf{x}}_{\mathbf{n}} \\ \widetilde{H}_1 &: \quad \widetilde{\mathbf{x}} = \tan\left(\angle \mathbf{x}_{\mathbf{onlp}}\right) + \widetilde{\mathbf{x}}_{\mathbf{n}}, \end{aligned} \tag{5.16}$$

where $\widetilde{\mathbf{x}}_{\mathbf{n}}$ is Cauchy distributed noise.

Define the variance of the imaginary and real parts of the zero-mean, complex Gaussian noise $\boldsymbol{x_n}$ as σ_i and σ_r, respectively. Then, the Cauchy distribution for a single sample with $\sigma_i \neq 1$, $\sigma_r \neq 1$, and correlation coefficient $\rho \neq 0$ is

$$p(\widetilde{x}_n) = \frac{1}{\pi} \frac{\beta}{(\widetilde{x}_n - \alpha)^2 + \beta^2}, \tag{5.17}$$

here $\alpha = \rho \frac{\sigma_{\mathrm{i}}}{\sigma_{\mathrm{r}}}$ and $\beta = \frac{\sigma_{\mathrm{i}}}{\sigma_{\mathrm{r}}} \sqrt{1-\rho^2}$. Since we assume $\sigma_i = \sigma_r$ and that the real and imaginary parts of the noise are uncorrelated, i.e. ρ=0, the joint distribution for N samples of $\widetilde{\mathbf{x}}$ under H_1 may be computed to be

$$p\left(\widetilde{\mathbf{x}}; \tan(\angle \mathbf{x}_{\mathbf{onlp}})\right) = \frac{1/\pi^N}{\prod_{m=0}^{N-1} \left[1 + \left(\widetilde{x}_m - \tan(\angle x_{onlp,m})\right)^2\right]}, \tag{5.18}$$

where $\widetilde{x}_m \equiv [\widetilde{\mathbf{x}}]_m$, the m[th] element of $\widetilde{\mathbf{x}}$.

The MLE for an unknown parameter ξ_i is given by solving the following equation for each ξ_i:

$$\frac{\partial}{\partial \xi_i} \ln p\left(\widetilde{\mathbf{x}}; \tan(\angle \mathbf{x}_{\mathbf{onlp}})\right) = 0. \tag{5.19}$$

Substituting (5.18) into (5.19),

$$\begin{aligned}\frac{\partial}{\partial \xi_i}\ln p\left(\tilde{\mathbf{x}};\tan(\angle \mathbf{x}_{\mathbf{onlp}})\right) &= \frac{\partial}{\partial \xi_i}\left\{-N\ln(\pi)-\sum_{m=0}^{N-1}\ln\left[1+\left(\tilde{x}_m-\tan(\angle x_{onlp,m})\right)^2\right]\right\} \\ &= \sum_{m=0}^{N-1}\frac{\tilde{x}_m-\tan(\angle x_{onlp,m})}{1+\left(\tilde{x}_m-\tan(\angle x_{onlp,m})\right)^2}\frac{\partial}{\partial \xi_i}\tan(\angle x_{onlp,m})=0\end{aligned} \tag{5.20}$$

Note that when the tangent of the phase of the ONLP model exactly matches that of the data, $\tilde{x}_m-\tan\left(\angle x_{onlp,m}\right)=0$ and (5.20) is satisfied. Thus, (5.20) can be physically interpreted as merely a condition selecting the unknown parameters ξ_i such that the phase mismatch is minimized.

Computing the MLE estimates for all 5 phase parameters thus requires solving a system of 5 nonlinear equations, which is impossible to do in closed form, and very computational and memory intensive even when solved numerically. Therefore, we break the problem into two stages by first estimating the linear component, and then estimating the non-linear term.

The linear term may be estimated as follows. If in (5.7) we model the human motion as being simply that of a constant-velocity point target, then $h=nvT$ and

$$x_p[n]\approx\frac{A}{r_b^2}e^{-j\frac{4\pi f_c}{c}(r-nTv_r)}, \tag{5.21}$$

where $v_r=v\cos\theta$. The two unknown linear phase parameters *r* and v_r may then be found by solving the least squares problem $\mathbf{A}\boldsymbol{\xi}=\mathbf{b}$ as

$$\hat{\boldsymbol{\xi}}=\left(\mathbf{A}^T\mathbf{A}\right)^{-1}\mathbf{A}^T\mathbf{b}, \tag{5.22}$$

where

$$\begin{aligned}\mathbf{A} &= \frac{4\pi f_c}{c}\begin{bmatrix}T & 2T & \cdots & NT\\ -1 & -1 & \cdots & -1\end{bmatrix}^T \\ \hat{\boldsymbol{\xi}} &= \begin{bmatrix}r & v_r\end{bmatrix}^T \\ \mathbf{b} &= \begin{bmatrix}\tan^{-1}(\tilde{x}_1) & \tan^{-1}(\tilde{x}_2) & \cdots & \tan^{-1}(\tilde{x}_N)\end{bmatrix}^T\end{aligned} \tag{5.23}$$

An initial estimate of the slope M may then be found as

$$M_i = \frac{4\pi f_c}{c} T v_r = \frac{4\pi f_c}{c} T \hat{\xi}(2). \tag{5.24}$$

This initial estimate is then numerically refined so as to ensure no residual linear component remains.

Having computed an estimate for the slope M, the remaining parameters in the nonlinear component of the phase are estimated from (5.20), which is now reduced to a system of four nonlinear equations and four unknowns, solved using numerical iteration. Note that of these four parameters, the frequency and phase shift coefficients C_3 and C_4 are the most crucial for ensuring the best match between model and data. Thus, to save computation time, larger step sizes are used for C_1 and C_2, while finer step sizes are utilized for C_3 and C_4.

The final form of our proposed ONLP detector is

$$\mathrm{Re}\left\{\hat{\mathbf{x}}_{\mathbf{onlp}}^{\mathbf{H}} \hat{\mathbf{R}}_{\mathbf{I}}^{-\mathbf{1}} \mathbf{x}\right\} > \gamma', \tag{5.25}$$

where $\gamma' = \sqrt{\mathrm{Re}\{\hat{\mathbf{x}}_{\mathbf{onlp}}^{\mathbf{H}} \hat{\mathbf{R}}_{\mathbf{I}}^{-\mathbf{1}} \hat{\mathbf{x}}_{\mathbf{onlp}}\}} \cdot Q^{-1}(P_{FA})$ and $\hat{\mathbf{x}}_{\mathbf{onlp}}$ is the ONLP response with MLE parameters; (5.25) is still a linear detector as the elements of $\hat{\mathbf{x}}_{\mathbf{onlp}}$ merely form the weights with which we filter our signal.

5.3 QUALITY OF PARAMETER ESTIMATES

Obtaining adequate estimates of the unknown model parameters is critical to the performance of the matched filter detector. The estimation problem, however, is affected by several factors, including the direction of motion (i.e. target geometry), dwell time, and SNR.

As indicated in (5.10), the phase history of a human target may be represented as the sum of linear and oscillatory components. Depending on the target geometry and walking speed, the shape of the phase history may vary. Remember that a radar measures not absolute speed, but the radial speed in the direction of the radar. When

the target moves roughly perpendicular to the antenna-target vector, the radial velocity will be nearly zero and the oscillatory component is clearly apparent. As the target moves along the antenna-target vector, the radial velocity is almost identical to the true target velocity, so the linear component has more of an effect.

Dwell time is also an important factor, as the amount of data collected limits the number of cycles we can observe. For example, consider a human walking at 2 m/s, with waist oscillations (OS_{FB}) on the order of inches and a PRI of 0.2 ms, as in the example of Fig. 4.1. Then $h \approx 4\times10^{-4}\times n$ inches. When the number of transmitted pulses is 2500, the linear component contributes 1 m to the value of h, obscuring the effect of the oscillatory component. Indeed, as was seen in Fig. 4.1, the phase history looks roughly linear. Only after the linear component was removed were the oscillations apparent. On the other hand, for short dwells, such as 100 pulses, the linear term contributes only 0.04 m (~1.6 inches), a value on the same order as the oscillations.

Finally, SNR is also a critical factor, since as the disturbance level increases the true signal curvature is obscured, leading to degradation in the parameter estimates. For low SNRs, longer dwell times will be required for good parameter estimates.

The quality of the parameter estimates may be assessed using the Cramer-Rao Bound (CRB). For a general signal *x[n,θ]* in complex Gaussian noise with variance σ^2, the CRB is given by [47]

$$\begin{aligned} &\mathrm{var}\left(\hat{\theta}\right) \geq \left[\mathbf{I}^{-1}(\boldsymbol{\theta})\right]_{ij}, \text{ with} \\ &\mathbf{I}(\boldsymbol{\theta})\big|_{ij} = \frac{2}{\sigma^2}\mathrm{Re}\left\{\sum_{n=0}^{N-1}\frac{\partial x^H}{\partial\theta_i}\frac{\partial x}{\partial\theta_j}\right\}, \end{aligned} \tag{5.26}$$

where **I(θ)** is the Fisher information matrix. Evaluating (5.26) for the expression of $\boldsymbol{x}_{onlp}$ given in (5.11), the desired CRB may be analytically expressed as

$$\mathrm{var}\left(\hat{\boldsymbol{\theta}}\right) \geq diag\left\{\frac{1}{4\cdot SNR}\mathbf{B}^{-1}\left(\hat{\boldsymbol{\theta}}\right)\right\}, \tag{5.27}$$

where the pulse-wise SNR is defined as $A^2/2r_b^2\sigma^2$ and

$$B(\theta)=\begin{bmatrix} N & S_1 & C_2S_2 & C_2S_3 & 0 \\ S_1 & S_4 & C_2S_5 & C_2S_6 & 0 \\ C_2S_2 & C_2S_5 & C_2^2S_7 & C_2^2S_8 & 0 \\ C_2S_3 & C_2S_6 & C_2^2S_8 & C_2^2S_9 & 0 \\ 0 & 0 & 0 & 0 & \frac{N}{A^2} \end{bmatrix}$$

where

$$S_1 \equiv \sum_{n=0}^{N-1}\cos(C_3n+C_4);\quad S_2 \equiv \sum_{n=0}^{N-1}n\sin(C_3n+C_4);\quad S_3 \equiv \sum_{n=0}^{N-1}\sin(C_3n+C_4); \tag{5.28}$$

$$S_4 \equiv \sum_{n=0}^{N-1}\cos^2(C_3n+C_4);\quad S_5 \equiv \sum_{n=0}^{N-1}n\sin(C_3n+C_4)\cos(C_3n+C_4);$$

$$S_6 \equiv \sum_{n=0}^{N-1}\sin(C_3n+C_4)\cos(C_3n+C_4);\quad S_7 \equiv \sum_{n=0}^{N-1}n^2\sin^2(C_3n+C_4);$$

$$S_8 \equiv \sum_{n=0}^{N-1}n\sin^2(C_3n+C_4);\quad S_9 \equiv \sum_{n=0}^{N-1}\sin^2(C_3n+C_4).$$

,

In Fig. 5.2, the CRB for $\hat{C}_1$ is plotted together with the simulated variance of $\hat{C}_1$ under two cases: 1) The underlying data is exactly the same as the model $\mathbf{x}_{\mathbf{ONLP}}$ in (5.11) used to compute the CRB; and, 2) the underlying data is the synthetic human data representative of true human motion as given in (3.22).

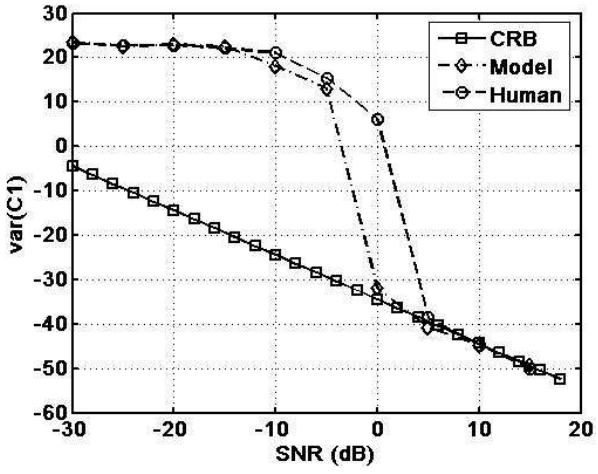

Figure 5.2: CRB and variance of parameter (C_1) MLE with ONLP approximation over 500 Monte Carlo trials.

The MLE estimator achieves the performance of the CRB for single-pulse SNRs above 5 dB. Notice that for intermediate SNR values, there is a slight difference between the simulated variances when the model data and synthetic human data are used. For example, when the underlying data exactly matches the model, the estimates follow the CRB for SNRs above 0 dB. This 5 dB difference illustrates the impact of modeling error on the estimates. However, the fact that the variances match for most SNRs also validates the quality of the ONLP model in terms of approximating the true data.

The dwell time – i.e., the number of pulses transmitted during the entire data collect times the PRI – also has a significant impact on the quality of the parameter estimates. As illustrated in Fig. 5.3, the longer the dwell time, the better the estimate. Thus, when the SNR is very low, as is typical of human targets, data must be collected for a much longer time to achieve comparable performance to targets with a higher SNR (or RCS). In this case, the estimate for the linear phase parameter, M, stabilizes after a 1.5 second dwell time when the SNR is 20 dB; but when the SNR is -20 dB, the estimate stabilizes after 2.4 seconds. In other words, for this particular example, to achieve the same quality of estimate, an additional 0.9 seconds of data must be collected.

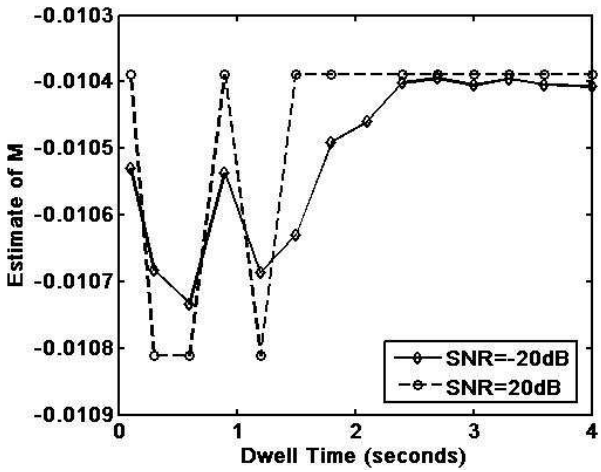

Figure 5.3: Variation of linear phase parameter, M: MLE versus number of pulses transmitted over 100 Monte Carlo runs.

5.4 PERFORMANCE

Detector performance is evaluated by applying the proposed ONLP detector to simulated radar data as generated in (3.22). The receiver operating characteristic (ROC) curves as well as the impact of SNR, incidence angle, and dwell time on the probability of detection (P_D) is assessed. By incidence angle, we mean the angle between the initial antenna-target vector and the target motion vector. Additionally, the effect on detection performance of multiple human targets within a single range bin is analyzed. The results presented in Fig. 5.4 – Fig. 5.9 are generated for radar with the characteristics shown in Table 5.1.

5.4.1 Receiver Operating Characteristics

ROC curves for the clairvoyant (i.e., perfectly matched, full knowledge of target), FFT, and ONLP detector are shown for a human target walking parallel to the x-axis and with an incidence angle of 135° in Fig. 5.4. The proposed ONLP detector exhibits similar performance to the ideal clairvoyant detector at a PFA of 0.5, whereas the FFT never approaches ideal performance until the PFA is about 1. The ONLP performance exceeds that of the FFT for all PFAs.

Table 5.1: Single Channel Radar System Parameters

Parameters	**Value**
Center Frequency	1 GHz
Sampling Frequency	20 MHz
Bandwidth	10 MHz
Pulse Repetition Interval	0.2 ms
Pulse Width	40 μs
Transmit Power	1.8 kW
Nominal Range	8,760 m
Range Resolution	60 m

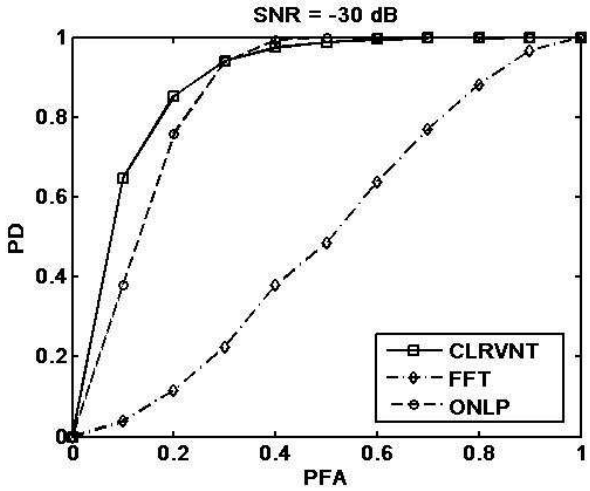

Figure 5.4. P_D vs. P_{FA} for a human target with an incidence angle of 135°, a dwell time of 0.5 s, and single-pulse SNR = -30dB.

5.4.2 Probability of Detection Versus SNR

The performance improvement of the proposed technique may also be seen in Fig. 5.5, which shows the affect of SNR on the probability of detection. The ONLP detector yields about an 11dB improvement in output SNR relative to the FFT.

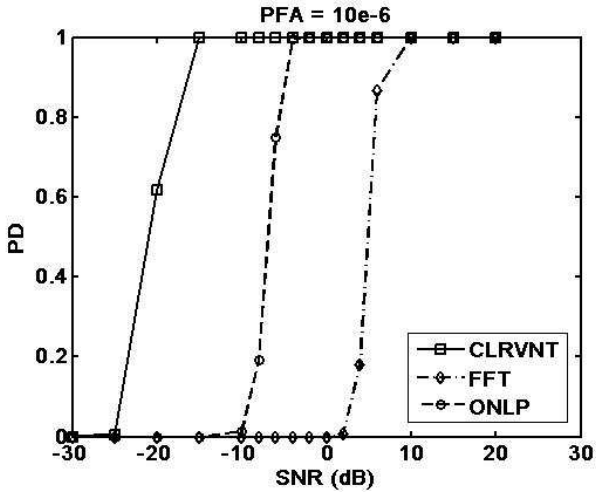

Figure 5.5. P_D vs. SNR for a human target with an incidence angle of 135°, a dwell time of 0.5 s, and $P_{FA}=10^{-6}$.

5.4.3 Impact of Target Motion on Detection

The ONLP method maintains this performance gain regardless of the target direction of motion. Fig. 5.6 shows the probability of detection variation over incidence angle for both FFT and ONLP methods. Note the performance of the FFT plummets as the target's motion increasingly aligns with the radar-target vector. Even a small error in estimating the phase history slope results in errors that accrue with dwell time and severely degrade performance. When the radial velocity is small, the phase history is predominantly sinusoidal and the phase mismatch errors are limited by the oscillation amplitude. Because the ONLP method optimizes the matched filter parameters, it maintains superior performance over all incidence angles.

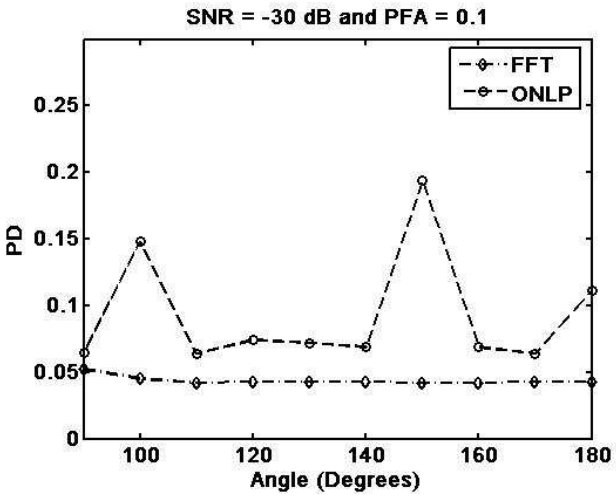

Figure 5.6. P_D vs. incidence angle for a human target with a dwell time of 0.5 s., SNR of -30dB, and P_{FA}=0.1.

5.4.4 Probability of Detection Versus Dwell Time

The impact of dwell time on detection performance is shown in Fig. 5.7. After a dwell of about 1.2 seconds, the proposed ONLP detector achieves the same performance as the ideal, clairvoyant detector. However, the FFT-based detector is unable to detect any targets even after twice the dwell time. This result is consistent with expectations, as the normalized output SNR versus dwell time plot of Fig. 4. also

showed that for human detection FFT-based detectors do not exhibit improved performance with dwell time. By making a significantly better matched filter, however, not only are we able to achieve better detection performance at a given dwell time, but we are now able to eventually achieve ideal performance given a sufficiently long dwell.

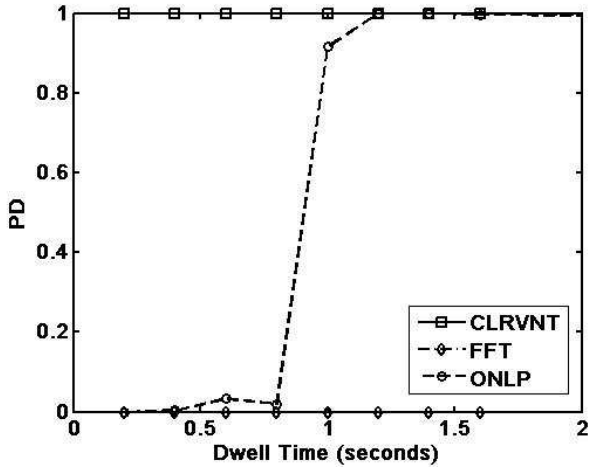

Figure 5.7. P_D vs. dwell time for a human target with an SNR of -10dB and $P_{FA}=10^{-6}$.

5.4.5 Multi-Target Situation

Up until now, results have been provided for the case when a single target resides in a single range bin. However, considering human social patterns, more than one human target occupying the same range-bin is very likely, causing the phase history to, in fact, contain the sum of the phase information of multiple human targets. In this situation, we define a detection as the simple indication of a target present, not the determination of the number of targets present.

Consider the case of three people starting at the same point, but walking in different directions: 45°, 0°, and -45° relative to x-axis. Then, the phase history obtained for a total number of 2,500 transmitted pulses consists of irregularly shaped oscillations, as shown in Fig. 5.8.

These irregularities do not significantly affect the detector design, as any nonlinearity is matched filtered with the best-fitting sinusoid and, thereby, achieves

improved detection performance, as shown in Fig. 5.9. Generally, the higher the number of targets in a range bin, the more complex and nonlinear the phase function. Although in an absolute sense, the degree to which the model matches the phase in the multi-target case may vary, the ONLP model will almost always better match the phase of – and thus outperform – the linear phase FFT.

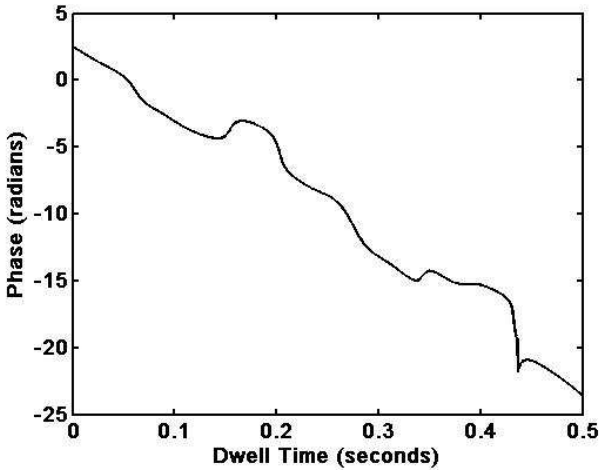

Figure 5.8: Phase history of three human targets walking in different directions within the same range bin.

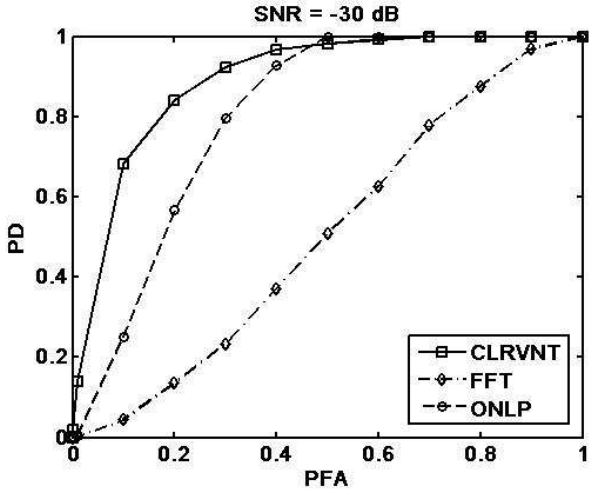

Figure 5.9: ROC curve comparing detector performance for the multi-target phase history of Fig. 5.8.

5.5 CONCLUSIONS

Thus, results show that the parameter estimation-based ONLP detector consistently outperforms conventional linear-phase matched filters, such as the FFT. Most importantly, the results confirm that our prior knowledge about human kinematics, and hence the structure of the expected human target return, can be used to improve detection performance.

However, the issue of detector performance in clutter remains to be addressed. For single-channel SAR systems, there is not much that can be done to mitigate the effect of clutter; however, by expanding to a multi-channel system, the clutter cancellation properties of space-time adaptive processing (STAP) may be exploited to achieve better performance. Here, a key question is how clutter affects the MLE estimates of unknown parameters and whether clutter cancellation sufficiently eradicates the clutter so as good estimates can be achieved.

In Chapter 6, the performance of the ONLP detector in clutter and with clutter cancellation is examined. An enhanced ONLP (EnONLP) detector is proposed that utilizes sparse approximation techniques to determine the best linear combination of possible target returns (i.e., dictionary entries) that matches the data. The performance of these two approaches (parameter estimation versus dictionary search) is compared in relation to conventional STAP processing.

CHAPTER 6

MULTICHANNEL DETECTOR DESIGN

Consider a multi-channel radar in which an antenna array with N antennas (i.e., channels) transmits a series of pulses at constant intervals in time and space while moving along a path. In general, the received signal is comprised of energy reflected by not just the desired target but by unwanted returns from other objects and the environment (clutter), and noise. Thus, the total space-time snapshot of the array at the target range gate may be mathematically expressed as

$$\boldsymbol{\chi} = \boldsymbol{\chi}_{\mathbf{t}} + \boldsymbol{\chi}_{\mathbf{c}} + \boldsymbol{\chi}_{\mathbf{n}}, \tag{6.1}$$

where $\boldsymbol{\chi}_t$ is the target space-time snapshot, $\boldsymbol{\chi}_c$ is the clutter space-time snapshot, and $\boldsymbol{\chi}_n$ is the noise space-time snapshot. The noise is modeled as being white complex Gaussian noise with variance σ_n^2. The human target and clutter models were derived in Chapter 3, but for convenience we repeat them here, extended to their multi-channel forms. From Section 3.2, (3.28)-(3.30),

$$\boldsymbol{\chi}_{\mathbf{c}} = \sum_{i=1}^{N_r}\sum_{k=1}^{N_c} \alpha_{ik}\mathbf{v}\left(\vartheta_{ik},\varpi_{ik}\right), \tag{6.2}$$

where α_{ik} is a random amplitude computed as

$$\alpha_{ik} = \eta\frac{G\lambda\sqrt{P_t\sigma_{ik}}}{(4\pi)^{3/2}R_c^2\sqrt{L_sL_a}}\sigma_n, \tag{6.3}$$

and η is a zero-mean complex Gaussian random variable, G is the antenna gain, P_t is the transmitted power, L_s represents system losses, L_a indicates atmospheric losses, σ_n is the noise standard deviation, and σ_{ik} is the RCS of the ik^{th} clutter patch, computed using the constant gamma model as

$$\sigma_{ik} = \sigma_0\Delta A = \gamma\sin\psi_c\Delta A, \tag{6.4}$$

where σ_0 is the area reflectivity of the ground at the ik^{th} patch, γ is a terrain-dependent parameter, ψ_c is the grazing angle and ΔA is the patch area.

Similarly, from Section 3.1, the multi-channel formulation of (3.22) may be obtained by incorporating the time delay Δt in the radar return between adjacent elements of the uniform linear array $\Delta t = d\sin(\phi)/c$, where d is the inter-element spacing, so that the radar return of a point target at the n[th] channel is

$$x_{p,n}(n,m) = x_p e^{-j\frac{f_c n d \sin(\phi)}{c}}, \tag{6.5}$$

where x_p is as defined for single-channel data in (3.22). Thus, the target contribution to the array's space-time snapshot may be expressed as

$$\boldsymbol{\chi}_{\mathbf{t}} = \left[\mathbf{x}_{\mathbf{p}} \circ \mathbf{b}_{\mathbf{t}}(\varpi_t)\right] \otimes \mathbf{a}_{\mathbf{s}}(\upsilon_t), \tag{6.6}$$

where $\boldsymbol{a_s}$ is the target's spatial steering vector, $\boldsymbol{b_t}$ is the target's temporal steering vector, the spatial frequency υ_t is $f_c n d \sin(\phi)/c$, ϖ_t is the target Doppler shift normalized by the pulse repetition frequency (PRF), and $\circ$ represents the Hadamard product.

6.1 PARAMETER ESTIMATION-BASED ONLP

The parameter estimation-based ONLP detector derived in Chapter 5 may be extended to multi-channel systems with the addition of spatial frequency as an unknown parameter. From (5.11), the ONLP approximation to the true target phase at each channel is

$$x_{onlp}[m] = \frac{A}{r_b^2} e^{j(C_0 m + C_1 + C_2 \cos(C_3 m + C_4))}, \tag{6.7}$$

where r_b is the center of the range bin at which the target is located; and A, C_0, C_1, C_2, C_3, and C_4 are parameters to be estimated from the measured data. Thus, the ONLP approximation for the MN x 1 space-time snapshot is

$$\hat{\boldsymbol{\chi}}_{\mathbf{onlp}} = \left[\hat{\mathbf{x}}_{\mathbf{onlp}};\quad \hat{\mathbf{x}}_{\mathbf{onlp}} e^{j\hat{C}_5};\quad \cdots\quad \hat{\mathbf{x}}_{\mathbf{onlp}} e^{j(N-1)\hat{C}_5}\right], \tag{6.8}$$

where MLEs of the unknown parameters $\hat{A}, \text{and } \hat{C}_0 - \hat{C}_4$ in (6.7) are substituted into (6.8) above to form the estimate $\hat{\boldsymbol{\chi}}_{\mathbf{ONLP}}$. The spatial frequency $\hat{C}_5$ is the MLE of the unknown incidence angle to the array. Thus, the multi-channel form of the ONLP detector may be written from (5.25) as

$$\mathrm{Re}\left\{\hat{\boldsymbol{\chi}}_{\mathbf{onlp}}^{\mathbf{H}} \hat{\mathbf{R}}_{\mathbf{I}}^{-\mathbf{1}} \boldsymbol{\chi}\right\} > \gamma, \tag{6.9}$$

where $\gamma = \sqrt{\mathrm{Re}\{\hat{\boldsymbol{\chi}}_{\mathbf{onlp}}^{\mathbf{H}} \mathbf{R}_{\mathbf{I}}^{-\mathbf{1}} \hat{\boldsymbol{\chi}}_{\mathbf{onlp}}\}} \cdot Q^{-1}(P_{FA})$, $\boldsymbol{R_I}$ is the covariance matrix of the interference, and P_{FA} is the probability of false alarm.

The results presented in Chapter 5 illustrated the performance of the ONLP detector in complex Gaussian noise with $\mathbf{R}_{\mathbf{I}} = \sigma_n^2 \mathbf{I}$, where σ_n is the noise standard deviation. In most environments, however, the quality of the parameter estimates, hence, the detection performance, is degraded by clutter. The influence of clutter is illustrated in Fig. 6.1, which plots the performance of the ONLP detector in Gaussian noise, in clutter with a clutter-to-noise-ratio (CNR) of 20 dB, and after clutter cancellation using optimal STAP (see Chapter 2, Section 2.2.7).

Notice that even with clutter cancellation, the detector does not achieve the same performance as attained in the presence of only Gaussian noise. This performance loss is a result of the clutter return being similar in form to the sought return. The clutter is, after all, just the sum of reflections from the same transmitted signal. Clutter cancellation offers some improvement in performance, in this case, increasing the signal-to-clutter ratio (SCR) by 8.6 dB. However, the remaining un-cancelled clutter is still enough to make it difficult to obtain reliable parameter estimates.

The ONLP algorithm has a few other drawbacks. First, the algorithm only matches against the torso response, not the entire human response as modeled by Thalmann. Second, the parameters C_0 – C_5 are not physically-based parameters. As

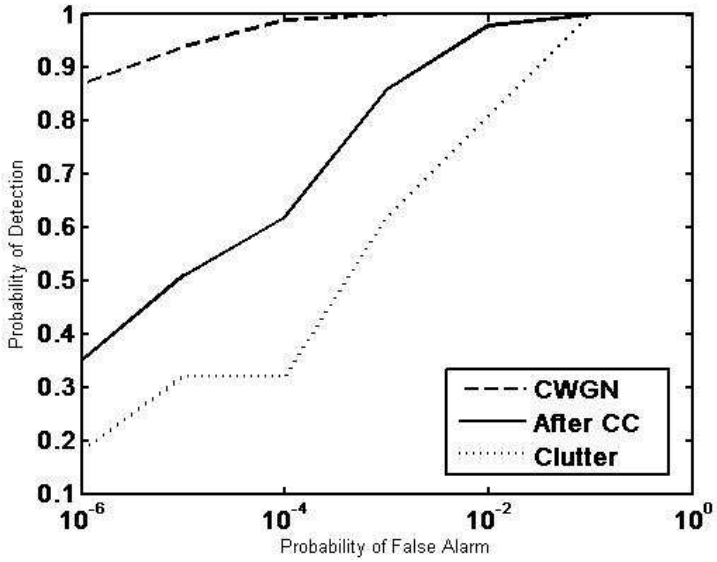

Fig. 6.1. Performance of ONLP detector in complex white Gaussian noise (CWGN), in clutter, and after clutter cancellation (CC).

mathematical constructs of the ONLP approximation, they are not directly relatable to any physical features, such as human size, speed, or direction. Thus, they cannot be used in post-detection processing, such as target characterization or feature extraction. Third, there is no limit on the potential values the parameters C_0, C_2, and C_3 may assume. Since the MLE estimates cannot be computed from closed-form equations, but instead involve searching over values that maximize a non-linear equation, the open-ended nature of the search interval greatly complicates and increases the computational complexity of finding MLE estimates for these parameters.

Since the estimation problem essentially reduces to a search problem, an enchanced ONLP (EnONLP) algorithm that remedies all of the above mentioned drawbacks, while also offering a computationally more practical approach to solving the problem, is proposed next.

6.2 DICTIONARY-BASED ENCHANCED ONLP (EnONLP)

The proposed Enhanced ONLP (EnONLP) method overcomes the difficulty of obtaining good parameter estimates in clutter by implementing a filter bank of the expected target response for each possible value of any unknown parameters. Rather than matched filtering based on just the torso response, as in ONLP, the EnONLP detector compares the data snapshot to a parametric model of the expected target response that incorporates the reflections from all body parts. A basis pursuit algorithm is used to search a dictionary of expected target returns for linear combinations of target responses that best match the measured data. Thus, unlike ONLP, the EnONLP algorithm also has the capability of detecting the presence of multiple human targets.

6.2.1 Formulation

The Enhanced ONLP detector utilizes (5.6) as an approximation for the true human response, where *h* is computed for each body part from the Thalmann model. Thus, the received target signal has the form

$$\hat{\boldsymbol{\chi}}_{\mathbf{EnONLP}} = \left[\hat{x} \circ \mathbf{b}_{\mathbf{t}}(\varpi_t)\right] \otimes \mathbf{a}_{\mathbf{t}}(\upsilon_t), \tag{6.10}$$

where $\hat{x} = \sum_{i=1}^{K} \frac{A}{r_b^2} e^{-j\frac{4\pi f_c}{c}(r - h_i \cos\theta)}$ and $\circ$ represents the Hadamard product.

The EnONLP approximation contains five unknown parameters: target velocity (*v*) and height of thigh (*HT*) from the Thalmann walking model, motion vector angle (θ), incidence angle (ϕ), and target range (*r*). Unlike the parameters $\hat{C}_0 - \hat{C}_5$ in the ONLP model, the EnONLP parameters have specific ranges over which they are defined. The Thalmann model is defined for values of *v/HT* between 0 and 2.3; angles can only be between 0 and 360 degrees; and the target range must lie within the range bin being tested. Thus, the range of possible parameter values is easily discretized into a finite

number of samples for each parameter.

Define $\boldsymbol{\xi} = [\xi_1 \quad \cdots \quad \xi_i \quad \cdots \quad \xi_P]$ as a vector of unknown parameters ξ_i, where P is the total number of unknowns; in this case, P=5 and $\boldsymbol{\xi} = [v \quad HT \quad \phi \quad \theta \quad r]$. The number of possible values each parameter may assume is defined as p_i for the i^{th} parameter. Thus, the total number of potential realizations of $\hat{\boldsymbol{\chi}}_{\mathbf{EnONLP}}$ is given by $Q = \prod_{i=1}^{P} p_i$, where each possible combination of parameter values is denoted by $\boldsymbol{\xi}_\mathbf{j}$, for $j = 1...Q$. For each $\boldsymbol{\xi}_\mathbf{j}$, the corresponding target return model is computed and stored as an entry in a dictionary (D) of size MN x Q

$$\boldsymbol{\mathcal{D}} = \left[\hat{\boldsymbol{\chi}}_{\mathbf{EnONLP}}(\boldsymbol{\xi}_1) \quad \cdots \quad \hat{\boldsymbol{\chi}}_{\mathbf{EnONLP}}(\boldsymbol{\xi}_j) \quad \cdots \quad \hat{\boldsymbol{\chi}}_{\mathbf{EnONLP}}(\boldsymbol{\xi}_Q)\right]. \tag{6.11}$$

The realization that best matches the data is given by the entry corresponding to the peak output when multiplied by $\mathbf{R}_\mathbf{I}^{-1}\boldsymbol{\chi}$. Mathematically,

$$\hat{\boldsymbol{\chi}}_{optimal} \rightarrow \max\left\{\left(\mathbf{R}_\mathbf{I}^{-1}\boldsymbol{\chi}\right)^H \boldsymbol{\mathcal{D}}\right\} \tag{6.12}$$

Effectively, the dictionary functions as a filter bank, in which the peak output is used to form the test statistic required for detection. From [51], the adaptive matched filter (AMF) test makes a positive decision if

$$\frac{\left|\hat{\boldsymbol{\chi}}_{\mathbf{o}optimal}^{\mathbf{H}} \hat{\mathbf{R}}_\mathbf{I}^{-1}\boldsymbol{\chi}\right|^2}{\hat{\boldsymbol{\chi}}_{\mathbf{o}optimal}^{\mathbf{H}} \hat{\mathbf{R}}_\mathbf{I}^{-1}\hat{\boldsymbol{\chi}}_{optimal}} > -\log(P_{FA}) \tag{6.13}$$

6.2.2 Multiple Target Detection

The formulation described above is suitable to test for the presence of at least one human target within a range gate of interest. However, multiple targets can be detected within the EnONLP framework by applying *sparse approximation* techniques, such as basis pursuit [72] or matching pursuit [73, 74]. Sparse approximation refers to the task of representing a signal as the linear combination of a small number of the signals comprising the entire signal set. In other words, a coefficient vector *C* is sought such that

$$\hat{\mathbf{s}} = \sum_{k=1}^{K} C_k \cdot \hat{\boldsymbol{\chi}}_{\mathbf{EnONLP}}\left(\xi_\eta\right), \tag{6.14}$$

where η is an index to the dictionary entries comprising ***s***, and the number of realizations (*K*) comprising the true target signal ***s*** is much less than the total number of dictionary entries, i.e. $K << Q$.

In this work, Orthogonal Matching Pursuit (OMP) [75] is used to recursively compute the best approximation. The procedure may be summarized as follows:

1. Initialize an index set $\boldsymbol{\eta} = \mathbf{0}$, the residual $\mathbf{r_0} = \mathbf{R_I^{-1}}\boldsymbol{\chi}$ and the loop index $t = 1$.
2. Determine an index η_t for which the projection of a dictionary entry onto $\mathbf{r_{t-1}}$ is maximized.
3. Then test for the presence of a target using (6.13).
4. If a target is present, update the index set: $\boldsymbol{\eta_t} \Rightarrow \boldsymbol{\eta_{t-1}} \cup \{\eta_t\}$. Otherwise, stop.
5. Find a coefficient vector ***C*** that solves the least squares problem

$$\min \left\| \mathbf{R_I^{-1}}\boldsymbol{\chi} - \sum_{j=1}^{t} C\left(\eta_j\right)\hat{\boldsymbol{\chi}}_{\mathbf{EnONLP}}\left(\eta_j\right) \right\|_2, \tag{6.15}$$

   where $\|\cdot\|_2$ denotes the Euclidean norm.

6. Update the residual by subtracting out the components already found:

$$\mathbf{r}_t \Rightarrow \mathbf{R}_I^{-1}\chi - \sum_{j=1}^{t} C(\eta_j)\hat{\chi}_{\mathbf{EnONLP}}(\eta_j), \tag{6.16}$$

7. Increment the loop counter: $t \Rightarrow t+1$.

8. Iterate by returning to Step 2.

In addition to the capability of detecting multiple targets, the EnONLP algorithm described above also gives as an output the parameter vector $\boldsymbol{\xi}$ for each detected target, which can potentially be used to further characterize or classify targets.

6.2.3 Refining the Search Space Using Dominant Parameters

Dictionary size is a key issue as it determines both the required memory and computational complexity of operations on the dictionary. The finer the discretization of parameter values, the more accurate the best matching dictionary entry will be, hence, the better the detection performance. Unfortunately, increasing the discretization also increases dictionary size, and, thereby, the memory and computational requirements.

Identifying dominant parameters – in other words, those parameters most critical to maximizing the detector test statistic and ensuring detection – can help reduce dictionary size, while having a minimal impact on detection performance. Once a target is detected, an additional search over these dominant parameters may be performed for the purposes of target classification or characterization. In this work, however, since we are primarily concerned with detection, dominant parameters are used to reduce the computational and memory requirements.

Among the five EnONLP parameters previously mentioned, two may be excluded from the dictionary: range (r) and height of thigh (HT). The range appears in (6.10) as a constant phase shift in the expected target response. We can avoid searching over

phase by slightly modifying the operation in (6.12) and in Step 2 of the OMP algorithm. Rather than compute the projection through multiplication, a convolution operation is performed on each dictionary entry as follows:

$$\mathcal{D}_{\text{conv}}(j) = \hat{\boldsymbol{\chi}}_{\text{EnONLP}}(\xi_j) * \hat{\mathbf{R}}_{\text{I}}^{-1}\boldsymbol{\chi}\,, \tag{6.17}$$

Since the convolution yields essentially phase-shifted copies of the product, the maximum of this new matrix yields not only the optimal parameter vector $\boldsymbol{\xi}$, but also the optimal phase shift (i.e. range). Thus, there is no need to store any phase information in memory.

Furthermore, simulations have shown that for short dwell, variations in the parameter HT cause only slight variations in the projection of the dictionary entry on the signal; in other words, minimal impact on detection performance. Consider human target data generated at varying HT values, but with all other parameters (i.e. velocity, azimuth and direction angles) identical. The target response at each HT is projected against a dictionary whose elements were generated using a fixed HT value corresponding to that of an average male, and all other parameters the same as that of the data. Thus, the only mismatch between the dictionary entries and the data is that due to mismatch in HT. Figure 6.2 shows a plot of the normalized projections versus HT for a signal comprised of 500 pulses.

The peak projection is given when the HT of the human in the data matches the HT utilized in the dictionary. When a mismatch in HT occurs, the projection value slightly drops; however, this drop has an insignificant affect on detection performance. Despite the mismatch, use of an average (typical) HT value in the dictionary still yielded high projection values, hence good detection performance, for all human sizes.

As the dwell time increases, however, the nonlinearities of human motion become more apparent and the effect of HT is more significant. Consider again the

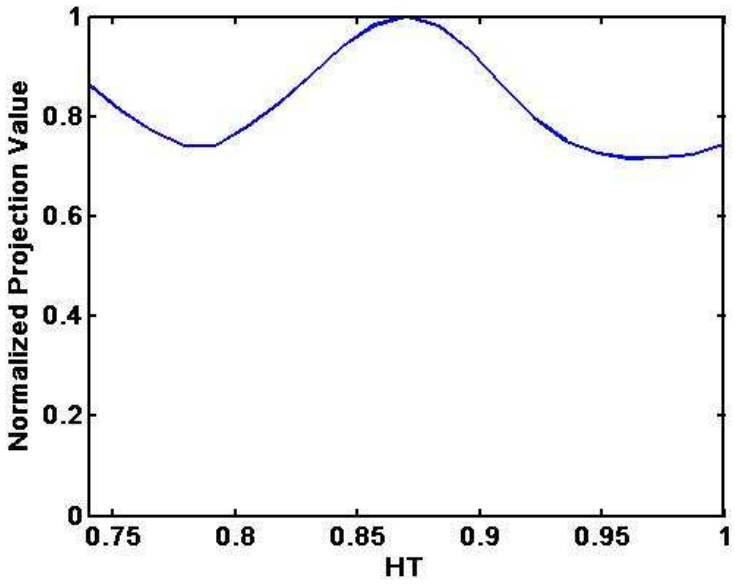

Fig. 6.2: Normalized projection of signal onto dictionary entries for data containing humans of varying HT for a signal with 500 pulses.

change in normalized projection versus HT, but this time for a signal comprised of 2,000 pulses (i.e. a dwell of 1 second), as illustrated in Fig. 6.3. As before, the peak occurs when the HT of the human in the data matches the HT used to create the dictionary; however, the mismatch in HT is now much more pronounced.

Thus, for short dwell HT may be excluded from the dictionary, but for long dwell should be included. Furthermore, for the purposes of target characterization, discussed in more detail in Chapter 7, these results show that a long dwell is required for estimation of the parameter HT. The examples in this section focusing on detection, however, are generally for short dwell, thus, dictionary entries are generated based on the average value of HT for a human male, with each realization generated from all possible combinations of the values of the parameters velocity (v), azimuth (ϕ), and human direction of motion (θ).

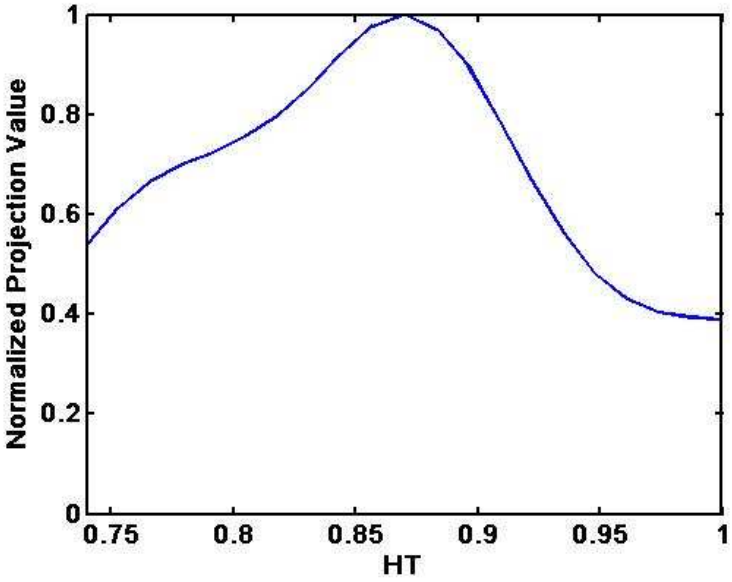

Fig. 6.3: Normalized projection of signal onto dictionary entries for data containing humans of varying HT for a signal with 2,000 pulses.

6.3 DETECTOR PERFORMANCE

Detector performance is evaluated by comparing the receiver operating characteristics (ROC) for the proposed EnONLP detector with that of ONLP and fully adaptive optimum STAP (see Eq. 2.33) in simulated radar data, generated as detailed in Section 6.1. The results presented are generated for a multi-channel radar with characteristics as shown in Table 6.1, chosen as being typical of a representative radar system.

The dictionary used by the EnONLP algorithm is generated by discretizing the unknown parameter ranges as follows: based on the limits in the Thalmann mmodel, velocities between 1.5 m/s and 2.7 m/s are sampled at 0.1 m/s increments; and the angles θ and ϕ are sampled at 5 degree intervals. Mathematically, $v \in \{1.5 \quad 1.6 \quad \cdots \quad 2.6 \quad 2.7\}$ for a total of 13 samples. $\theta \in \{0 \quad 5 \quad \cdots \quad 350 \quad 355\}$ for a total of 72 samples. $\phi \in \{-90 \quad -85 \quad \cdots \quad 85 \quad 90\}$ for a total of 37 samples. The

Table 6.1: Multi-Channel Radar System Parameters

Parameters	Value
Number of Channels	5
Number of Pulses	500
Center Frequency	1 GHz
Sampling Frequency	20 MHz
Bandwidth	10 MHz
Pulse Repetition Interval	0.2 ms
Pulse Width	40 μs
Transmit Power	1.8 kW
Nominal Range	8,760 m

dictionary is comprised of all possible combinations of the parameters v and θ, yielding a total of 13 x 72 = 936 entries. Note that this dictionary stores the possible responses for each velocity and walking direction for one channel only. The model data for all channels for each discritized azimuth angle ϕ can be obtained by simply applying an appropriate phase shift (see Chapter 2, Section 2.2.6) to each dictionary element. Thus for each ϕ a separate multichannel dictionary is created and stored in temporary memory. In this way, the overall dictionary size and hence memory requirements are minimized. Instead of storing a dictionary of size channel number (5) x pulse number (500) by 13*72*37, i.e. 2500 by 34632, a main dictionary of size pulse number (500) by 13*72, i.e. 500 by 936, is stored. Thus, an increase in computational load is traded off for savings in memory.

6.3.1 Receiver Operating Characteristics

ROC curves for the EnONLP, ONLP, and STAP detectors are shown in Fig. 6.4 and Fig. 6.5 for an average-sized male walking at a 45^o angle relative to the x-axis with a speed of 2 m/s. Note that the $\mathbf{R}_\mathbf{I}^{-1}\boldsymbol{\chi}$ factor in the detector test statistic can be decomposed into $\mathbf{R}^{-1/2}\left(\mathbf{R}^{-1/2}\boldsymbol{\chi}\right)$ where the first $\mathbf{R}_\mathbf{I}^{-1/2}$ represents a linear transformation of the EnONLP model and the second $\mathbf{R}_\mathbf{I}^{-1/2}$ is a whitening filter that cancels clutter present in the data vector $\boldsymbol{\chi}$.

Both human model based detectors, ONLP and EnONLP, have better performance in comparison to conventional STAP processing. However, the proposed EnONLP detector exhibits the best performance with a P_D of 0.77 at a P_{FA} at 10^{-6}, steadily increasing as the P_{FA} increases, with the other methods matching performance only when the P_{FA} has risen to 0.01. As the clutter-to-noise ratio (CNR) increases to beyond 15 dB, the other methods exhibit a sharp drop in detection rate, whereas the EnONLP method is able to maintain good performance. Note that for this example, the EnONLP algorithm ran approximately twice as fast the ONLP algorithm, but that in general computational savings is dependent upon the dictionary size (i.e. the fineness of parameter space discretization) in the EnONLP algorithm and the fineness of the parameter search in the ONLP algorithm.

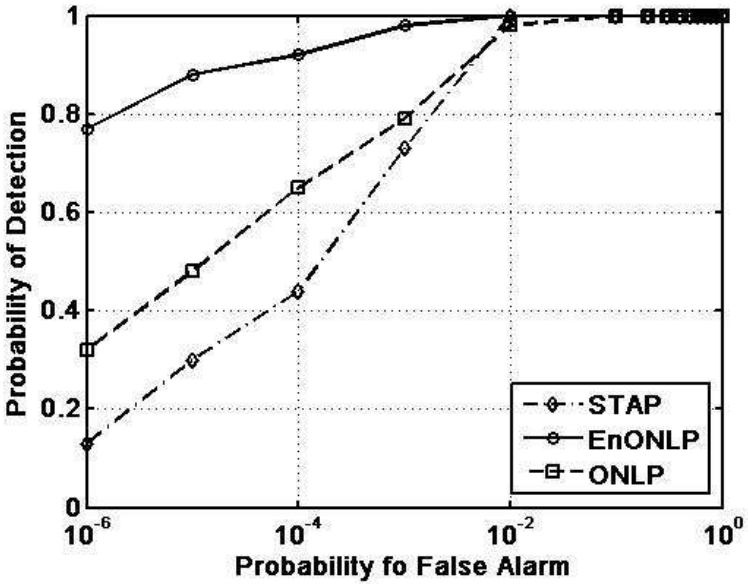

Fig. 6.4. P_D v P_{FA} for a human target with SNR = 0 dB and CNR = 30 dB.

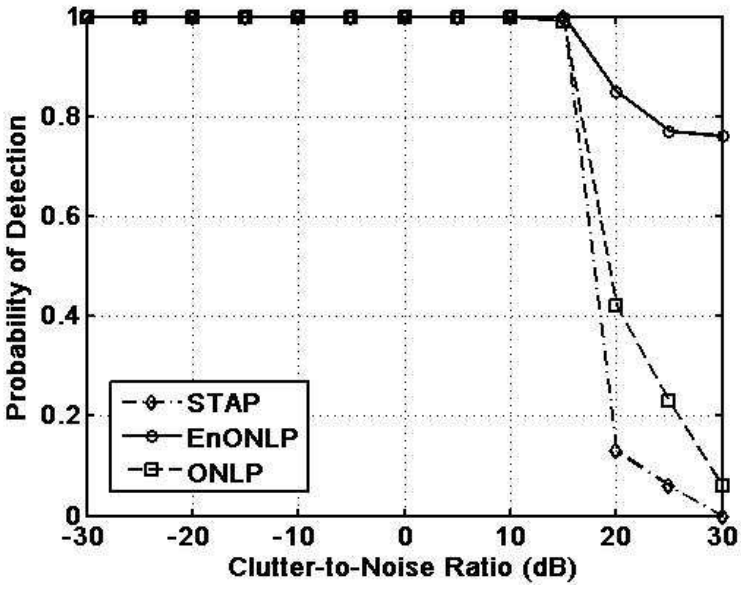

Fig. 6.5. P_D v CNR for a human target with $P_{FA} = 10^{-6}$.

6.3.2 Multi-Target Situation

The EnONLP framework has the additional advantage of being able to detect the number of human targets present in a single range bin, as well as extract an estimate of the modeled parameters for each target. Consider a two target scenario, with one being an average sized male (Target 1) and the other an average sized female (Target 2), in clutter with an SINR of 20 dB. Table 6.2 summarizes the characteristics of the target motion: azimuth angle, direction, and velocity. As described in Section 6.2.2, first the maximum projection of the snapshot onto the dictionary is computed. Fig. 6.6 shows the value of the projection maximized over velocity and walking direction plotted against azimuth angle. Notice that two major peaks are present, but that the largest peak is extracted first, yielding an azimuth angle estimate of 65^o.

In the next iteration, the dictionary entry corresponding to the peak in Fig. 6.6 is removed from the signal, and the remaining signal is projected against the dictionary. Fig. 6.7 shows the result of maximizing over azimuth angle. Note that now only one major peak remains, indicating the azimuth of the second target (-30^o).

Table 6.2: Target Parameters for Two-Human Scenario

	TRUE		DETECTED	
	Target 1	**Target 2**	**Target 1**	**Target 2**
Azimuth	60^o	-30^o	65^o	-30^o
Direction	15^o	30^o	15^o	35^o
Velocity	2 m/s	2.4 m/s	2 m/s	2.3 m/s

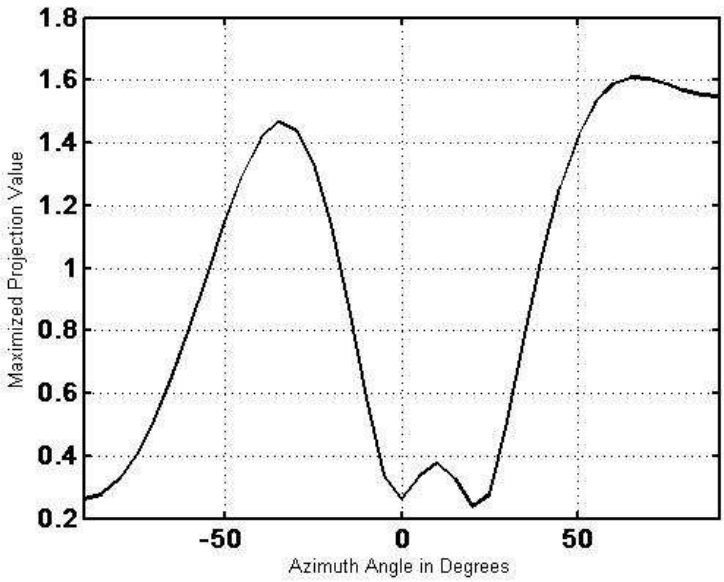

Fig. 6.6. First iteration of OMP showing the maximum projection over velocity and walking direction versus azimuth angle.

If we iterate a third time, the remaining peaks are not strong enough to trigger a detection, indicating that no other targets are present, thus terminating the EnONLP algorithm. Table 6.2 shows the true and detected target parameters. These values are initial estimates, and a finer dictionary should be applied post-detection if more refined estimates are required.

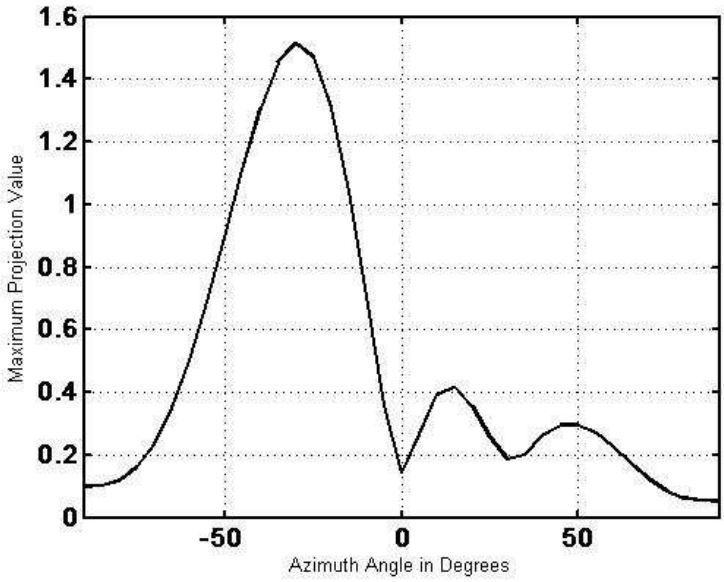

Fig. 6.7. Second iteration of OMP showing the maximum projection over velocity and walking direction versus azimuth angle.

6.3.3 Impact of Resolution and Dictionary Mismatch

The above example showed results for which the two targets were sufficiently separated so that the algorithm could resolve both targets. Additionally, the target parameters coincide with the parameters used to generate the dictionary. However, in general, it is possible for targets to be closely spaced and for there to be mismatch relative to the parameter values in the dictionary.

Consider the two target scenario illustrated in Fig. 6.8. The detection algorithm is applied on two targets located a varying relative angles. The first target is tested at locations sampled along zero degree azimuth, which the second target is tested at locations with azimuth angles varying from -90° to 90°. Notice that when the two targets are greater than 15° apart in azimuth angle, that the algorithm successfully detects both targets, as indicated in Fig. 6.8. However, when the azimuth is less than 15°, the algorithm is unable to discriminate between the targets. Thus, while the algorithm successfully detects that a human target is present, it erroneously decides that there is

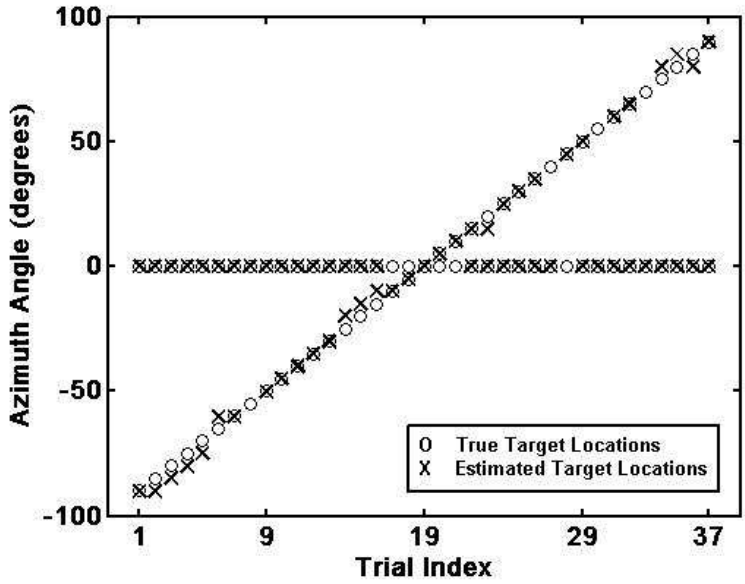

Fig. 6.8. Detection results for a scenario with two targets located at varying relative azimuth angles.

only one target. Azimuth resolution may be improved by increasing the number of channels comprising the radar antenna.

Mismatch between true target parameters and the discretized parameters of the dictionary, on the other hand, is a much more readily addressable issue. Consider the two target situation summarized in Table 6.3. The dictionary is generated for azimuth angles between -90° and 90° with 5° increments, velocities between 1.5 m/s and 2.7 m/s with 0.1 m/s increments, and direction angles of 0° to 355° with 5° increments. Note that none of the parameters of the two targets coincide with any dictionary elements, in fact, they lie approximately in between dictionary entries, representing the maximum possible mismatch.

In this case, despite the mismatch, the EnONLP algorithm is able to successfully detect the presence of both targets. The mismatch causes a slight decrease in the value of the projection, but this is not enough to change the outcome of the detection test. If, however, the parameter space is so crudely sampled so that mismatch results in entirely inaccurate parameter estimates, detection performance may be affected. However, for

Table 6.3: Target Parameters for Two-Human Scenario with Dictionary Mismatch

	TRUE		DETECTED	
	Target 1	**Target 2**	**Target 1**	**Target 2**
Azimuth	42^o	-53^o	40^o	-55^o
Direction	76^o	18^o	70^o	15^o
Velocity	1.87 m/s	2.24 m/s	1.9 m/s	2.05 m/s

most reasonably sampled parameter spaces, the mismatch is simply reflected as an error in the parameter estimates generated – an error easily remedied by applying a more finely discretized dictionary.

In summary, the EnONLP successfully detects the presence of human targets even when there is mismatch between the data and dictionary elements. EnONLP also correctly yields the number of *resolvable* targets present in a single range bin. Resolution is effected by the number of channels, thus, correctly detecting the number of closely spaced humans requires sufficiently increasing the total number of channels.

6.4 CONCLUSIONS

Results show that both human model-based, nonlinear phase detectors, ONLP and EnONLP, exhibit improved detection performance over conventional STAP processing. Because the clutter is comprised of reflections from the transmitted signal, even after clutter cancellation, the parameter estimates obtained via the ONLP algorithm remain degraded in relation to those obtained in complex Gaussian noise. Despite this degradation in estimates, however, ONLP outperforms STAP. EnONLP offers a more robust solution because the search space is confined by finite limits, thereby eliminating the need for an initial estimate or guessed starting point for the search. The dictionary element that yields the greatest matched filter output is directly selected. Thus, even in

high clutter environments, the exploitation of a priori knowledge of human kinematics is useful in designing better human detectors.

The EnONLP framework, however, offers some additional advantages relative to parameter estimation-based ONLP. EnONLP trades off the real-time computational expense of searching for the best MLE with storing possible target returns in memory. Orthogonal matched pursuit (OMP) provides an efficient way of determining the best linear combination of dictionary entries that matches the measured data. Thus, not only can EnONLP be used to simply detect whether or not a human target is present in the range bin, but the number of resolvable human targets can also be computed, along with the associated parameter values. Because the EnONLP parameters are directly related to physical properties of the target, additional knowledge about the target characteristics can be obtained. In Chapter 7, the application of EnONLP to target characterization is discussed.

CHAPTER 7

TARGET CHARACTERIZATION

Target characterization refers to techniques designed to extract additional information about targets beyond whether or not they are present in a given range bin (i.e., detection). Thus, deciding whether or not a detected target is human, or extracting features, such as height or speed, all fall within the scope of target characterization. To date, much of the work in this area has focused on using spectrogram analysis to classify and characterize human targets. The EnONLP framework described in Chapter 6, however, provides an alternative, model-based approach to target characterization. In Section 7.1, recent applications of spectrogram analysis to target characterization and classification are discussed. Then, in Section 7.2 an example of applying EnONLP to discriminate multiple targets of different types is presented.

7.1 SPECTROGRAM ANALYSIS FOR TARGET CHARACTERIZATION

Spectrogram analysis is by far the most ubiquitous method for classifying and extracting features of human targets. A few of the more recent papers are discussed here to illustrate the potential and drawbacks of the spectrogram-based techniques.

For example, Otero [22] examined the harmonics of the spectrogram by taking an FFT over time for each Doppler bin in the spectrogram. From the resulting Doppler Frequency versus Cadence Frequency plot (Fig. 7.1), peaks corresponding to the fundamental gait cadence and higher gait harmonics could be easily picked out. Since the torso moves at roughly a constant velocity, its signal component appears as a peak at zero Hz. The location of the peak along the Doppler axis yields a measurement of the torso velocity, v_0, while the value of the peak gives an estimate of the amplitude of the RCS of the torso.

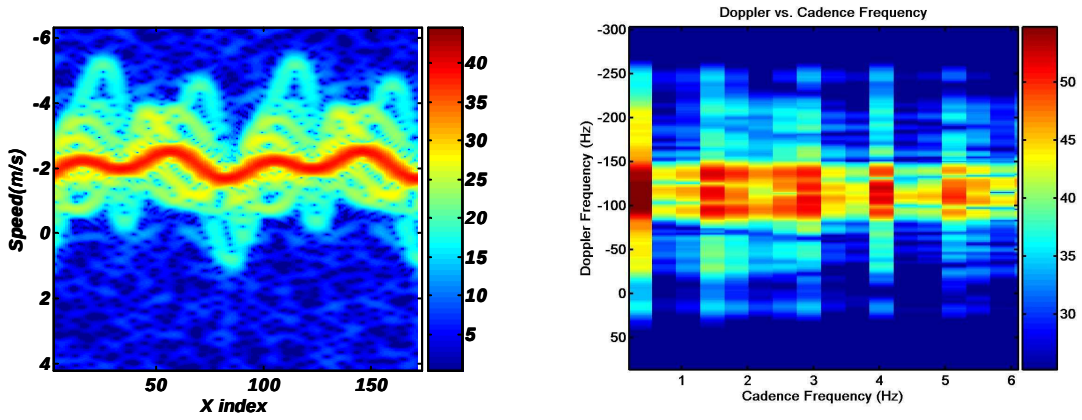

(a) (b)

Fig. 7.1. (a) Sample spectrogram of a human walking. (b) Cadence frequency plot computed from spectrogram in (a).

Otero then defined two features, stride and appendage/torso (A/T) ratio, as

$$Stride = \frac{v_0}{f_m}, \tag{7.1}$$

where f_m is the fundamental cadence frequency, and

$$A/T = \frac{\sum_{n=1}^{3} RCS_n}{RCS_0}, \tag{7.2}$$

where RCS_n is the amplitude of the nth peak; n=0 corresponds to the torso, and n=1, 2, and 3 to the fundamental, 2nd and 3rd harmonics, respectfully. These features were then used to classify whether or not a detected target was human. Additionally, since the legs of animals such as dogs are much shorter than those of humans, Otero suggested exploiting differences in A/T ratio to discriminate humans from animals. Indeed, as shown in Fig. 7.2, the spectrograms of humans and dogs are noticeably different.

Even actions that we would think to be almost insignificant can cause enough of a change in the spectrogram so as to be discernable. For example, Greneker designed a suicide bomber detection system [27] that detected changes in the human spectrogram caused by wearing additional weight around the waist, and Kim [76] applied

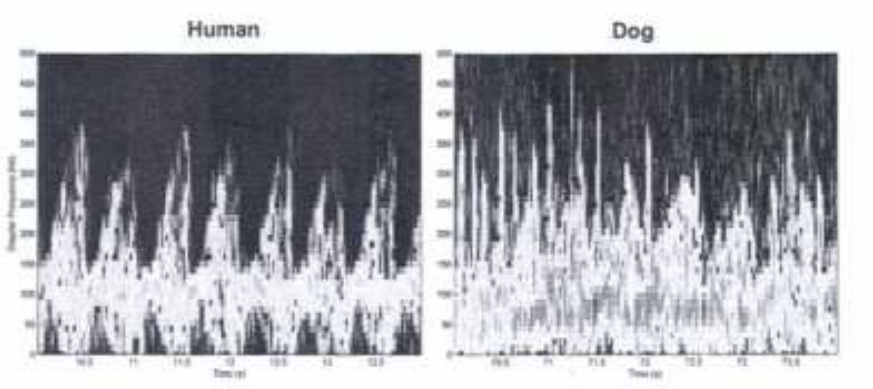

Fig. 7.2. Comparison of the spectrograms for a human and dog [22].

artificial neural networks to classify human activity based on discernable changes in the human spectrogram. That a classification accuracy of over 80% was achieved shows the utility of spectrogram analysis in target characterization.

Nevertheless, there remain two key limitations to spectrogram-based classification: first, accurate extraction of any features from measured spectrograms requires a sufficiently long dwell and high SINR so that estimates are not exceedingly corrupted; second, the spectrograms of multiple targets in the same range bin overlap, making difficult any kind of estimation, as shown in Fig. 7.3. The EnONLP algorithm, however, is still able to obtain reasonable estimates of model parameters in clutter and is able to discriminate multiple targets of varying type, as shown next, in Section 7.2.

7.2 APPLICATION OF EnONLP: MIXED TARGET DISCRIMINATION

The dictionary structure of the EnONLP detector provides a convenient framework for sparse signal approximation that can be exploited for target characterization. As detailed in Chapter 6, the dictionary is simply a database of potential target returns, as generated by varying the parameters in the modeled return. However, if models of other types of targets, or even other types of human activity were to be included in the dictionary, then those would also be tested as part of the orthogonal

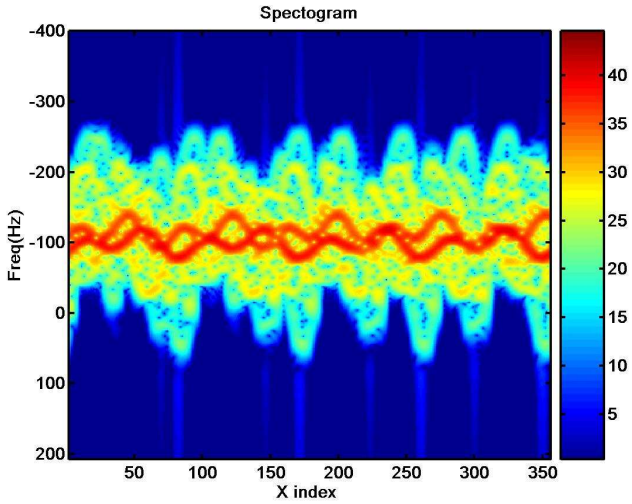

Fig. 7.3. Spectrogram of two human targets located in the same range bin and walking at approximately the same velocity.

matching pursuit algorithm to see whether they formed a component of the best match to the measured data. Thus, addition of a dog model to the dictionary would facilitate discrimination of a target as either human or dog, and addition of running, jumping or crawling models would yield additional information as to what activity the detected human target was engaged in.

As a simpler example, consider a scenario in which a vehicle, a tall male with a thigh height (HT) of 1 meter, and a small female with a thigh height of 0.74 meters are all moving within a single range gate in clutter with an SINR of 20 dB. Table 7.1 provides additional details of the target motion, including azimuth angle, direction, and velocity.

The vehicle is modeled as a point target (linear phase history) with a reflection 10 dB stronger than the male target. Thus, the dictionary is augmented with entries for point target responses, discretized for spatial and temporal steering vector angles between $-\pi$ and $+\pi$. In particular, 30 samples of each angle were taken, resulting in an additional dictionary size of MN x 900 for the point target.

In the first iteration, the algorithm detected the strongest target, i.e. the vehicle, followed by the male in the second iteration and the female in third. Thereafter, no

sufficiently strong targets were detected, and, the algorithm stopped. Thus, all targets were again successfully detected, with the parameters of the best matching dictionary entry listed in Table 7.1.

Table 7.1: Target Parameters for Two-Human and One-Vehicle Scenario

	TRUE		**DETECTED**	
	Male	**Female**	**Male**	**Female**
Azimuth	60^o	-30^o	65^o	-30^o
Direction	15^o	30^o	15^o	35^o
Velocity	2 m/s	2.4 m/s	2 m/s	2.3 m/s
	Vehicle		**Vehicle**	
Azimuth	37^o		37^o	
Rad. Vel.	14 m/s		14 m/s	

Since the first selected dictionary entry is from the augmented dictionary, we conclude that the detected target is a point target, i.e. a vehicle, with the associated radial velocity and azimuth angle of the selected entry. The following two selections are made from within the human dictionary, leading the remaining two targets to be classified as human. Note that aside from the azimuth, direction, and velocity, we still have no other information about the detected human, such as size or gender. Such additional features may be extracted by applying EnONLP again, this time with a dictionary better suited to yield the additional information desired, as illustrated in the next section.

The classification performance of the EnONLP algorithm may be further quantified by considering the confusion matrix shown in Fig. 7.2. Notice that over all SINR levels, the algorithm correctly classifies the vehicle; but as the SINR decreases, the number of trials in which the human is mistakenly classified increases.

Table 7.2: Confusion matrix for classification of human (H) versus vehicle (V).

		PREDICTED									
		SINR=20dB		SINR=0dB		SINR=-5dB		SINR=-10 dB		SINR=-20 dB	
		H	V	H	V	H	V	H	V	H	V
ACTUAL	H	100	0	100	0	43	57	3	97	0	100
	V	0	100	0	100	0	100	0	100	0	100

7.3 REFINING PARAMETER ESTIMATES WITH EnONLP

Once a target has been detected, the dictionary structure of the EnONLP algorithm may be re-applied to improve the initial estimates found during the detection stage, or to extract additional information about detected targets. Consider a scenario in which a radar transmitting 500 pulses illuminates a human with an HT of 0.831 meters, a velocity of 2 m/s, and an azimuth angle of 20° is walking at a 40° angle relative to the x-axis in interference with an SINR of 10 dB. The dictionary is generated for that of an average male with an HT of 0.92 meters. Application of EnONLP yields a detection with approximately correct estimates for the target parameters: azimuth angle, 20°; velocity, 2.2 m/s; and direction angle, 35°.

Now, suppose we wish to apply a different dictionary for the purpose of estimating the detected target's size, i.e. HT. The dictionary is augmented with entries corresponding to values of HT between 0.74 meters (i.e., a woman in the 5^{th} %ile) and 1 meter (i.e., a man in the 95^{th} %ile), discretized into 21 possible values at intervals of 1.25 cm. If memory is a limiting factor, the variation of the other parameters may be restricted to a small interval around the initial estimates found during the detection stage. Furthermore, a longer dwell of 2,000 pulses is used, so that signal changes due to size

becomes more apparent (see discussion in Chapter 6, Section 6.2.1). Applying EnONLP with this modified dictionary yields new estimates of HT = 0.831 meters; velocity, 2 m/s; azimuth angle, 20°; and direction angle, 35°, which are a closer match to the true target data than the initial estimates. Note that in this example HT was found exactly because the correct HT value was included in the generation of dictionary elements, i.e., there was not mismatch between the true value and that of the dictionary entry. Were mismatch to be present, however, the next best value would have been returned as the estimate (see Chapter 6, Section 6.3.3). A summary of the parameter estimates in this example is shown in Table 7.3.

Table 7.3: Target Parameters for Two-Human Scenario with Refined Estimate

	TRUE	INITIAL ESTIMATE	REFINED ESTIMATE
HT	0.831 m	0.92 m	0.831 m
Azimuth	20^o	20^o	20°
Direction	40^o	35^o	35°
Velocity	2 m/s	2.2 m/s	2 m/s

7.4 CONCLUSIONS

Thus, the EnONLP framework developed in Chapter 6 can be used not just for detecting human targets, but for detecting multiple targets of any type, just so long as the appropriate model is included in the dictionary of potential target responses. Furthermore, the EnONLP algorithm yields estimates of the model parameters, which can be used to extract additional information about the detected target. More accurate estimates of model parameters may be obtained by running the data through a secondary dictionary, more finely discretized in an interval around the initial estimates yielded by the EnONLP detector.

CHAPTER 8

CONCLUSION

The primary topic of this thesis has been the application of human modeling towards the design of detectors specifically geared towards improving the detection rates of human targets in clutter for single and multi-channel radar systems. Two optimized nonlinear phase detectors were proposed. The first, denoted simply as the "ONLP" detector, utilized a sinusoidal approximation to the torso response alone and found MLEs of the unknown geometry and kinematic parameters. Results showed that the parameter estimation-based ONLP detector outperformed conventional Fourier-based, linear phase matched filter detectors, both in complex Gaussian noise and in clutter.

The second, an enhanced ONLP, or "EnONLP" detector, employed an orthogonal matched pursuit algorithm to determine the linear combination of possible target responses, stored as dictionary entries, that best matches the data. Effectively, the real time search for the MLEs of the parameters in the ONLP is traded off for the memory required to store all the dictionary elements, followed by implementation of the OMP. Results show that the EnONLP significantly outperforms both the ONLP and conventional STAP in terms of detection performance in clutter. An important advantage is that the EnONLP detector is also capable of detecting multiple targets and discriminating between targets of differing type. Additionally, the parameter values that yield the best matching model also provide information about the detected target that can be useful for target characterization. By adding appropriate target models to the dictionary, target characterization problems such as distinguishing between humans and animals, or differing human motions, such as jumping versus walking, may be resolved. Examples illustrating the performance of the EnONLP algorithm for detecting a man and a woman, and differentiating between two people and a moving vehicle are presented.

8.1 CONTRIBUTIONS

The most critical contribution of this thesis is the development of a novel approach for improving the detection rate of human targets by exploiting knowledge of human modeling and gait analysis. Most of the research in human detection focuses on identifying or classifying already detected targets as humans, while the first problem of detection is only dealt with generically as slow-moving target detection, and the form of the detector itself is the same as that used to detect any other type of target, i.e. linear-phase matched filtering. Our work thus not only presents a novel approach by specifically "tuning" the detector to human targets, but also addresses a fundamental flaw not as of yet addressed: namely, the inherent SNR loss incurred by matched filtering highly nonlinear phase targets such as humans with linear-phase filters.

Two approaches to human model-based detection were successfully implemented for both single and multi-channel radar systems: a parameter estimation-based optimized non-linear phase (ONLP) detector and a dictionary search-based enhanced optimized non-linear phase (EnONLP) detector. Both detectors yielded significant improvement in the probability of detection of human targets over current linear-phase matched filter techniques, even in the presence of high clutter.

Furthermore, the iterative framework of the EnONLP algorithm yielded a mechanism for not just detecting humans but also extracting the number and type of resolvable targets residing within a range bin. For example, humans and vehicles could be distinguished and estimates of their model parameters obtained. Thus, the EnONLP framework is also a key contribution to target characterization and identification.

8.2 FUTURE WORK

There are several areas that can be pursued in future research related aspects of modeling, testing, and analysis. The kinematic model of human motion could be extended to include other kinds of activities, such as running, jumping, or crawling. Or the effect of carrying something in the arms or in a backpack on the human target phase history could be quantified. The addition of such models to the dictionary could then be applied within the EnONLP framework to discriminate between varying human activities. This information in turn could be useful in a number of applications, such as differentiating whether a target was hostile or not.

Another area of future work is conducting experiments on measured radar to further verify and bound performance. Further analytical and experimental work can be done to study the effect on the expected target return of multi-path reflections between humans. Oftentimes, people move not as individuals, but as groups, and due to multi-path the resulting return may not be as simple as just the superposition of individual target returns. Such an analysis could also lead to techniques capable of distinguishing individuals from groups or discerning the number of individuals in a group.

Finally, results from tracking could be incorporated into the ONLP and EnONLP models so that surveillance capabilities are extended over larger distances.

REFERENCES

[1] BOULT, T.E., MICHAELS, R.J., GAO, X., and ECKMANN, M., "Into the woods: visual surveillance of noncooperative and camouflaged targets in complex outdoor settings," *Proceedings of the IEEE*, Vol. 89, Issue 10, pp. 1382-1402, October 2001.

[2] NIU, W., LONG, J., HAN, D., and WANG, Y., "Human activity detection and recognition for video surveillance," *IEEE International Conference on Multimedia and Expo*, Vol. 1, pp. 719-722, June 2004.

[3] YOON, S.M., and KIM, H., "Real-time multiple people detection using skin color, motion and appearance information," *13th IEEE International Workshop on Robot and Human Interactive Communication*, pp. 331-224, September 2004.

[4] CHOI, Y.K., KIM, K.M., JUNG, J.W., CHUN, S.Y., and PARK, K.S., "Acoustic intruder detection system for home security," *IEEE Transactions on Consumer Electronics*, Vol. 51, Issue 1, pp. 130-138, February 2005.

[5] SHOJI, Y., TAKASUKA, T., and YASUKAWA, H., "Personal identification using footstep detection," *Proceedings of 2004 International Symposium on Intelligent Signal Processing and Communication Systems*, pp. 43-47, November 2004.

[6] MAZARAKIS, G.P., and AVARITSIOTIS, J.N., "A prototype sensor node for footstep detection," *Proceedings of the Second European Workshop on Wireless Sensor Networks*, pp. 415-418, 2005.

[7] SUCCI, G., CLAPP, D., GAMPERT, R., and PRADO, G., "Footstep detection and tracking," *Proceedings of SPIE*, Vol. 4393, pp. 22-29, 2001.

[8] RICHMAN, M.S., DEADRICK, D.S., NATION, R.J., and WHITNEY, S.L., "Personnel tracking using seismic sensors," *Proceedings of SPIE*, Vol. 4393, 2001.

[9] BROGGI, A., FASCIOLI, A., CARLETTI, M., GRAF, T., and MEINECKE, M., "A multi-resolution approach for infrared vision-based pedestrian detection," *IEE Intelligent Vehicles Symposium*, pp. 7-12, June 2004.

[10] LINZMEIER, D.T., SKUTEK, M., MEKHAIEL, M., and DIETMAYER, K.C.J., "A pedestrian detection system based on thermopile and radar sensor data fusion," *7th International Conference on Information Fusion*, Vol. 2, pp. 1272-1279, July 2005.

[11] YAROVOY, A.G., LIGTHART, L.P., MATUZAS, J., and LEVITAS, B., “UWB radar for human being detection,” *IEEE Aerospace and Electronic Systems Magazine*, Vol. 21, Issue 3, pp. 10-14, March 2006.

[12] FALCONER, D.G., FICKLIN, R.W., and K.G. KONOLIGE, “Robot-mounted through-wall radar for detecting, locating, and identifying building occupants,” *IEEE International Conference on Robotics and Automation*, Vol. 2, pp. 1868-1875, April 2000.

[13] VAN DORP, P., and GROEN, F.C.A., “Human walking estimation with radar,” *IEE Proceedings on Radar, Sonar and Navigation*, Vol. 150, Issue 5, pp. 356-365, October 2003.

[14] MILCH, S., and BEHRENS, M., “Pedestrian detection with radar and computer vision,” *Proceedings of Conference on Progress in Automobile Lighting*, Darmstadt, Germany, 2001.

[15] SABATINI, A.M., and COLLA, V., “A method for sonar based recognition of walking people,” *Robotics and Autonomous Systems*, Vol. 25, pp. 117-126, 1998.

[16] BOULGOURIS, N.V., HATZINAKOS, D., and PLATANIOTIS, K.N., “Gait recognition: A challenging signal processing technology for biometric identification,” *IEEE Signal Processing Magazine*, November, 2005.

[17] LITTLE, J.J., and BOYD, J.E., “Recognizing people by their gait: The shape of motion,” *Videre: Journal of Computer Vision Research*, Vol. 1, No. 2, The MIT Press, Winter 1998.

[18] WEIR, R.F., and CHILDRESS, D.S., “A new method of characterizing gait using a portable, real-time, ultrasound ranging device,” *Proceedings of the 19th Annual International Conference of the IEEE Engineering in Medicine and Biology Society*, Vol. 4, pp. 1810-1812, October 30 – November 2, 1997.

[19] WEIR, R.F., and CHILDRESS, D.S., “A portable, real-time, clinical gait velocity and analysis system,” *IEEE Trans. on Rehabilitation Engineering*, Vol. 5, No. 4, pp. 310-321, 1997.

[20] GEISHEIMER, J.L., MARSHALL, W.S., and GRENEKER, E., “A continuous-wave (CW) radar for gait analysis,” *Signals, Systems, and Computers*, Vol. 1, pp. 834-838, 2001.

[21] GEISHEIMER, J.L., GRENEKER, E.F., and MARSHALL, W.S., “A high-resolution Doppler model of human gait,” *Proceedings of SPIE, Radar Sensor Technology and Data Visualization*, Vol. 4744, 2002.

[22] OTERO, M., “Application of a continuous wave radar for human gait recognition,” *Proceedings of SPIE, Signal Processing, Sensor Fusion and Target Recognition XIV*, Vol. 5809, pp. 538-548, 2005.

[23] BAKER, C.J. and TRIMMER, B.D., “Short-range surveillance radar systems,” *Electronics and Communication Engineering Journal*, pp. 181-191, Aug. 2000.

[24] CHEN, V.C., “Analysis of radar micro-Doppler signature with time-frequency transform,” *Proc. of the 10th IEEE Workshop on Statistical and Array Processing*, pp. 463-466, 2000.

[25] ZHANG, Z., POULIQUEN, P., WAXMAN, A., and ANDREOU, A., “Acoustic micro-Doppler radar for human gait imaging,” *J. Acoust. Soc. Am. Express Letters*, Vol. 121, No. 3, pp. 110-113, 2007.

[26] BOULIC, R., THALMANN, M.N., and THALMANN, D., “A global human walking model with real-time kinematic personification,” *Visual Computing*, Vol. 6, pp. 344-358, 1990.

[27] GRENEKER, G., “Very low cost stand-off suicide bomber detection system using human gait analysis to screen potential bomb carrying individuals,” *Proceedings of SPIE*, Vol. 5788, 2005.

[28] VAN DORP, P., and GROEN, F.C.A., “Feature-based human motion parameter estimation with radar,” *IET Radar, Sonar and Navigation*, Vol. 2, Issue 2, pp. 135-145, April 2008.

[29] BILIK, I., and TABRIKIAN, J., “Radar target classification using Doppler signatures of human locomotion models,” *IEEE Trans. AES*, Vol. 43, No. 4, pp. 1510-1522, Oct. 2007.

[30] LINNEHAN, R., PERLOVSKY, L., MUTZ, C., RANGASWAMY, M., and SCHINDLER, J., “Detecting multiple slow-moving targets in SAR images.” *IEEE Sensor Array and Multichannel Signal Processing Workshop*, pp. 643-647, 2004.

[31] BERGIN, J. and TECHAU, P., “Multiresolution signal processing techniques for ground moving target detection using airborne radar.” *EURASIP Journal on Applied Signal Processing*, No. 8, pp. 1-16, 2006.

[32] JAO, J.K., YEGULALP, A.F., and AYASLI, S., “Unified synthetic aperture space time adaptive radar (USASTAR) concept.” *MIT Lincoln Lab Report*, 24 May 2004.

[33] FRIEDLANDER, B. and PORAT, B., “VSAR: A High Resolution Radar System for Detection of Moving Targets,” *IEE Proc. on Radar, Sonar, and Navigation*, Vol. 144, No. 4, pp. 205-218, August 1997.

[34] CHEN, P. and BEARD, J.K., “Bistatic GMTI Experiment for Airborne Platforms,” *IEEE International Radar Conference*, pp. 42-46, 2000.

[35] GURBUZ, S.Z., MELVIN, W.L., and WILLIAMS, D.B., “Detection and identification of human targets in radar data,” *Proceedings of SPIE, Defense and Security Symposium*, Orlando, FL, April 9-13, 2007.

[36] GURBUZ, S.Z., MELVIN, W.L., and WILLIAMS, D.B., “Comparison of radar-based human detection techniques,” *41st Asilomar Conference on Signals, Systems, and Computers*, Monterey, CA, November 4-7, 2007.

[37] RICHARDS, M.A., “Fundamentals of Radar Signal Processing,” McGraw Hill, New York, 2005.

[38] SOUMEKH, M., “Synthetic Aperture Signal Processing with MATLAB Algorithms,” John-Wiley and Sons, 1999.

[39] CARRARA, W.G., GOODMAN, R.S., and MAJEWSKI, R.M., “Spotlight Synthetic Aperture Radar: Signal Processing Algorithms,” Artech House, 1995.

[40] BRENNAN, L.E., and REED, I.S., “Theory of Adaptive Radar,” IEEE Transactions on Aerospace and Electronic Systems, AES-9, 2, pp. 237-252, March 1973.

[41] REED, I.S., MALLET, J.D., and BRENNAN, L.E., “Rapid Convergence Rate in Adaptive Arrays,” IEEE Transactions on Aerospace and Electronic Systems, AES-10, 6, pp. 853-863, Nov. 1974.

[42] BRENNAN, L.E., MALLETT, J.D., and REED, I.S., “Adaptive Arrays in Airborne MTI,” IEEE Transactions, AP-24, (5), pp. 607-615, 1976.

[43] KLEMM, R., “Introduction to Space-Time Adaptive Processing,” Electronics and Communication Engineering Journal, pp. 5-12, Feb. 1999.

[44] ENDER, J.H.G., “Space-Time Processing for Multichannel Synthetic Aperture Radar,” Electronics and Communication Engineering Journal, pp. 29-38, Feb. 1999.

[45] MELVIN, W.L., “A STAP Overview,” IEEE A&E Systems Magazine, Vol. 19, No. 1, pp. 19-35, Jan. 2004.

[46] KLEMM, R. “Principles of Space-Time Adaptive Processing,” The Institute of Engineering and Technology, 2006.

[47] KAY, S.M., “Fundamentals of Statistical Signal Processing: Volume II, Detection Theory,” Prentice-Hall, 1998.

[48] JOHNSON, D.H., and DUDGEON, D.E., “Array Signal Processing: Concepts and Techniques,” Prentice-Hall, 1993.

[49] HELSTROM, C.W., “Elements of Signal Detection and Estimation,” Prentice-Hall, 1995.

[50] MORRIS, G. and HARKNESS, L., “Airborne Pulsed Doppler Radar,” Artech House, 1996.

[51] ROBEY, F.C., FUHRMANN, D.R., KELLY, E.J., and NITZBERG, R., “A CFAR adaptive matched filter detector,” *IEEE Transactions on Aerospace and Electronic Systems*, Vol. 28, No. 1, January 1992.

[52] KAY, S.M., “Fundamentals of Statistical Signal Processing: Volume I, Estimation Theory,” Prentice-Hall, 1993.

[53] NOVACHECK, T.F., “The biomechanics of running,” *Gait and Posture*, Vol. 7, pp. 77-95, 1998.

[54] BEHNCKE, H., “A mathematical model for competitive running,” *Methods of Operation Research*, Issue 49, pp. 471-498, 1985.

[55] WATANABE, K., “Kinematical Analysis and Measurement of Sports Form,” *IEEE Transactions on Systems, Man, and Cybernetics – Part A: Systems and Humans*, Vol. 36, No. 3, May 2006.

[56] SMITH, B., ASHTON, K.M., BOHL, D., CLARK, R.C., METHENY, J.B., and KLASSEN, S., “Influence of carrying a backpack on pelvic tilt, rotation and obliquity in female college students,” *Gait and Posture*, Vol. 23, pp. 263-267, 2006.

[57] FOWLER, N.E., RODACKI, A.L.F., and RODACKI, C.D., “Changes in stature and spine kinematics during a loaded walking task,” *Gait and Posture*, Vol. 23, pp. 133-141, 2006.

[58] FIOLOKOWSKI, P., HORODYSKI, M., BISHOP, M., WILLIAMS, M., and STYLIANOU, L., “Changes in gait kinematics and posture with the use of a front pack,” *Ergonomics*, Vol. 49, No. 9, pp. 885-894, 15 July 2006.

[59] ORENDURFF, M.S., SEGAL, A.D., BERGE, J.S., FLICK, K.C., SPANIER, D., and KLUTE, G.K., “The kinematics and kinetics of turning: limb asymmetrics associated with walking in a circular path,” Gait and Posture, Vol. 23, pp. 106-111, 2006.

[60] McGEER, T., “Passive walking with knees,” *Proceedings of IEEE Robotics and Automation Conference*, Cincinnati, OH, pp. 1640-1645, 1990.

[61] GARCIA, M., RUINA, A., COLEMAN, M., “Some results in passive-dynamic walking,” *Euromech Conference on Biology and Technology of Walking*, Munich, Germany, March 1998.

[62] YAM, C-Y., NIXON, M.S., and CARTER, J.N., “Automated person recognition by walking and running via model-based approaches,” *Pattern Recognition*, Vol. 37, pp. 1057-1072, 2004.

[63] ORMONEIT, D., BLACK, M.J., HASTIE, T., and KJELLSTROM, H., “Representing cyclic human motion using functional analysis,” *Image and Vision Computing*, Vol. 23, pp. 1264-1276, 2005.

[64] WHITE, M.O., “Radar cross-section: measurement, prediction and control,” *Electronics and Communication Engineering Journal*, pp.169-180, August 1998.

[65] YAMADA, N., TANAKA, Y., and NISHIKAWA, K., “Radar cross section for a pedestrian in 76 GHz band,” *2005 European Microwave Conference*, Vol. 2, 4-6 October 2005.

[66] DOGARU, T., NGUYEN, L., and LE, C., “Computer Models of the Human Body Signature for Sensing Through the Wall Radar Applications,” *U.S. Army Research Laboratory Technical Report ARL-TR-4290,* September 2007.

[67] RoyMech Website:
http://www.roymech.cok.uk/Useful_Tables/Human/Human_sizes.html

[68] SHNIDMAN, D.A., "Generalized Radar Clutter Model," IEEE Transactions on Aerospace and Electronic Systems, Vol. 35, No. 3, pp. 857-865, July 1999.

[69] SHNIDMAN, D.A., "Radar Detection in Clutter," IEEE Transactions on Aerospace and Electronic Systems, Vol. 41, No. 3, pp. 1056-1067, July 2005.

[70] MICHELS, J.H., HIMED, B., and RANGASWAMY, M., "Performance of STAP Tests in Gaussian and Compound-Gaussian Clutter," Digital Signal Processing, (10), pp. 309-324, 2000.

[71] WARD, J., "Space-Time Adaptive Processing for Airborne Radar," Technical Report, ESC-TR-94-109, Lincoln Laboratory, Dec. 1994.

[72] CHEN, S.S., DONOHO, D.L., and SAUNDERS, M.A., "Atomic Decomposition by Basis Pursuit," SIAM Journal on Scientific Computing, Vol. 20, No. 1, pp. 33-61, 1998.

[73] TROPP, J.A., "Topics in Sparse Approximation," PhD Dissertation, Computational and Applied Mathematics, The University of Texas at Austin, August 2004.

[74] MALLAT, S., and ZHANG, Z., "Matching Pursuit in a Time-Frequency Dictionary," IEEE. Transactions on Signal Processing, Vol. 41, pp. 3397-3415, 1993.

[75] PATI, Y.C., REZAIIFAR, R., and KRISHNAPRASAD, P.S., "Orthogonal Matching Pursuit: Recursive Function Approximation with Applications to Wavelet Decomposition," Proc. of the 27th Asilomar Conference on Signals, Systems and Computing, 1993.

[76] KIM, Y., and LING, H., "Human Activity Classification Based on Micro-Doppler Signatures Using an Artificial Neural Network," Antennas and Propagation Society International Symposium, AP-S 2008, pp.1-4, 5-11 July 2008.

VITA

SEVGİ ZÜBEYDE GÜRBÜZ

SEVGİ Z. GÜRBÜZ was born in Redwood City, California on November 8, 1976. She graduated from the Massachusetts Institute of Technology (MIT) in June 1998 after completing her B.S. degree in Electrical Engineering with Minor in Mechanical Engineering. As an undergraduate, she spent three summers working at NASA Ames Research Center in Moffett Field, CA, involved with the acoustic properties of wind tunnels and the stress analysis of helicopter blades. She also held two undergraduate research assistantships, one investigating the fire damage of composite materials, and one designing the electronics controlling the vibrating motors of a tactile navigation vest to aid the blind. As a recipient of a USAF Reserve Officers Training Corps Scholarship, upon graduation she was also appointed as a 2nd Lieutenant in the United States Air Force and was one of three AFROTC graduates selected nationwide to pursue her master's degree while on active-duty.

Under the Charles Stark Draper Laboratory Fellowship, she conducted research on the architecture of Delta-Sigma A/D converters, leading to her graduating again from MIT with her M.Eng. degree in Electrical Engineering and Computer Science in February 2000. Thereafter, she was assigned as a radar signal processing engineer to the Signal Processing Technology Branch, Sensors Directorate, Air Force Research Laboratory, Rome, NY, pursuing research in radar signal processing and radar waveform design. From January to June 2003, she was deployed as a Turkish linguist to Diyarbakir, Turkey.

Upon separating from active duty military service as a Captain in January 2004, she was awarded a National Defense Science and Engineering Graduate (NDSEG) Fellowship to pursue her doctoral research full-time at the Georgia Institute of Technology, Atlanta, GA. Since then, she has been a graduate research assistant at the Georgia Tech Research Institute (GTRI) Sensors and Electromagnetic Applications Laboratory (SEAL). Her research interests include radar signal processing, synthetic aperture radar, detection and estimation.

While not working on her research, she enjoys playing piano, reading Turkish history, and spending time with her 3 year old son Mustafa Alperen and husband Ali Cafer Gürbüz.